NASA TM-79171

NASA Technical Memorandum 79171

NASA-TM-79171 19790015749

AN EXPERIMENTAL INVESTIGATION OF FORCE MIXING OF A TURBULENT BOUNDARY LAYER IN AN ANNULAR DIFFUSER

Robert Joseph Shaw
Lewis Research Center
Cleveland, Ohio

April 1979

AN EXPERIMENTAL INVESTIGATION OF FORCED MIXING OF A TURBULENT BOUNDARY LAYER IN AN ANNULAR DIFFUSER

by

ROBERT JOSEPH SHAW

Submitted in partial fulfillment of the requirements
for the Degree of Doctor of Philosophy

Thesis Advisor: John D. Lee

Department of Aeronautical and Astronautical Engineering
OHIO STATE UNIVERSITY

June 8, 1979

AN EXPERIMENTAL INVESTIGATION OF FORCED MIXING OF A TURBULENT BOUNDARY LAYER IN AN ANNULAR DIFFUSER

DISSERTATION

Presented in Partial Fulfillment of the Requirements for the Degree of Doctor of Philosophy in the Graduate School of The Ohio State University

By

Robert Joseph Shaw, B.A.A.E., M.S.

* * * * *

The Ohio State University

1979

Reading Committee:

Dr. John D. Lee

Dr. Gerald M. Gregorek

Dr. Stuart L. Petrie

Approved By

_____

Adviser
Department of
Aeronautical & Astronautical
Engineering

ACKNOWLEDGEMENTS

The author wishes to mention a few of the individuals without whose assistance this effort could not have been completed. The author will be forever grateful to the NASA-Lewis Research Center Training Committee and particularly Ms. Gertrude Collins who provided this educational opportunity. The author is also indebted to his adviser Dr. John D. Lee who provided guidance and assistance when needed but who also allowed the author the freedom to independently pursue the solution to the problem posed. This effort could not have been completed with any degree of success without the most professional assistance of Ms. Eileen Cox and Susan Button who wrote the data reduction computer programs and Robert Freedman and Larry Jones who helped in the facility buildup and data acquisition phases. Finally, the author wishes to thank his wife, Loretta, and daughter, Cynthia, for the many sacrifices they have made to allow him to complete this effort.

VITA

[redacted] . . . . . Born - [redacted]

1970 . . . . . Bachelor of Aeronautical and Astronautical Engineering, The Ohio State University, Columbus, Ohio

1970 . . . . . M.S., Aeronautical and Astronautical Engineering, The Ohio State University, Columbus, Ohio

1970 - 1979 . . . . . Aerospace Engineer, NASA-Lewis Research Center, Cleveland, Ohio

PUBLICATIONS

1970

1. Shaw, R. J., "A Schlieren Study of Airflow over a Film Cooled Turbine Blade," M.Sc. Thesis, The Ohio State University, Columbus, Ohio.

1973

2. Wasserbauer, J. F.; Shaw, R. J.; and Neumann, H. E.: Minimizing Boundary Layer Bleed for a Mixed Compression Inlet. AIAA Paper 73-1270, November, 1973.

1974

3. Shaw, R. J.; Mitchell, G. A.; and Sanders, B. W.: Distributed Porous Throat Stability Bypass to Increase the Stable Airflow Range of a Mach 2.5 Inlet with 60-Percent Internal Contraction. NASA TM X-2974, 1974.

4. Shaw, Robert J.; Mitchell, Glenn A.; and Sanders, Bobby W.: Forward Slanted Slot Throat Stability Bypass to Increase the Stable Airflow Range of a Mach 2.5 Inlet with 60-Percent Internal Contraction. NASA TM X-2973.

5. Shaw, Robert J.; Mitchell, Glenn A.; and Sanders, Bobby W.: Distributed Educated Throat Stability Bypass to Increase the Stable Airflow Range of a Mach 2.5 Inlet with 60-Percent Internal Contraction. NASA TM X-2975, 1974.

6. Mitchell, Glenn A.; Sanders, Bobby W.; and Shaw, Robert J.: Throat Stability Bypass Systems to Increase the Stable Airflow Range of a Mach 2.5 Inlet with 60-Percent Internal Contraction. NASA TM X-2976, 1974.

7. Wasserbauer, Joseph F.; Neumann, Harvey E.; and Shaw, Robert J.: Distortion in a Full-Scale Bicone Inlet with Internal Focused Compression and 45 Percent Internal Contraction. NASA TM X-3133, December 1974.

1975

8. Wasserbauer, Joseph F.; Shaw, Robert J.; and Neumann, Harvey E.: Design of a Very-Low-Bleed Mach 2.5 Mixed-Compression Inlet with 45 Percent Internal Contraction. NASA TM X-3135, 1975.

9. Neumann, Harvey E.; Wasserbauer, Joseph F.; and Shaw, Robert J.: Performance of Vortex Generators in a Mach 2.5 Low Bleed Full-Scale 45 Percent Internal Contraction Axisymmetric Inlet. NASA TM X-3195, 1975.

1976

10. Shaw, Robert J.; Wasserbauer, Joseph F.; and Neumann, Harvey E.: Boundary Layer Bleed System Study for a Full Scale, Mixed Compression Inlet with 45 Percent Internal Contraction. NASA TM X-3358, 1976.

1977

11. Koncsek, J. L.; and Shaw, R. J.: Operating Characteristics of an Inlet Model Tested with a 0.5 M Powered Fan at High Angles of Attack. NASA CR-135270, 1977.

1978

12. Shaw, Robert J.; Williams, Robert C.; and Koncsek, Joseph L.: VSTOL Tilt Nacelle Aerodynamics and Its Relation to Fan Blade Stresses. NASA TM-78899, 1978.

13. Shaw, Robert J.; Williams, Robert C.; and Koncsek, Joseph L.: Tilt Nacelle Aerodynamics and its Relation to Fan Blade Stresses. AIAA Paper 78-958, July 1978.

FIELDS OF STUDY

Major Field: Aeronautical and Astronautical Engineering

Studies in Aerodynamics: Professors J. D. Lee and G. M. Gregorek

Studies in Viscous Flow and Heat Transfer: Professor O. R. Burggraf

Studies in Mathematics: Professor Henry Colson

TABLE OF CONTENTS

LIST OF FIGURES

LIST OF SYMBOLS

A	diffuser cross-sectional area
AR	aspect ratio of vortex generator
AR'	aspect ratio of vortex generator assuming semi-span is $h - \delta^*$
a	direction sensitivity coefficient of hot film probe
$C_1, C_2, \tilde{C}_2$	calibration coefficients for hot film probe
C_f	skin friction coefficient
C_L	lift coefficient of vortex generator if it were immersed in a uniform stream
C_ℓ	section lift coefficient
C_p	static pressure coefficient
D	lateral period or spacing of vortex generators
d	spacing between adjacent vortex generators which form a divergent pair
E	total voltage output of hot film anemometry probe
$\overline{E}$	steady-state voltage output of hot film anemometry probe
e	fluctuating voltage output of hot film anemometry probe
f	hot film response function
H	boundary layer profile shape factor
h	semi-span of vortex generator
h'	height of vortex axis above confining surface
k_0, k_1, k_2, k_3	constants in hot film response relation
L	diffuser axial length

ℓ	vortex generator chord or mixing length in boundary layer
M	Mach number
N	boundary layer profile power law exponent
n	exponent in governing equation for hot film anemometry probe
P_t	total pressure
p	static pressure
Q	dynamic pressure
Q_{eff}	effective cooling velocity for a hot film probe
Q_{normal}	velocity component normal to sensor of a hot film probe
$Q_{parallel}$	velocity component parallel to sensor of a hot film probe
R	radius
Re	inlet Reynolds number based on annulus height
r	radial co-ordinate
t	time
U	steady state axial velocity component
U_*	friction velocity
u'	fluctuating axial velocity component
V	steady-state transverse velocity component
V_θ	circumferential velocity induced by vortex
v'	fluctuating transverse velocity component
W	steady-state circumferential velocity component
w'	fluctuating circumferential velocity component
x	surface axial coordinate
y	coordinate normal to surface
z	diffuser axial coordinate
α	angle-of-attack of vortex generator

β	yaw angle of velocity vector out of axisymmetric plane
Γ	vortex strength or circulation
γ	ratio of specific heats
ΔR	total pressure rake dimension
δ	boundary layer thickness
δ^*	boundary layer displacement thickness
ϵ	eddy viscosity coefficient
ζ	axial component of vorticity
θ	boundary layer momentum thickness
ν	lmainar kinematic viscosity coefficient
ρ	fluid density
τ	turbulent shear stress
ϕ	diffuser angular coordinate
ψ	angle between inclined hot film sensor and axial velocity component

Subscripts:

B	diffuser station B
C	diffuser station C
D	diffuser station D
center	center of vortex
core	vortex core
e	edge of boundary layer
exit	diffuser exit station
hub	diffuser hub surface
inlet	diffuser inlet station
inlet,2d	two-dimensional value at diffuser inlet station
jet	jet value

max	maximum value
min	minimum value
no VG	no vortex generators installed
ref	reference value
tip	diffuser tip surface
VG-sep'n	vortex generator-to-separation position
VG	vortex generator position
W	wall value
0	inlet station
1d,inc	one dimensional, incompressible value
∞	free stream value

Superscript:

$\bar{}$	average value (time or space)

CHAPTER I

INTRODUCTION

The problem of boundary-layer separation and prevention is one of the oldest problems to confront the fluid mechanicist. According to Chang,[1] Prandtl was concerned about the separation problem even before he started his work on boundary-layer theory. His particular problem was connected with trying to resolve the discrepancy between the theoretical performance of subsonic diffusers with the experimentally measured performance levels.

Through the years, a number of concepts have been advanced to hopefully inhibit boundary-layer separation and the resultant decreases in performance of the fluid mechanical device in question whether it is a wing, control surface, diffuser or combustor. Included among these so called boundary-layer control concepts are bleeding and blowing which rely on either removing the low energy fluid or supplementing it with high energy fluid. Bleeding and blowing have been used extensively to cure aerodynamic separation problems but the hardware required for such systems is viewed as a drawback both from the standpoint of weight and complexity. A somewhat different form of boundary-layer control which is the subject of this study is that of forced mixing.

The term forced mixing implies that some device is used to supplement the normal mixing occurring in the boundary layer and thus to interject relatively higher energy air into the region of the boundary layer immediately adjacent to the confining wall. It is this energizing of the inner strata of a boundary-layer which allows the boundary layer to overcome the adverse pressure gradient imposed on it.

The forced mixing device establishes some secondary flow patterns within the flowfield which transport the relatively high energy fluid from the free stream into the boundary layer. This fluid mixes with the boundary layer flow with the result that the boundary layer is energized. That is, the velocity profile is fuller than it would have been without any mixing having occurred. At the same time, low energy air from the boundary layer is expelled into the free stream and mixed with the potential flow field.

The concept of forced mixing devices is not new. According to available literature, Bruynes[2] of United Aircraft patented one such device in 1951 although Taylor,[3-7] also of United Aircraft, authored several reports dealing with the same basic design in the 1946-50 time period.

The Taylor-Bruynes device was simply a series of small wing like protuberances which were mounted from the confining wall at an angle of attack with respect to the oncoming flow. These protuberances had a lift associated with them which resulted in a trailing vortex being shed from essentially the wing tip of each of the devices. This large scale vortical motion established the desired mixing of the high energy free stream flow with the low energy boundary-layer flow. These devices were aptly named vortex generators, and they will constitute the particular fluid mixing device which is the object of this study.

Countless other forced mixing devices have been tested. A number of such designs are discussed in the paper by Schubauer and Spangenburg.[8] The devices differ only in the way in which the secondary flow patterns are established to effect the desired fluid mixing. A more recent investigation of a different forced mixing device which has been advanced as a candidate for actual flight applications is the so called flow control rail which has been investigated by Sajben et al.[9]

An obviously attractive feature of a forced mixing device is the lack of mechanical complexity. Such systems require no associated hardware such as do boundary-layer bleeding and blowing systems. The extra weight required translates into either a reduced aircraft payload or range. However, forced mixing devices do have an associated drag penalty which should be accounted for in any final evaluation.

The open literature has numerous examples of vortex generators applied to various fluid mechanical devices and the resultant increases (or in some cases decreases!) in performance. An overview of much of the work done with various forced mixing devices for different applications is given by Woolard.[10] Summaries of not only experimental but theoretical studies are presented. Also included is a rather comprehensive reference list of past work efforts. Pearcy[11] presents a similar overview of past efforts by British investigators who appear to have expended a significant effort in studying forced mixing.

The particular application to be treated herein is the subsonic diffuser. Subsonic diffusers are integral parts of aircraft propulsion systems. To minimize aircraft weight, diffusers must be as short as possible, but diffuser performance must be high (that is high total pressure recovery and low total pressure distortion) if acceptable levels of power plant efficiency are to be attained. These two requirements are conflicting as short diffusers imply large adverse static pressure gradients being present if the desired diffusion is to be achieved. The large adverse gradients will probably result in boundary-layer separation occurring which will tend to reduce the performance to unacceptable levels. Longer diffusers reduce the magnitude of the adverse gradient but increase the resulting component weight to unacceptable levels.

Thus, to keep diffusers as short as possible, it often becomes necessary to incorporate boundary layer control to maintain attached

flow. Vortex generators have been frequently used in diffuser designs since such a system is simple to fabricate and has no movable parts (and hence very little associated weight penalty).

The pioneering work done by Taylor and Bruynes mentioned previously involved fundamental studies in the United Aircraft Corporation Laminar Flow Tunnel, a two dimensional non-return low turbulence wind tunnel. The effectiveness of various vortex generator configurations in inhibiting separation was investigated for a series of different adverse pressure gradients. Taylor also did some potential flow analysis to predict vortex generatic performance.

A number of experimental studies of vortex generators installed in subsonic diffusers can be mentioned. Taylor's aforementioned studies did involve placing vortex generators in the subsonic diffuser of the United Aircraft Wind Tunnel for the purpose of reducing the power consumption of that facility.

Valentine and Carroll[12-13] studied the increase in performance of a conical diffuser with vortex generators installed. They concluded that increases in static pressure recovery of as much as 40 percent could be achieved if the proper vortex generator configuration was chosen. They also indicated that the dynamic activity at the diffuser exit plane was greatly reduced when vortex generators were installed which would be expected if boundary-layer separation were suppressed.

Wood and his colleagues[14-16] at NACA Langley investigated a number of annular diffuser designs with vortex generator flow control. Their studies involved inlet flows both with and without swirl components as their particular application was potential turbojet afterburner designs.

Nishi and Senoo[17] studied the use of vortex generators to increase the divergence angle of a conical diffuser without incurring separation. They determined a divergence angle of 16 degrees could be achieved.

Several studies have been reported which dealt with attempting to improve the subsonic diffuser of an inlet system for an aircraft application. MacMiller[18] studied a large number of subsonic diffuser designs which were typical of designs to be used in actual aircraft applications. A portion of this study involved using vortex generators to improve diffuser performance.

Mitchell and Davis[19] investigated vortex generator performance in the subsonic diffuser of an axisymmetric inlet system designed for operation at a free stream Mach number of 3.0.

Neumann, Wasserbauer, and Shaw[20] reported on the improvement in performance of an axisymmetric mixed compression inlet for Mach 2.5 operation with vortex generators installed.

Woolard's work[10] which has already been mentioned, also involved an experimental study of a subsonic diffuser for a two-dimensional supersonic inlet for a supersonic transport application.

An example of an actual flight aircraft inlet using vortex generators to improve performance was that presented by Ting, et al.[21] Their effort involved the design and testing of a new center inlet and S duct for the Boeing 727 subsonic transport with refanned JT8D engines.

Brown, Nawrocki, and Paley[22] reported on the efforts to design a short two-dimensional diffuser suitable for use with the Lockheed version of the supersonic transport. Their approach incorporated vortex generators as an integral part of the diffuser design.

Several works have been published which attempted to predict the theoretical performance of configurations with vortex generators. These efforts have been principally concerned with predicting the inviscid potential flow fields which would simulate actual vortex generator flow fields.

In addition to his considerable experimental efforts, Taylor attempted to predict the cross-sectional streamlines of a series of vortices in a circular pipe and qualitatively compare his results with experimental results. He made a number of assumptions which allowed the problem to be reduced to a two-dimensional one.

Jones[23] undertook a similar analysis of an infinite series of vortices placed adjacent to a flat plate. He made many of the same assumptions as did Taylor to enable him to treat the problem as being locally two dimensional. Jones' predictions of vortex trajectories agreed reasonably well with available experimental data.

Pearcy[11] examined much of the British theoretical efforts in predicting the paths of the vortices and drew some conclusions regarding acceptable design criteria for vortex generator systems.

Nishi and Senoo[17] used a two-dimensional complex potential analysis to predict the paths of vortices in a pipe and compared their results with measurements. They also attempted to verify their conclusions as to acceptable vortex generator designs with some limited performance measurements of four conical diffuser designs.

Some general comments can be made concerning the work done to date, both theoretical and experimental, in regards to vortex generator forced mixing. The experimental efforts by and large have been of the system development type. That is a given design of diffuser is tested both with and without vortex generators and the relative performance levels (e.g., diffuser static and total pressure recoveries and diffuser exit distortion levels) are compared. A trial and error procedure of trying different vortex generator configurations is attempted to hopefully arrive at an "optimum" configuration.

Criteria for selection of vortex generator design is usually that developed by Taylor in his original studies mentioned previously. Very little attempt has been made at making detailed flow field measurements and surveys so as to understand the fluid physics of vortex generator forced mixing. A few experimental investigations can be pointed out which undertook the task of trying to understand the fluid mechanics involved. Schubauer and Spangenburg[8] investigated a number of forced mixing devices in conjunction with the flow over a flat plate with an imposed pressure gradient. They made detailed total pressure surveys at a number of positions relative to the mixing devices for each of several axial stations. Their aim was to study how the devices affected the development of the boundary layer, especially the momentum and displacement thicknesses and incompressible shape factor.

Spangler and Wells[24] measured boundary layer profiles and wall shear stress levels for the flow in a pipe downstream of a row of vortex generators. Their aim was to determine if forced mixing affected the wall shear stress levels.

Ponte and Baron[25] investigated the turbulent structure of a vortex with the long range goal of constructing a model of the vortex-boundary layer interaction phenomenon. They also attempted to outline areas for future research which would be needed if a model of the vortex mixing phenomenon were to be constructed.

The previously mentioned work of Sajben et al.[9] could be termed a fundamental study of forced mixing even though the devices employed were not classical vortex generators.

Thus, it appears that a definite need exists for a fundamental data base to better understand the fluid mechanics of forced mixing. In particular, it would be appropriate to make the required measurements in an actual diffuser flow field so as to accurately duplicate the system of interest.

Also, it appears that to date no comprehensive modeling of forced mixing has yet been attempted. The theoretical treatments previously discussed have dealt with simplified geometries and have attempted to predict vortex paths using only potential flow considerations. No attempts have been made to incorporate the viscous aspects of the problem which are of great significance.

Models which incorporate the key physical elements are needed to input into available computer codes to enable calculations to be made to predict the performance of diffusers which employ forced mixing.

Thus, with these thoughts in mind, the general goals of the research program discussed herein are twofold: (1) make detailed measurements of the appropriate quantities needed to gain an understanding of the physical aspects of forced mixing, and (2) incorporate the physical insight gained into an analytical model of the forced mixing phenomenon.

The next section will discuss the fluid physics of forced mixing.

CHAPTER II

PHYSICAL CONSIDERATIONS OF VORTEX GENERATOR FORCED MIXING

As Schubauer and Spangenburg[8] pointed out, the underlying concept of forced mixing is to introduce a large scale stirring or mixing of the flow over and above that level of mixing accomplished by the random fluctuations present in a turbulent boundary layer. The level of mixing in a turbulent boundary layer is measured by the turbulent shear stress levels since the shear stress indicates the amount of axial momentum being transported across planes parallel to the confining wall. It is this diffusion of axial momentum from the faster fluid regions to the slower fluid regions near the wall which energizes the boundary-layer and allows it to proceed against an adverse pressure gradient without separating.

The concept of eddy viscosity has been introduced to relate the turbulent shear stress to the mean velocity gradient and hence is an indication of the amount of mixing present. Schubauer and Spangenburg point out that the level of eddy viscosity is on the order of 100 times greater than the corresponding laminar viscosity for typical boundary-layer flows while it is on the order of 1000 times greater for wakes and jets. Thus for forced mixing to be beneficial, the levels of mixing (and hence, shear stress and eddy viscosity) must be increased over the levels normally found in turbulent boundary layers.

As already indicated, the forced mixing accomplished by vortex generators is a result of the large scale rotary induced motion which is established by the trailing vortices. Consider Figure 1 which shows a low aspect ratio wing mounted perpendicular to the confining surface and set at an angle of attack with respect to the oncoming boundary layer flow. The lift generated by the wing results in trailing vorticity being shed, and this trailing vorticity ideally wraps up into a single trailing vortex as shown. The induced vortical motion results in the fluid particles having helical paths about the vortex filament. Fluid particles in the free stream which have a high axial momentum are swept into the boundary layer on one side of the vortex. Natural turbulent mixing within the boundary-layer then mixes these high momentum particles with the lower momentum boundary-layer particles with the result that the mean axial momentum of the fluid particles within the boundary layer is increased.

Simultaneously low momentum particles within the boundary layer are swept out into the free stream and mixed with the higher momentum free stream flow.

However, it must be realized that a number of these wing-like protuberances are placed (usually) at the same axial station in close proximity to one another to effect a complete spanwise energizing of the retarded boundary layer.

Figure 2 presents the two general vortex generator configurations which are usually employed in conjunction with many fluid mechanical devices. The so-called co-rotating configuration (Fig. 2(a)) features all the generators with the same orientation with respect to the mean direction of the flow field. It can be seen that for this configuration all vortices have the same rotation (and hence, the description of co-rotating). The counter rotating configuration (Fig. 2(b)) has the generators alternately set at positive and negative angles of attack. The alternate angle of attack setting results in the vortices having alternate senses of rotation which lead to the term counter rotating being used to describe such a configuration.

The co-rotating configuration has some desirable features which has let to its use on aircraft wings to increase the stall free angle of attack range. However, diffuser applications have almost completely employed the counter rotating configuration, and since the diffuser is the particular fluid mechanical device to be considered herein, only the counter-rotating configuration will be discussed.

It is convenient at this point to introduce the nomenclature which will be used to describe counter-rotating vortex generator designs. Figure 3 shows a typical design. For counter-rotating vortex generator configurations, since the individual blades alternate in orientation ($+\alpha$, $-\alpha$) they form what is termed divergent and convergent pairs. Since this pattern repeats itself over the entire span of the installation, the symbol D is used to indicate the lateral period of the generators. That is the vortex generator pattern is repeated every D units of length. The spacing between adjacent blades which make up a diverging pair is represent by the symbol d. The geometry of each blade is given by ℓ (chord) and h (semi-span) while the angle of attack is denoted by α. It should be noted that the vortex generators depicted in Figure 3 have a rectangular unswept planform. A later discussion will indicate that some improvements in performance could be expected for blades with swept leading edge, variable chord distribution, etc., but only simple rectangular planform vortex generator designs were used in the experimental program described herein.

Also, as Figure 3 shows, the height of the axis of the trailing vortex filament above the confining surface is denoted by h'.

It can be anticipated that the amount of forced mixing achieved for any given application will be very dependent on the strength and the positions of the trailing vortices. For

counter-rotating vortex generator designs, the induced velocities which are established in the flow field cause the positions of the vortices to change significantly as they are convected downstream. In turn, the strengths of the vortices are very dependent on the positions of the vortices since if and when the vortices interact with each other or with the boundary layer, significant decreases in the strength of the vortices will occur. The forced mixing is then clearly governed by the strength and paths of the vortices, and a knowledge of these factors is essential in order to understand the fluid mechanics of vortex generator forced mixing.

The prediction of the strength of the trailing vortices shed from vortex generators is a difficult task. The incoming flow field to the generators is of a very complicated nature since it is the local boundary-layer profile and this along with the fact that the aspect ratios of typical vortex generators are usually small results in approximate treatments of the problem being employed. A common assumption is that of ignoring the boundary-layer effects and treating the vortices as being semi-infinite in extent. That is in any plane (extending downstream from the tips of the generators) perpendicular to the axial direction, the flow can be regarded as being two-dimensional flow of a perfect fluid. Jones[23] used a complex potential method to determine the strength of an infinite series of counter rotating vortices positioned above a flat plate while Nishi and Senoo[17] performed a similar analysis for vortex generators placed in a constant diameter pipe. In each case, the downwash across the generator blade was taken as a constant and calculated from the induced velocity equations derived from the governing complex potential relations. Nishi and Senoo achieved what they termed satisfactory agreement when they compared their theoretical predictions of vortex strength with measurements made in a pipe using a vortmeter.

Gould[26] argued that the similarity between vortex generators and wings allowed wing theory to be employed to calculate the strength of the shed vortices. He pointed out that the confining surface could be taken to be aerodynamically equivalent to a plane of symmetry in the absence of the boundary layer. He also indicated that past experiments (unreferenced) have shown that if the blade height-to-local-boundary layer height is greater than four, the effect of the boundary-layer could be accounted for by taking the effective plane of symmetry at the height of the boundary layer displacement thickness. It should be pointed out that in many diffuser applications, the height-to-boundary layer thickness ratio is on the order of two or less so some caution should be exercised in using Gould's suggested approach.

According to Gould, modified wing-theory predicts the following form for the strength of the trailing vortex

$$\Gamma = B \frac{C_L}{AR} U_\infty h \left[\left(1 - \frac{\delta^*}{h}\right) \frac{1 + \frac{AR}{2}}{1 + \frac{AR'}{2}} \right] \tag{1}$$

where

$B = C_{\ell}\ell / C_L\overline{\ell}$ and $C_{\ell}\ell$ is evaluated at the effective plane of symmetry, i.e., $h - \delta^*$

C_L lift coefficient of vortex generator if immersed in uniform stream

AR aspect ratio of actual vortex generator

AR' aspect ratio of vortex generator with semi-span of $h - \delta^*$

δ^* displacement thickness of boundary layer at vortex generator station

The height of the axis of the vortex filament above the confining surface is given by

$$h' = \frac{h}{B} + \delta^* \left(1 - \frac{1}{B}\right) \tag{2}$$

An implicit assumption was made in Gould's analysis that all the trailing vorticity wraps up to form a single tip vortex. Obviously such an assumption is only partially correct. Dosanjh, Gasparek, and Eskinazi[27] measured the amount of circulation which rolled up into a trailing vortex behind an NACA 0009 airfoil, rectangular planform wing cantilevered from a wind tunnel wall and found it to be only 0.58 of the expected value. Nishi and Senoo[17] incorporated this fact in their analysis.

Taylor[3-7] also considered this fact in his pioneering work concerning vortex generators and indicated that to achieve constant circulation across the span of the generator and hence, shed only a tip vortex, the variation of chord should be such that the product of the local wing chord and velocity should remain constant. Since the generator is mounted in a velocity gradient region (the boundary layer) this requirement necessitates a variable chord generator. In practice the scale size of vortex generators is so small that such a requirement cannot realistically be met, and most applications employ generators of rectangular planform. Taylor did point out that such a compromise would not significantly affect the strength of the shed tip vortex.

In connection with the height of the vortex axis from the confining surface (h'), Taylor indicated that experimental results showed that $h' = 0.9\ h$.

Mutual interaction effects between the vortices of a counter rotating configuration also play a very important role in determining the paths of the vortices and hence the forced mixing effectiveness. Consider the array of equally spaced counter-rotating vortices of Figure 4 located over a plane surface and the accompanying image vortices. The resultant velocity induced at each vortex by its image which is horizontal results in the vortices being grouped in pairs as shown. Once the vortices pair off, the effect of the image vortices is lessened and the resultant induced velocities carry each vortex away from the surface as shown. The movement of the vortices away from the surface obviously decreases the levels of forced mixing achievable, and thus, it is important to be able to describe the paths of the vortices and especially to understand the importance of the various parameters which describe a counter-rotating vortex generator configuration in determining the resultant paths.

Figure 5 taken from reference 11 represents pitot pressure contours taken at various axial distances downstream of an equally spaced vortex generator configuration. The contours clearly show the vortices moving together into pairs and then away from the surface. These contours also show the mixing action of the vortices. The boundary layer thickness in the diverging passage is reduced to less than half of the appropriate thickness when no vortex generators were present. The boundary layer in the convergent passage also can be seen to have grown thicker than the nominal value due to the low energy boundary layer fluid being swept outward. Notice also how viscosity acted to spread out and diffuse the vortices in the downstream direction.

Consideration can also be given to more general vortex generator configurations, that is those configurations which have unequal vortex generator spacing. Figure 6, also taken from reference 11, shows the lateral paths of the vortices and image vortices for a configuration with $D/d > 2$. It should be noticed that $D/d > 2$ implies that the diverging pair of vortex generators are spaced more closely than the converging pairs. The vortices can be seen to initially move near the surface (1-2) as they pair off and then transport each other away from the surface (2-3). The vortices should provide an effective mixing action during stages 1 and 2 and, in fact, the mixing action could be increased over that of the equally spaced configuration (Fig. 4) since the vortices move closer to the surface prior to moving away.

The path prediction studies done to date have only treated idealized flow cases. Jones[23] considered the case of an infinite number of initially equally spaced counter-rotating vortices positioned over a flat plate. The flow was taken to be incompressible,

the boundary layer was ignored, and the vortices were taken to be infinite in extent which allowed a complex potential treatment of the real and image vortices to be made. An implicit assumption was made that the slopes of the vortex axis could be neglected; that is at any axial station, the flow could be assumed to be two-dimensional. With these assumptions it was possible to derive equations which predict the paths of the vortices as functions of the appropriate geometric variables.

Gould[26] used Jones method to predict the paths of several different vortex configurations and the results are shown in Figure 7. The effect of the spacing ratio D/d on the vortex paths can be clearly seen. The equally spaced configuration (D/d = 2) can be seen to lift off the surface immediately while the unequally spaced configurations (D/d = 2.5, 3, and 4) initially move closer to the surface prior to lifting off. It should be noted that the higher the value of D/d the closer to the surface the vortices approach but in turn the faster they move away from the surface. It is also apparent from the figure that as the spacing ratio is increased the spanwise movement of the vortices is increased.

This figure points out an important consideration in connection with counter-rotating vortex generator configurations, namely, they have a limited axial range over which they can act as efficient forced mixers. Once the vortices start moving away from the confining surface their ability to carry high momentum fluid particles into the boundary layer becomes severely diminished. Thus, it is very important that the surface distance over which the boundary layer must be energized must coincide with the distance over which the vortices remain in close proximity to the confining surface.

It should be pointed out that the Jones analysis did not include any three-dimensional effects, i.e., the contributions of the bound vorticity for each generator blade were neglected. This bound vorticity would be expected to induce a lateral velocity component on each vortex which would reduce the movement toward the surface (1-2 of Fig. 6). (The movement toward the surface by each vortex is primarily due to the vertical velocity component induced by the near neighbor vortex and the bound vorticity induced velocity would tend to carry these vortices away from one another.) Also the vortex movement toward the wall occurs in the first 1-2 blade heights downstream. This coincides with the region where the shed vorticity is in the process of rolling up to form the trailing vortex so the assumption of a single vortex in this region is not correct.

Pearcy[11] used Jones' technique to calculate vortex paths for various values of not only D/d but also D/h. (Note that Gould only considered the case D/h = 2). The axial paths are shown in Figure 8. An important point to be noted is the effect of doubling the value of D/h while holding D/d constant (configurations B and C). The movement toward the surface is decreased but the axial

distance over which the vortices remain close to the surface is greatly increased over the distances for configurations A and B.

Figure 9 depicts vortex generator configurations which would be expected to produce the vortices the paths of which are depicted in Figure 8. It should be noted that three configurations are shown which would give the nondimensional vortex paths labeled as C. It can be seen that the spacing D, height h, and chord ℓ vary between the configurations C1-C3 but the governing nondimensional parameters D/d and D/h remain constant. Thus, other considerations must be used to determine which of the three C configurations would be the most attractive mixing configuration.

Thus it can be seen that Jones' analysis even though it considers a specialized case does point out the importance of the nondimensional spacing parameters D/d and D/h in the resultant vortex paths and hence, the mixing effectiveness.

However, it also must be stressed that these treatments are purely inviscid and as such the viscous effects are completely ignored.

Gould[26] attempted to determine optimum vortex generator configurations using a momentum interchange parameter as an indicator of vortex mixing effectiveness. He related the average flux of axial momentum toward the confining surface through surfaces parallel to the confining surface and used the classical relationships for induced velocity components for an infinite array of equally spaced vortices over a flat plate. His analysis indicated that the effectiveness per unit span of vortex generation increased to a maximum for d/h in the interval 1.0 to 1.5. The exact value of d/h for the maximum effectiveness as well as the level of effectiveness was dependent on the value of h/δ. Gould used similar analysis for a single vortex generator and its image vortex to show that the maximum effectiveness occurred for $h/\delta = 1.2$. A rapid decrease in effectiveness was noted as h/δ was decreased from the optimum value.

It must be pointed out that Gould's analysis neglected the effects of momentum loss in the boundary-layer due to the profile drag of the generator blades. As the spacing between blades is decreased, more blades would be required per unit span and the resultant increase in drag would offset somewhat the predicted increased in effectiveness.

The above discussed treatments of vortex generator forced mixing are very illustrative in pointing out the important geometrical parameters which govern the vortex paths and resulting mixing effectiveness. However, the analysis failed to account for one very important factor (that of viscosity), the effects of which cannot be neglected. When a vortex comes into contact with the boundary layer, the shear stresses present act to reduce the strength of the vortex and the reduced strength is reflected in a decreased mixing effectiveness.

An appreciation for the effects of viscosity on a vortex can be gained by considering Squire's solution[28] for a two-dimensional vortex immersed in a turbulent fluid. His analysis yielded the following expressions for the mean axial vorticity and circumferential velocity variations through the vortex, assuming an eddy viscosity relationship:

$$\zeta = \frac{\Gamma_o}{4\pi(\nu + \varepsilon)t} \exp\left[-\frac{r^2}{4(\nu + \varepsilon)t}\right] \tag{3}$$

$$V_\theta = \frac{\Gamma_o}{2\pi r}\left\{1 - \exp\left[-\frac{r^2}{4(\nu + \varepsilon)t}\right]\right\} \tag{4}$$

Figure 10 shows the variation of the nondimensional circumferential velocity through the vortex for different values of the parameter $4(\nu + \varepsilon)t$. As time increases the viscosity acts to significantly decrease the levels of axial velocity and to increase the size of the vortex. The decreased circumferential velocity is an indication of a reduced forced mixing ability.

An appreciation of the growth of the vortex in a turbulent fluid can also be gotten from a simple analysis originated by Squire.[28] Squire assumed the vortex generator blade was elliptically loaded which allowed a determination of Γ_o to be made. He further assumed that the core radius of the vortex was the radius where ζ was equal to 0.05 of its value at $r = 0$. The assumption of uniform flow allowed time to be related to downstream distance through $U_\infty = xt$. The resultant expression for the core radius variation was

$$\Gamma_{core}^2 = \frac{12(\nu + \varepsilon)x}{U_\infty} \tag{5}$$

Squire at this point assumed that the eddy viscosity could be related to the vortex strength through

$$\varepsilon = 0.001\ \Gamma_o \tag{6}$$

where the constant 0.001 was arrived at from some unpublished test results. The assumption of elliptic blade loading resulted in the following expression for the nondimensional core size where the molecular viscosity effect was ignored.

$$\left(\frac{\Gamma_{core}}{h'}\right)^2 = \frac{0.048}{\pi} \cdot \frac{C_L}{AR} \cdot \frac{x}{h'} \tag{7}$$

Figure 11 is a plot of the above expression. The vortex radius can be seen to increase rather rapidly in the initial stages. It is conceivable that for the cases where the height of the vortex axis h' is only slightly larger than the boundary layer thickness δ, the vortex will interact with the boundary layer very soon after its formation, and hence, the dissipative effects of viscosity will begin. Thus, depending on the severity of the separation problem and, hence, the amount of forced mixing required to retain attached flow, the effects of viscosity must be minimized. This can be done either by increasing the vortex height relative to the boundary layer thickness or by increasing the shed vorticity strength so that the trailing vortex will retain sufficient strength in spite of the viscous effects. Either of these solutions will involve a penalty since the drag of the vortex generators will be increased.

Nishi and Senoo[17] measured the effects of viscosity on the strength of vortices shed from generators mounted on the wall of a constant diameter circular pipe using a vortmeter. They determined that the vortex strength distribution was of the following form

$$\frac{\Gamma}{\Gamma_o} = 1 - \exp\left(-\frac{0.02\ U_\infty}{x}\right) \tag{8}$$

They used the above expression along with a Jones types of potential flow analysis to predict the paths of the vortices, and they indicated the results were satisfactory when compared with the experimentally determined paths.

The above considerations lead to the following concept for the vortex generator-turbulent boundary layer interaction problem. Figure 12 shows a vortex generator blade of height, h which is larger than the local boundary-layer height. The trailing vortex axis height h' is shown to be somewhat less than h but still greater than δ. The shed vorticity wraps up into the trailing vortex and is convected downstream. If it is assumed that the fluid surrounding the vortex is inviscid, the circulation or strength will remain constant and the vortex will not grow in size. However, once the vortex encounters the turbulent boundary layer, viscosity will act to not only reduce the strength of the vortex but also to increase its size. The stronger the interaction with the turbulent boundary layer is, the faster the rate of dissipation of the vortex and resultant growth would be. This viscous dissipation acts to reduce the mixing action and the resultant effectiveness of the vortex generator in preventing separation would be limited.

This model emphasizes the fact that proper sizing of the vortex generator blades is a critical factor in determining the resultant performance. If the separation point for a diffuser moves axially as operating conditions change, it may be necessary that the vortices persist in strength for a relatively long distance downstream. This

would require that the height of the blade be increased relative to the boundary layer height so that the effects of viscous dissipation would be minimized. If, however, the separation point does not move then perhaps the generator semi-span can be reduced relative to the boundary layer height. The model also implicitly points out the importance of placement of the generator blades relative to one another since the potential flow path prediction showed that the mutual interaction effects could result in the vortices coming closer to the confining surface which would result in the vortices interacting with the boundary layer and with viscous dissipation occurring.

The interaction model also indicates some features which probably should be incorporated in any models of the vortex generator mixing process. If it is assumed (as Squire[28] did) that the eddy viscosity which accounts for the mixing action can be related to the vortex strength or circulation, then in the noninteractive portion of the vortex downstream path, the eddy viscosity would be a constant since the vortex strength is constant. However, once the vortex interacts with the turbulent boundary layer, the vortex strength is dissipated so the resultant mixing action and eddy viscosity level should be decreased. However, it also appears that to include such information in a mixing model might prove difficult since the vortices affect the boundary layer thickness as a result of the mixing (Fig. 5).

Ponte and Barron[25] studied the flow field downstream of the vortex generators mounted on a flat plate. They employed a voltmeter to measure the angular velocity variation through the vortices and compared the experimental profiles with the predicted variation through a vortex immersed in a laminar fluid. They argued that the agreement between the theory and the experimental data indicated that since the solution for a vortex immersed in a laminar fluid was for a constant viscosity fluid, the eddy viscosity through the vortices shed from the vortex generators could also be taken to be a constant. They did point out that the eddy viscosity must be zero in the nonturbulent core of the vortex but that since the rate of strain tends to zero as the vortex axis is approached, the assumption of a constant eddy viscosity is not seriously in error.

The authors also compared the axial distribution of maximum angular velocity with that predicted from the laminar vortex solution. They indicated that for both cases the maximum angular velocity varied inversely with the axial distance, and that again the agreement in form indicated that the eddy viscosity did not vary with axial position. However, they did indicate that such an assumption could be in error by as much as 15 percent.

The assumption of a constant eddy viscosity would result in the eddy viscosity level being only a function of the trailing vortex

strength according to the authors; although they do point out that they could not prove this relationship using the available data and that further experiments would be required.

Another characteristic of the trailing vortices which should be mentioned is that of the vortex bursting phenomenon. The inner portions of a vortex have reduced energy levels since part of the initial vortex energy is converted into heat through viscous dissipation, and since the pressure increases in the downstream direction ($\partial p/\partial x > 0$), the tendency is for air to be pushed upstream around the vortex axis. If the shear stress levels within the vortex are not sufficiently large, reversed flow may occur within the vortex and this occurrence can result in bursting of the vortex. Obviously, once vortex bursting has occurred, the forced mixing process no longer occurs.

It is also conceivable that the pressure differential existing between the vortex core and any separated flow regions could result in reverse flow in the vortex and subsequent bursting. Conceptually, vortex bursting is a very difficult phenomenon to directly detect since interaction effects due to the measurement probes could cause the vortices to burst.

Thus far consideration has been given only to the details of the flow downstream of the vortex generators. However, the flow in the near vicinity of the generators can also have a distinct influence on the strength of the shed vorticity. If the vortex generator blade is considered as a wing set at some angle of attack, then the boundary layer flow over the suction side of the blade will be accelerated while the flow over the pressure side of the blade is decelerated. The deceleration of the flow over the pressure side results in a thickening of the boundary layer in the vicinity of the blade and can even result in a localized flow separation. These deleterious effects can in turn result in a decrease in the strength of the shed vorticity and resultant mixing effectiveness. The localized thickening and possible separation also increases the momentum losses in the boundary layer.

If vortex generators are immersed in locally supersonic flow, bow shock waves will be formed forward of the generators and again the boundary layer can appreciably thicken or even possibly separate.

Thus far only the attributes of vortex generator forced mixing have been discussed. However, there is a price to be paid for vortex generators being used with a fluid mechanical device and that is the drag of the devices. The drag of the generator blades should be accounted for in any final analysis of overall effectiveness. This is especially true in a wing installation since vortex generators are normally used to increase the angle-of-attack capability of the wing. For normal cruise conditions, the vortex generators are not required and the increase in drag can be significant depending on the design.

For diffuser applications, the situation is somewhat different in that the design goal is to make the device as short as possible while retaining acceptable performance levels. In addition, diffuser designs of interest would usually experience flow separation for all operating conditions of interest without vortex generators being present. Thus, the drag of the vortex generators which is manifested as a total pressure loss at the exit station is a necessary penalty to be absorbed to prevent a more significant performance penalty from being paid. For both applications, minimum drag configurations should be chosen which would provide sufficient mixing to prevent separation.

The drag of a vortex generator blade is composed of two components: the profile drag which is a function of airfoil shape and blade size and the induced drag which is mainly a function of the strength of the shed vortex. In order to assess the drag penalty of vortex generator configurations, it is necessary to simultaneously consider effectiveness in producing forced mixing and associated drag penalty. Gould[26] attempted such an analysis for equally spaced counter-rotating configurations by considering the ratio of the induced drag (for assumed elliptic loading) to the effectiveness parameter already discussed. He attempted to minimize this quotient and found that (1) blade geometry and incidence should be chosen so that each generator is operating at its maximum lift-to-drag coefficient level; (2) blade aspect ratio should be high, and (3) blade height should be kept as small as possible. Gould pointed out his analysis did not include profile drag effects which would alter the conclusions somewhat.

Theoretically generator blade aspect ratio and blade sections could be chosen to yield high lift-to-drag coefficient levels without conflicting with maximum effectiveness criteria; however, the size of vortex generators for typical applications often makes simple rectangular, constant airfoil section designs the only practical designs.

To date analytical treatments of the vortex generator mixing process do not exist. The idealized treatments of the process already discussed do add important qualitative understanding, but the design and implementation of a vortex generator configuration to improve the performance of a candidate diffuser still remains an experimental trial-and-error procedure.

Few references exist which set down any design criteria; rather most simply report the performance of a given diffuser with various generator configurations.

Surprisingly, Taylor's pioneering work[3-7] still provides the design criteria which are followed. It will be recalled that Taylor studied many vortex generator configurations in the diffuser of the

United Aircraft Research Laboratory's eight-foot-subsonic-wind tunnel. He based his results on the study of velocity profiles measured at various positions downstream of the generators. His studies involved the systemmatic variation of many of the important design variables already discussed.

The design procedure which Taylor set down for equally spaced counter-rotating vortex generators can be paraphrased as follows:

(1) Determine the separation point as accurately as possible and the boundary-layer thickness upstream of the separation point.

(2) Locate the generator station anywhere from 10 to 30 times the local boundary layer thickness (at the generator station) upstream of the separation point. Try to keep the distance at least 20 times the boundary layer thickness if possible.

(3) Choose the generator span to approximately 1.2 times the boundary layer thickness ($h/\delta_{VG} = 1.2$).

(4) Choose the airfoil chord to be approximately 1.5 times the span although values from 1.4 to 2.0 will yield good results ($1.4 \leq \ell/h \leq 2.0$).

(5) Space the generators so that the distance between adjacent generators is no less that two nor more than five times the span ($2 \leq (d/h) \leq 5$).

(6) Use the NACA 64-812 airfoil section with an unswept quarter chord and no taper. Employ a chord distribution such that the circulation is constant across the span and thus only a tip vortex would be shed.

(7) Use an angle-of-attack of 16°.

Taylor did indicate that the above criteria would serve as a good starting point for a successful design but experimental testing would be required for further refinements.

In practice, a number of refinements have been made to Taylor's procedure which still resulted in acceptable designs. As already indicated, for many diffuser applications, the scale of the generator precludes any planform other than a simple rectangular planform from being used. Also, airfoil sections other than that which Taylor advocated have been used. In particular, the NACA 0012 airfoil section has often been employed. In addition, angles-of-attack other than 16° have been employed.

One other study involving diffusers which set down some design criteria should be mentioned. Henry, Wood, and Wilbur[29] compared the performance of a conical and an annular diffuser design while

systematically varying the important vortex generator parameters. Their only merit of performance used to compare the vortex generator configurations was the total pressure recovery levels achieved. Also, they considered only evenly spaced counter-rotating configurations.

The results indicated that the optimum vortex generator configuration appeared to be pretty much independent of diffuser type and inlet conditions. They also pointed out that the performance of the diffusers became more sensitive to the vortex tenerator configuration as the inlet speed was increased. That is the performance levels decreased more rapidly as the vortex generator configuration was changed from the optimum configuration.

Their design criteria were as follows:

$$\left.\begin{aligned} \frac{h}{\delta^*_{inlet,2d}} &= 5 \\ \frac{h}{\delta^*_{inlet,2d}} &= 20.8 \\ \frac{h}{\delta^*_{inlet,2d}} &= 15.4 \\ \frac{X_{VG\text{-}sep'n}}{\delta^*_{inlet,2d}} &= 50 \end{aligned}\right\} \qquad (9)$$

Although the criteria differ somewhat from those advanced by Taylor they nevertheless provide a convenient starting point for the design of vortex generator configurations for a given application.

The next section will discuss the details of the experiment conducted which was aimed at gaining a more complete understanding of the vortex generator forced mixing process.

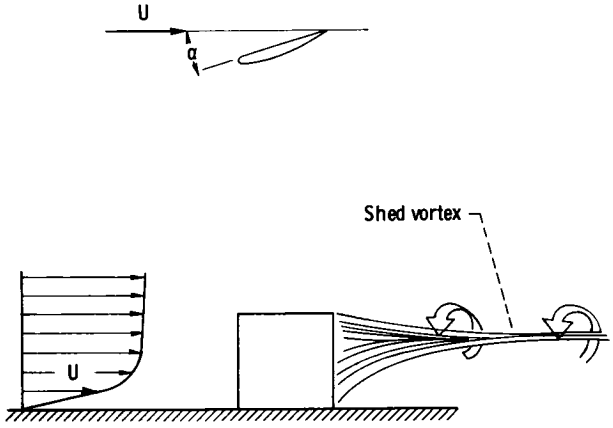

Figure 1. - The vortex generator.

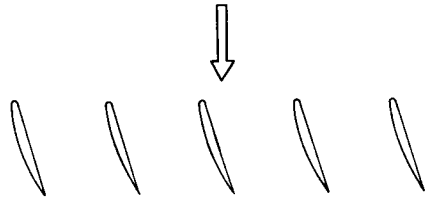

(a) Co-rotating configuration.

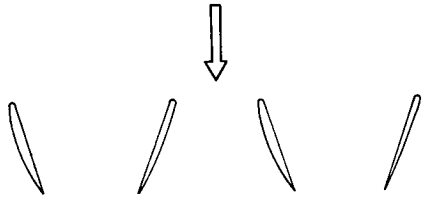

(b) Counter rotating configuration.

Figure 2. - Vortex generator configurations.

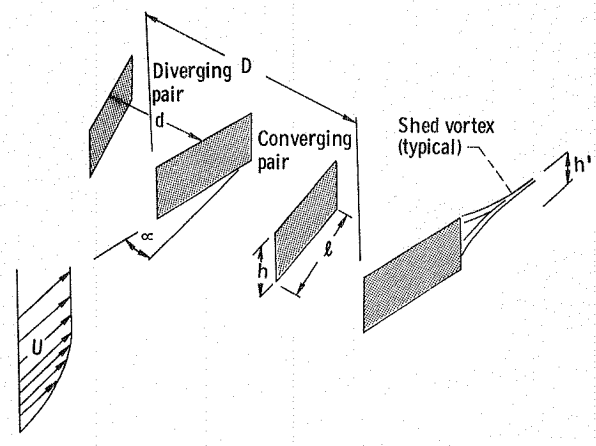

Figure 3. - Vortex generator nomenclature.

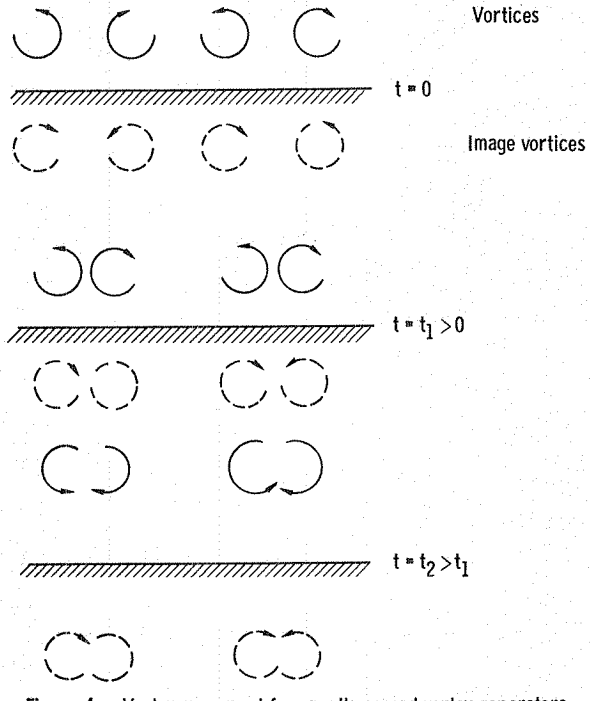

Figure 4. - Vortex movement for equally spaced vortex generators.

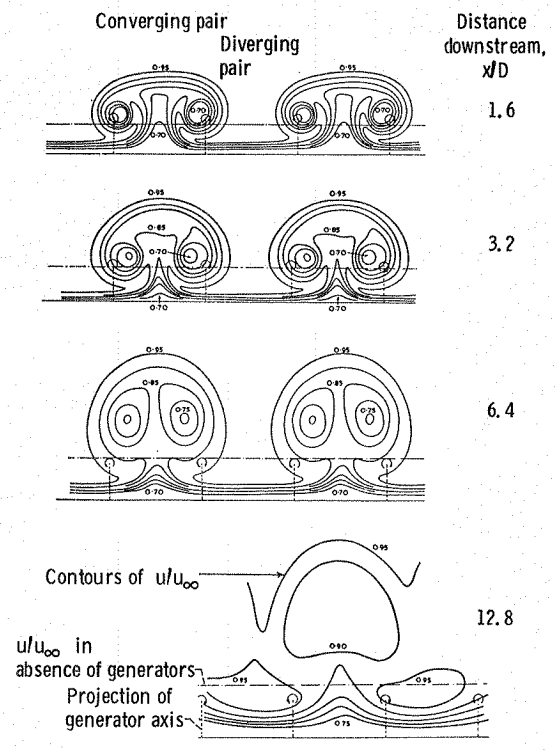

Figure 5. - Velocity contours for counter rotating vortices of equally spaced vortex generators.

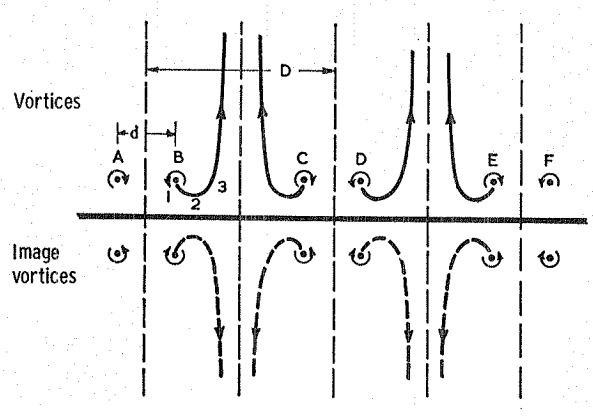

Figure 6. - Vortex movement for unequally spaced vortex generators.

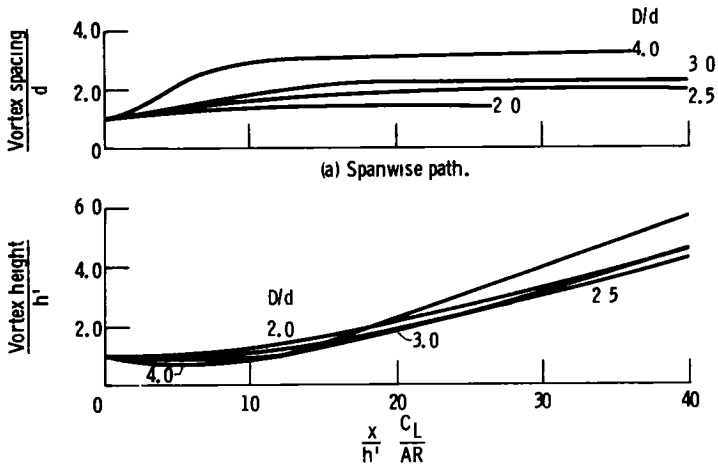

Figure 7 - Paths of vortices for counter rotating vortex generators, $D = 2\pi h'$

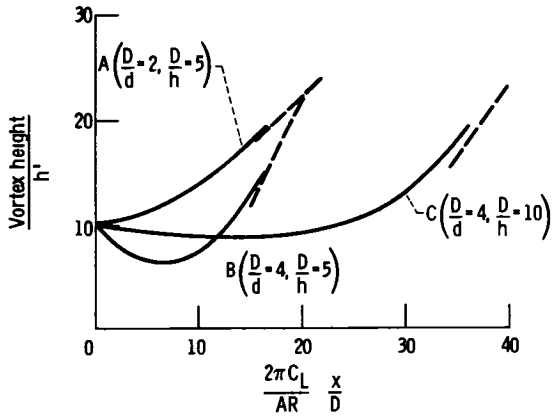

Figure 8. - Paths of vortices for counter rotating vortex generators.

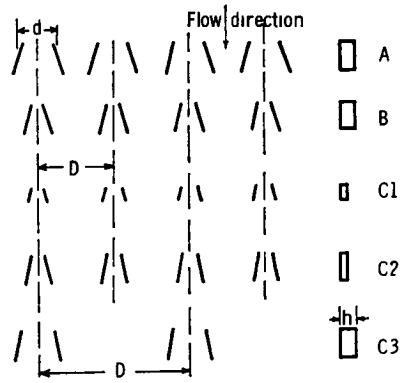

Figure 9 - Vortex generator configurations

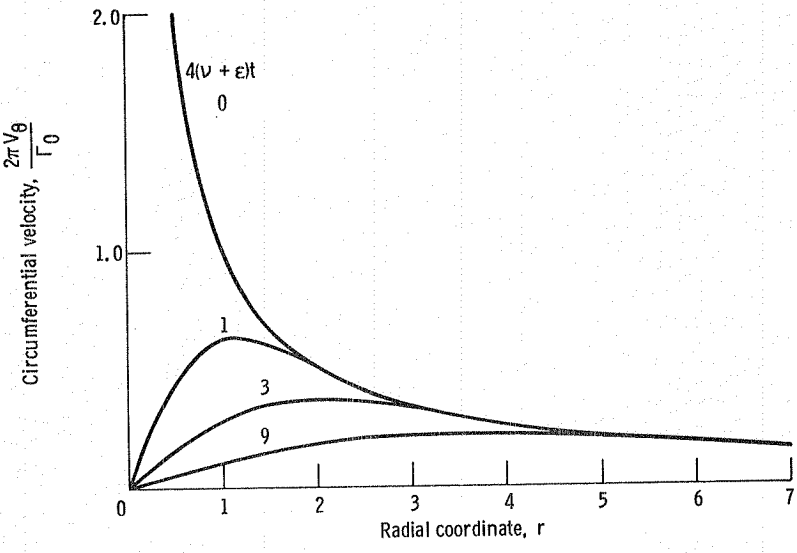

Figure 10. - Vortex strength dissipation due to viscosity.

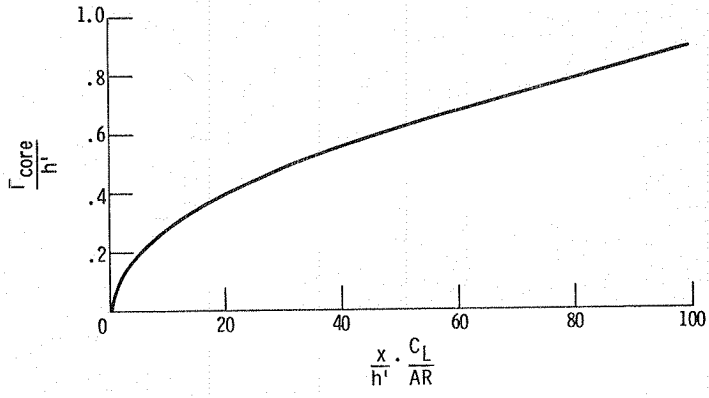

Figure 11. - Effect of turbulent dissipation on vortex size.

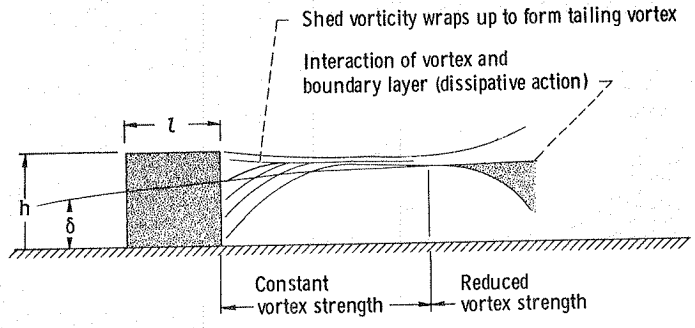

Figure 12. - Vortex-boundary layer interaction.

CHAPTER III

APPARATUS AND PROCEDURE

Diffuser Design and Analytical Prediction of Performance

The forced mixing study was conducted using an annular diffuser design typical of those used with supersonic propulsion systems which employ axisymmetric supersonic inlets. The diffuser chosen was the so-called linear Mach number diffuser. As might be anticipated, the area variation of this diffuser (hereafter referred to as the dM/dz diffuser) is chosen so that the average free stream Mach number will vary linearly in the axial direction. It might be noted that the subsonic diffuser design of the supersonic propulsion system discussed in reference 20 was a dM/dz diffuser.

Much of the actual hardware used for the forced mixing study was identical to that used in an earlier steady state diffuser performance study (ref. 30). The diffuser models were designed to have a constant outer surface radius, that is, to effect an area variation solely through a change in inner surface radius distribution. It was felt that such diffuser designs would be representative of actual flight designs.

Figure 13 shows the contour of the dM/dz diffuser model tested and includes a tabular listing of the inner surface coordinates while Figure 14 shows the area variation of the diffuser.

As Figures 13 and 14 indicate, the axial length of the dM/dz diffuser was 9 inches while the inlet station throat height was 1.5 inches which resulted in a length-to-throat height ratio of 6. The diffuser area ratio (A_{exit}/A_{inlet}) was 2.0 while the equivalent conical expansion angle of the diffuser arc $\tan(R_{exit} - R_{inlet})/L$ was 14.8^{o}.

The incompressible one-dimensional static pressure coefficient variation for a diffuser is given by the following expression.

$$C_{P,1d,inc} = 1 - \frac{1}{\left(\frac{A}{A_{inlet}}\right)^2} \tag{8}$$

The $C_{P,1d,inc}$ variation for the dM/dz diffuser is given in Figure 15.

An indication of the ratio of diffusion for a diffuser can be determined by differentiating the above equation to get

$$\frac{dC_{P,ld,inc}}{dz} = \frac{2\,\frac{dA/A_{inlet}}{dz}}{\left(\frac{A}{A_{inlet}}\right)^3} \tag{9}$$

Since the diffuser exit pressure coefficient is a measure of the total diffusion achieved, the curve of $dC_{P,ld,inc}/dz$ simply shows how the diffusion is apportioned over the length of the diffuser. Figure 16 shows the variation of $dC_{P,ld,inc}/dz$ for the dM/dz diffuser.

As Figures 13 and 14 indicate, the dM/dz diffuser initially has a large radius of curvature and Figure 16 also reflects this fact as the diffusion rate is seen to be initially small but to increase in the downstream direction.

As a point of comparison, Figure 16 compares the diffusion rate variation for the dM/dz diffuser with that for a diffuser which has a constant inner surface slope (a so called dR/dz diffuser). It can be seen that the dR/dz diffuser has a much higher initial diffusion rate than does the dM/dz diffuser, but after approximately one third of the diffuser length, the diffusion rate of the dM/dz diffuser becomes larger than that of the dR/dz diffuser. Thus, it can be said that the dR/dz diffuser accomplishes a larger part of its total diffusion initially while the dM/dz diffuser has a more uniform rate of diffusion. (Note that both diffusers have the same inlet and exit areas and length so that the areas under the two rates of diffusion curves are identical.)

Theoretical performance of the dM/dz diffuser was studied using the finite difference procedure of Anderson.[31] This technique calculates the turbulent, swirling, compressible flow in axisymmetric ducts. The equations of motion are solved in a coordinate system made up of the streamlines and potential lines of the inviscid solution. Boundary-layer type approximations are made in that coordinate system, and the viscous effects are treated as perturbations on the flow. The analysis solves for the entire flow across the duct at each streamwise station. This strong interaction solution eliminates the matching problems of the boundary layer with the potential flowfield.

Figure 17 presents the calculated hub surface skin friction coefficient distributions for three inlet station flow conditions. For purposes of this study, both the hub and tip boundary layers were assumed to have equal displacement thicknesses ($\delta^* = 0.0025$ ft) and to be described by equal values of the power law exponent ($N = 5$). The corresponding values of Reynolds number were representative of experimental levels.

The curves indicate that for all conditions, the hub boundary layer separated about 7 inches downstream of the inlet station ($z = 7$ in.). This general position corresponds with the region of rapid variation in hub surface slope (small values of radius of curvature). It should be pointed out that the tip surface boundary layer showed no tendency toward separation for any of the inlet conditions.

Figure 18 shows the estimated hub surface boundary layer thickness distributions corresponding to the same inlet conditions. For all conditions, the boundary layer buildup became great over the aft end of the diffuser which coincided with the rapid hub surface slope variation.

Vortex Generator Configurations

According to the design criteria of Taylor, the vortex generators should be located upstream of the separation point some 10 to 30 times the boundary layer thickness at the vortex generator station. The generator station was chosen to be 1.3 inches downstream of the inlet station ($z = 1.3$ in.). The corresponding boundary layer thickness was approximately 0.21 inch for an inlet Mach number of 0.70. The range of effectiveness of the generators would be expected to be 2.1 to 6.3 inches or $z = 3.4$ to 7.4 inches which would be an acceptable position. The generators could be located further downstream and still satisfy the axial spacing criterion. However, the required generator height would be greater which would result in larger losses.

Three vortex generator configurations were designed to be tested with the dM/dz diffuser and they are shown in Figure 19. It should be noted that all three configurations had the same airfoil sections - one half an NACA 0012 section with a 0.003 to 0.006 inch radius rounded leading edge. The angle-of-attack of all configurations was 14°.

Configuration I was an evenly spaced configuration ($D/d = 2$) with a half inch chord ($\ell = 0.5$ in.) and a 0.25 inch semi-span ($h = 0.25$ in.). The resultant aspect ratio (h/ℓ) was 0.5.

Configuration II had the same size vortex generators as did configuration I with the only difference being that the converging pairs were further apart ($D/d = 3$).

Configuration III was an evenly spaced configuration like configuration I but the height h and chord ℓ were increased to 0.375 and 0.75 inch, respectively. The aspect ratio remained constant at 0.5.

Recall that Taylor indicated that the parameter h/δ should have a value of about 1.2. Configurations I and II satisfied this criterion but configuration III had a value of 1.79 for this parameter. Thus, the vortex generators of configuration III would protrude relatively far out into the inviscid flow field, and thus the vortex axes would be expected to lie further away from the surface than they would for configurations I and II. However, the larger size of the vortex generators of configuration III would result in stronger shed vortices than those of configurations I and II.

Taylor indicated that the aspect ratio of the generators (h/ℓ) should be between 0.5 and 0.71. All three configurations had values of aspect ratio of 0.5. Taylor also stated that the spacing-to-height ratio (d/h) should have a value between 2 and 5. Configuration I had a value of 3.508, configuration II, 2.340, and configuration III, 2.339.

Thus, it can be seen that configurations I and II satisfied all of Taylor's basic criteria while configuration III satisfied all but the h/δ criterion.

Configuration I was considered to be the baseline vortex generator configuration. Configuration II would indicate the effect of circumferential positioning of adjacent vortex generators. Configuration III would indicate the effects of vortex axes placement relative to the local boundary layer height.

Figure 20 is a photograph of the dM/dz diffuser hub with three vortex generator bands - one for each of the three configurations tested. Each band spanned a 180° circumferential extent so two bands were needed for each vortex generator configuration tested.

Experimental Facility

The forced mixing study described herein was conducted in the CE-22 test facility of the Engineering Research Building (ERB) at the NASA-Lewis Research Center. This building contains a number of test facilities which employ common air supply and exhaust systems. An isometric drawing of the CE-22 facility is shown in Figure 21 while Figure 22 shows a schematic view of the facility.

Air flow through the facility was achieved by independent control of the supply and exhaust pressures. The exhaust pressure was controlled by evacuating or pressurizing the 85-inch-diameter tank which enclosed the experimental apparatus using the altitude exhaust system. The maximum capability of the exhaust system was 26 inches of Mercury which resulted in a flow rate of approximately 35 lbm/sec. The supply air which had a nominal atmospheric temperature had a maximum total pressure of about 40 psig. Figure 23 shows one half of the tank structure rolled back to expose the test rig.

As shown in Figure 22, the supply air passed through a filter prior to reaching the test rig. The filter was included in the system to purify the air of rust contaminants which accumulate in the ERB supply lines. The filter removed all particles of 10 micron diameter and larger. It was felt that if the supply air were not filtered, the measurement probes used could not withstand the environment and major probe breakage problems would occur.

Airflow into the experimental test rig was monitored at the primary air monitoring station shown in Figure 22. This station consisted of 16 total and four static pressure measurements which were used to compute the amount of airflow through the system.

The total temperature of the incoming flow was measured by an iron-constantin thermocouple located slightly upstream of the test section.

After passing through the test section, the airflow was evacuated through the altitude exhaust, also shown in Figure 22.

Figure 24 is a detailed sketch of the test section of the facility indicating the pertinent features. As indicated previously, much of the hardware used in this experiment was used in a previous test which involved a parametric study of the steady state performance of various diffuser designs. The results of that study are discussed in reference 30. This test involved the variation of the diffuser inner surface (hub) contour while retaining the same outer surface (tip) contour.

As Figure 24 shows, the outer surface contour was simply a pipe of constant 12-inch-diameter. Thus, all diffusion was effected by a variation in the hub contour.

The convergent nozzle, throat section, and hub bleed regions are also shown in the figure. The convergent nozzle was simply a hemispherical cap of 4.74-inch-radius while the throat and bleed region was a section of constant 3° slope, 4.80 inches in length.

The hub bleed capability was provided so as to vary the properties of the incoming boundary layer. It consisted of two rows of 0.067 inch diameter normal holes, each row having 300 holes. The centerline of the upstream most row of holes was located 1.25 inches from the diffuser inlet station. The distance between the centerlines of the two rows of holes was 0.082 inch.

The hub assembly was supported by the horizontal pipe and two sets of struts as shown in Figure 24. The hub bleed airflow was ducted through the hollow pipe to the altitude exhaust.

Since the purpose of the experiment was to study the fluid mixing characteristics of vortex generators, it was necessary to

device some means for repositioning the instrumentation circumferentially relative to the vortex generators since the vortices produced result in the local flow being distinctly asymmetric.

Due to space limitations, all instrumentation other than surface static pressures (i.e., total pressure rakes and radially traversing probes) was attached to the outer (tip) surface. A design was accomplished which allowed a portion of the outer surface to be rotated relative to the inner surface and, hence, the instrumentation could be repositioned circumferentially with respect to the hub (and thus to the vortex generators). The movable portion of the outer surface is indicated in Figure 24.

The mechanism which rotated the outer surface is also indicated in Figure 24. A Globe motor powered by a 28 volt DC power supply was controlled by a potentiometer. The Globe motor powered a gear system which rotated the outer surface to the desired position.

The outer surface could be rotated through a 22.5° angular rotation. The rotational system was calibrated in 2.81° increments. O-rings were used to seal the junction between the rotary and stationary portions of the outer surface.

Diffuser Model Instrumentation

The forced mixing study was conducted in two phases. Initially, the diffuser was instrumented with hub and tip static pressure taps, total pressure rakes, and radially traversing boundary-layer total pressure probes. This so-called pressure testing phase was undertaken throughout the inlet Mach number range attainable ($0.15 \leq \bar{M}_{inlet} \leq 0.9$). The intent was to carefully map out the diffuser total pressure fields at various stations downstream of the vortex generators to ascertain the effect of the vortices on the hub boundary layer and thus on the diffuser performance. It was hoped that the paths of the vortices could be deduced from the rake total pressure profiles while the boundary layer total pressure profiles could yield information as to the state of the hub boundary layer.

Following the pressure testing phase, the traversing boundary layer probes were replaced with traversing hot film anemometry probes. Both single and cross film probes were used to measure the turbulent properties of the hub boundary layer - both intensities and shear stresses. The single film probes were also used to determine the mean velocity profiles.

The hot film measurements were made only for a nominal inlet Mach number of 0.3. The inlet Mach number was purposely kept low to avoid the compressibility problems which plague hot wire and hot film probes.

Figure 25 is a detailed layout of the pressure instrumentation It should be noted that the angular notation is counter clockwise looking downstream. The outer surface had 13 surface static pressure taps (labeled TI-TI3). Eight outer surface static pressures (T1-T8) were located in the throat region to detect the presence of a terminal shock system within the diffuser. These eight static pressures were connected to a Mercury manometer to provide an on-line indication of terminal shock existence and location. The inner surface had nine static pressure taps (H1-H9).

A total of five measurement planes were selected to make detailed flow field measurements. These will be noted as stations A, B, C, D, and E, and are shown on Figure 25.

The diffuser inlet flow was measured by a six tube total pressure rake shown as rake A in Figure 25. It should be noted that rake A was located on the nonrotating portion of the outer surface.

Rakes B, C, and D were located 2.75, 4.50, and 7.0 inches downstream of the diffuser inlet station. These rakes were 10 tube total pressure rakes and were located on the rotating portion of the outer surface.

The diffuser exit total pressure profile was measured by a 14 tube total pressure rake noted as rake E on Figure 25. This rake was also positioned on the rotating portion of the outer surface.

Rake E also had a midstream static pressure tap (indicated as MS1 in Fig. 25). This static pressure tube along with the appropriate wall static taps (T13, H9) were used to determine the local static pressure at each total pressure tube location via a linear interpolation scheme.

Figure 26 shows the positions of the total pressure tubes for each of the five rakes. The details of the total pressure probe tip design are also shown. The figure also indicates the nominal (reference) angular position of each of the five rakes. It should be noted that the rakes were offset from one another to avoid any mutual interference effects. As the movable portion of the outer surface was rotated through the 22.5° of allowable motion, the angular positions of the rakes would be increased by 22.5°.

A radially traversing boundary-layer total pressure probe assembly was also positioned at each of the five measuring planes. The probes were offset from the rakes to avoid any mutual interference effects.

Probe A which was fixed in circumferential position like rake A was positioned at 180°. Probes B, C, D, and E, which were located on the movable portion of the outer surface had reference positions of 33.75°, 101.25°, 180°, and 247.5°, respectively.

The details of the total pressure probe tips are shown in Figure 27. The probe tips were flattened to result in an opening width of 0.006 inch. The boundary-layer probes were connected to 50 psi absolute transducers located above the test section to measure the local boundary layer total pressure profiles.

The actuator mechanism used to position both the total pressure and hot film anemometry probes is shown in Figure 28. Note that a cross film anemometry probe is shown installed in the mechanism.

The probe actuator system was a standard closed loop servo-system which consisted of a feedback potentiometer, a so-called set point potentiometer, and a DC motor. The feedback and set point potentiometer voltages (which were opposite in polarity) were summed into a high gain operational amplifier and when the allowable difference in voltage was exceeded, the motor repositioned the probe to a null position (as measured by the feedback potentiometer).

The actuator system featured an automatic stepping sequence circuit which allowed each probe to be stepped 25 times through a given distance with a total of 26 data samples being taken per traverse. A time delay circuit was incorporated which allowed about a 10 second settling time between steps.

The total distance of travel for each probe could be adjusted independently. The individual step sizes were determined for each probe by a series of fixed resistors in series.

Nominal distances of travel for the probes were taken to be 1 inch for probes A, B, C, and D, and 2 inches for probe E. It was felt that these distances would not only allow the local boundary layer profile but also the vortex profile to be surveyed.

The data acquisition sequence for the boundary layer total pressure probes was as follows:

(1) All probes were positioned so that the probe tips were resting on the wall. An electrical contact method was employed which gave a visual indication that the probe tips were indeed touching the wall. The first of the 26 data samples which constituted a probe traverse was taken with the probe tips resting on the surface.

(2) The automatic stepping sequence was initiated which automatically positioned each probe at the positions 2 through 26 which corresponded to the various values of the fixed resistors employed. At each of the steps, a data sample was taken which consisted of each probe position and corresponding total pressure (for each of the five probes).

A pre-run 26 point probe position calibration was undertaken for each of the five probes to ascertain the probe tip position corresponding to each of the 26 steps of the traverse. Probe movement was monitored by a Starrett dial indicator which had an accuracy of 0.001 inch.

A linear interpolation scheme was then employed to determine the probe tip position for each step of the traverse. This was found to be necessary as the probe actuator systems exhibited some drift in positioning from one traverse to the next. While this occurrence was certainly unfortunate it was not felt to be a serious problem.

Since the vortices generated by the vortex generators introduce local asymmetric velocity components and, hence, local flow angularities, it was felt that some knowledge of the magnitude of the flow angularity would be desirable. For this reason, two miniature flow angularity probes were fabricated to be installed at stations B and C.

A schematic of the probe design is shown in Figure 29. The probes were designed to measure the angle of the local velocity vector out of the so-called axisymmetric plane.

In order to measure the complete orientation of the velocity vector, two angles would need to be measured. For such a measurement, a five tube probe tip design would be required. It was felt that the size of such a probe tip would be too great relative to the size of the boundary layer to make such measurements meaningful. Also, it was felt that the measurement of only the one angle would yield sufficient information.

Radial traverses were made with the angularity probes in the same manner as already discussed for the boundary layer total pressure probes.

A more complete discussion of the flow angularity probes is given in Appendix A.

As already indicated, the second phase of the test involved the use of commercially fabricated hot film anemometry probes to map out the variation in turbulence properties of the flow field at the same axial stations which the total pressure measurements were made. Turbulence data were taken only at a nominal inlet Mach number of 0.3. This Mach number was felt to be high enough so that the mixing action of the vortices would be present but still low enough so that the compressibility effects on the hot film sensors could be ignored.

Both single and cross film probes were used. The single film probes were used to measure the axial turbulent intensity and mean velocity profiles while the cross film probes were used to measure

the Reynolds turbulent shear stress profiles. No cross film probe was installed at the diffuser inlet station A as it was felt that the boundary layer height was too small relative to the probe size to make meaningful measurements.

The hot film probes used in this study were manufactured by Thermo Systems Incorporated (TSI), St. Paul, Minnesota. Figure 30 shows the pertinent details of the probes used. Both probe models used had a sensor diameter of 0.002 inch. The single film probes used were Model 1261 while the cross film probes used were Model 1249 The probes were specially manufactured so that the orientation of each probe matched the local surface slope of the diffuser contour

Hot film sensors were used rather than the smaller diameter hot wire sensors since it was felt that the particulate matter in the incoming flow would present breakage problems for the more fragile wire sensors.

Even though the hot film sensors had a lower frequency response than did the hot wire sensors, it was felt to be adequate for the study in question.

TSI Model 1050 anemometer modules were used with the hot film probes. The probes were operated at an overheat ratio of 1.5. No linearizers were employed in the set up and operation of the hot film probes. A complete discussion of the hot film probe calibration technique employed as well as the data reduction equations used is given in Appendix B.

To facilitate the acquisition of the large amounts of hot film data acquired, an analog computer was employed to process the raw analog signals into forms suitable for data reduction. A complete discussion of the analog computer circuitry is given in Appendix C.

The data acquisition procedure was basically the same for the hot film probes as it was with the boundary layer total pressure probes with one difference. The hot film probes could not be allowed to touch the wall as sensor breakage would occur. Rather the probes were manually positioned as close to the wall as appeared safe and the distances of the sensors from the local surface were measured using a ruler and transit.

The rest of the procedure including the position calibration technique was the same.

As already indicated, the movable outer surface was designed to allow the instrumentation to be repositioned with respect to the vortex generators. The outer surface could be rotated through a 22.5° angular variation which allowed the instrumentation to be positioned at any point with respect to the vortex generators.

Measurements were made every 0.94°, that is, 25 profiles were taken spanning the 22.5° circumferential extent of two consecutive vortex generator pairs. It was felt that such a number of profiles would adequately map out the local flow field at each measurement station. An implicit symmetry assumption was made, i.e., the flow field between adjacent-like pairs of vortex generators would be similar.

Figure 31 indicates the relationship of the actual measurement locations for each rake and traversing probe to the vortex generator locations for the three configurations tested. For instrumentation planes B and C, the reference position was midway between a diverging pair of vortex generators. For instrumentation planes D and E, the reference position was midway between a converging pair of vortex generators.

It should be noted that for the evenly spaced vortex generator configurations, both converging and diverging pairs were spaced 11.25° apart. For the unevenly spaced configuration, the converging pairs were spaced 15° apart while the diverging pairs were spaced 7.5° apart.

Data Acquisition and Reduction Procedures

All the data obtained during the test was recorded by the NASA-Lewis Central Automatic Digital Data Encoding System (CADDE) and then processed into a usable engineering format by an IBM 360 digital computer using a specially prepared data reduction program. The static and total pressures (with the exception of the traversing boundary-layer probe pressures) were measured using four 48 port scannivalves each of which had a 50 psia transducer.

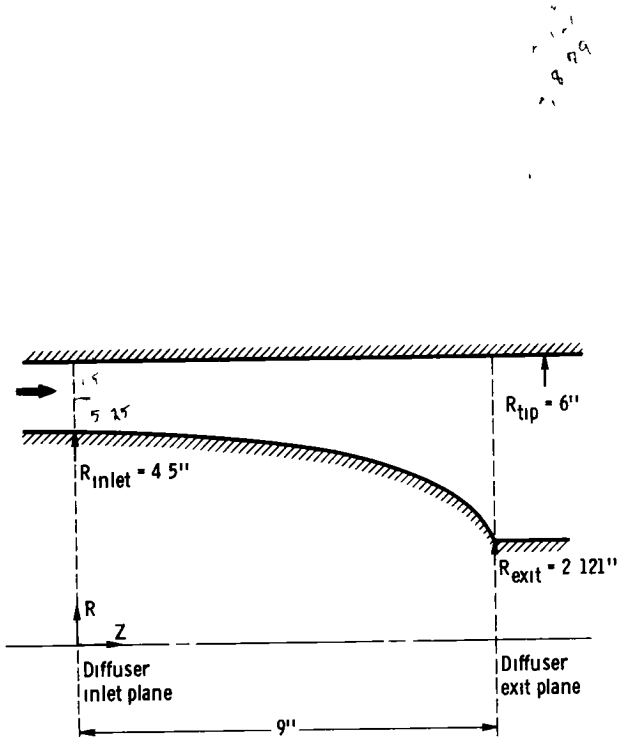

Z in	R in
0.000	4.500
.420	4.486
860	4 469
1.080	4.460
1 300	4.449
1 740	4.424
2 180	4.396
2.620	4.362
3 060	4 324
3 500	4.279
3 940	4.228
4.380	4.168
4.820	4.100
5 260	4.020
5 700	3 927
6 140	3 818
6 580	3 688
6.800	3 614
7 020	3 533
7.240	3.443
7 460	3.343
7 680	3 232
7 900	3.108
8 120	2 966
8 340	2.804
8 560	2 616
8 780	2 393
9 000	2 121

Figure 13. - Geometry of dM/dZ diffuser model

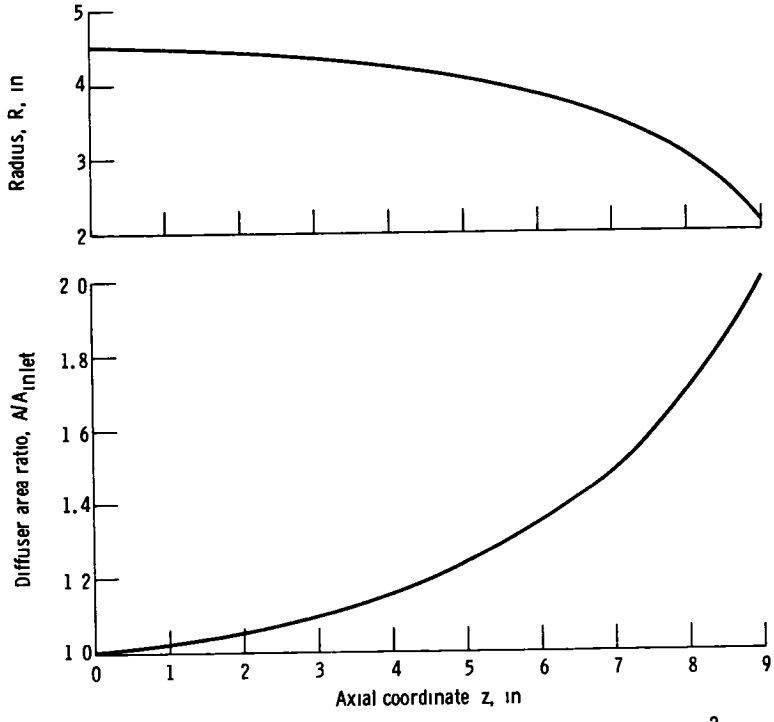

Figure 14 - Diffuser radius and area variations A_{inlet} = 49 48 in ^{2}

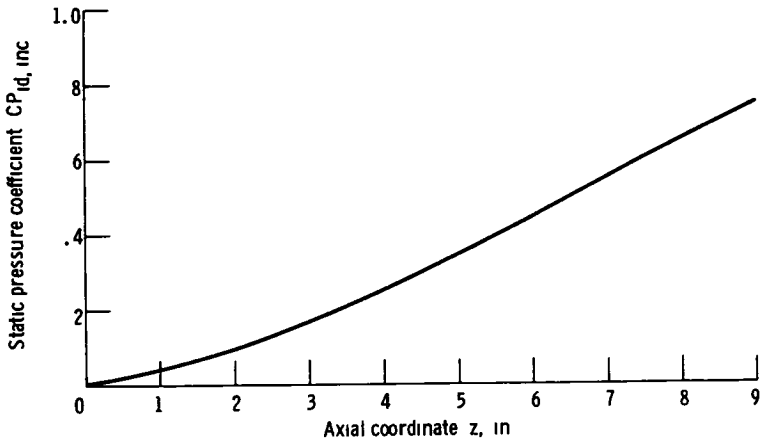

Figure 15 - Theoretical incompressible static pressure coefficient variation

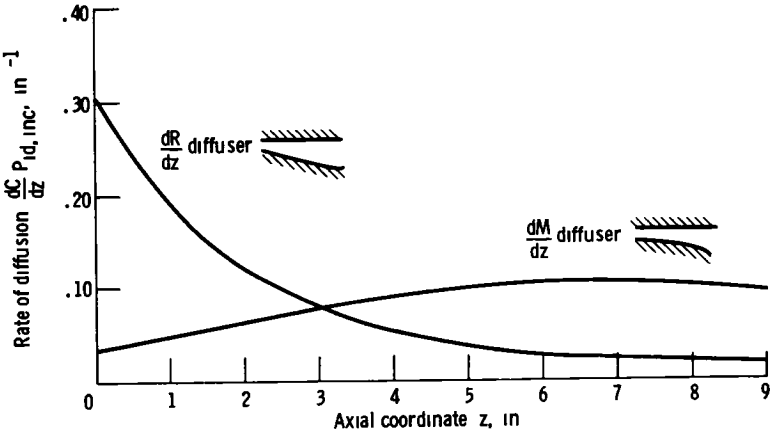

Figure 16 - Variation of rate of diffusion for two diffuser designs

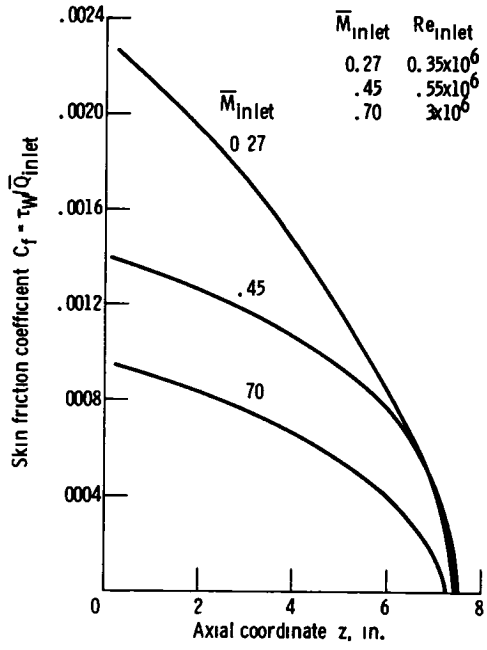

Figure 17 - Predicted hub surface skin friction distributions δ^*_{inlet} = 0.0025 ft, N = 5.

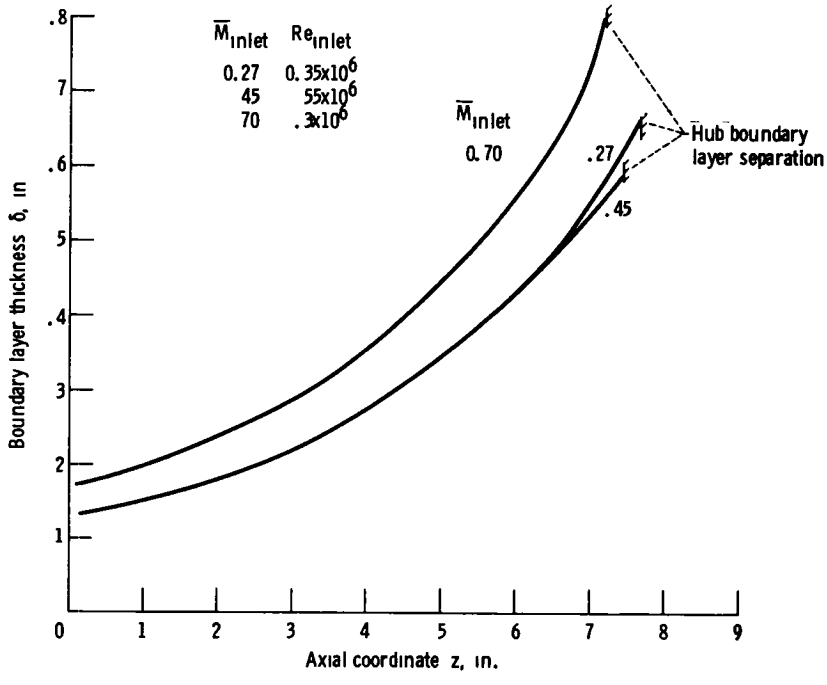

Figure 18. - Estimated hub boundary layer thickness distribution δ^*_{inlet} = 0 0025 ft, N = 5

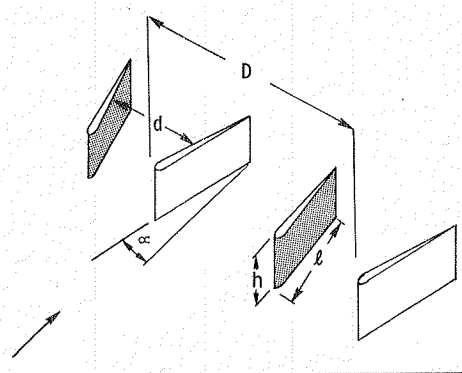

Configuration	ℓ	h	D	d	δ	$\frac{h}{\delta}$	$\frac{D}{d}$	$\frac{d}{\ell}$	$\frac{D}{\ell}$	$\frac{h}{\ell}$	$\frac{D}{h}$	$\frac{d}{h}$
I	0.5	0.25	1.754	0.877	0.21	1.19	2	1.754	3.508	0.5	7.016	3.508
II	.5	.25	1.754	.585	.21	1.19	2	1.169	3.508	.5	7.016	2.340
III	.75	.375	1.754	.877	.21	1.19	2	1.169	2.339	.5	4.677	2.389

Figure 19. - Vortex generator configurations.

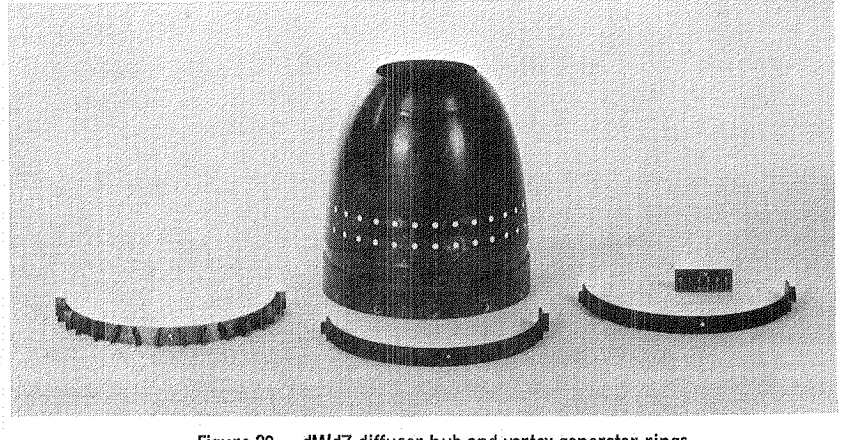

Figure 20. - dM/dZ diffuser hub and vortex generator rings.

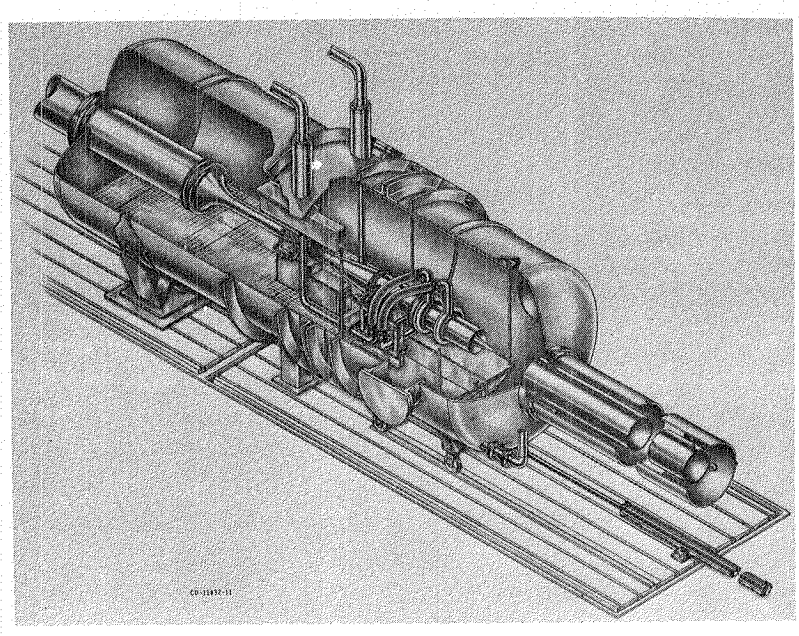

Figure 21. - Isometric view of CE-22 test facility.

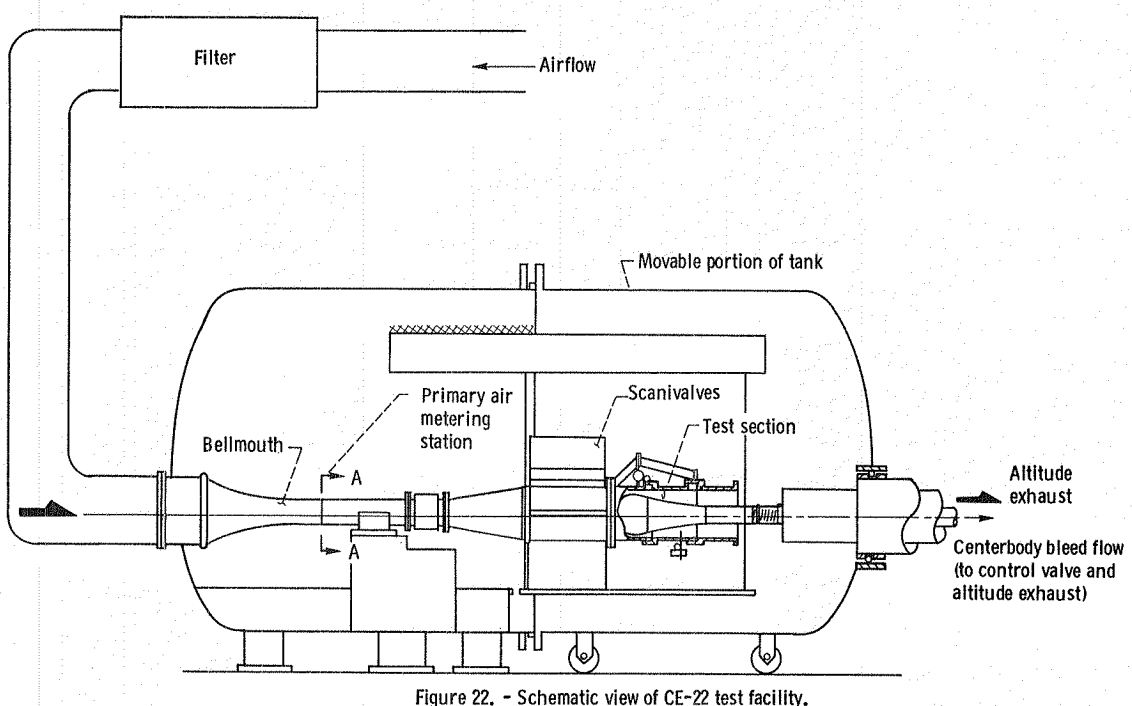

Figure 22. - Schematic view of CE-22 test facility.

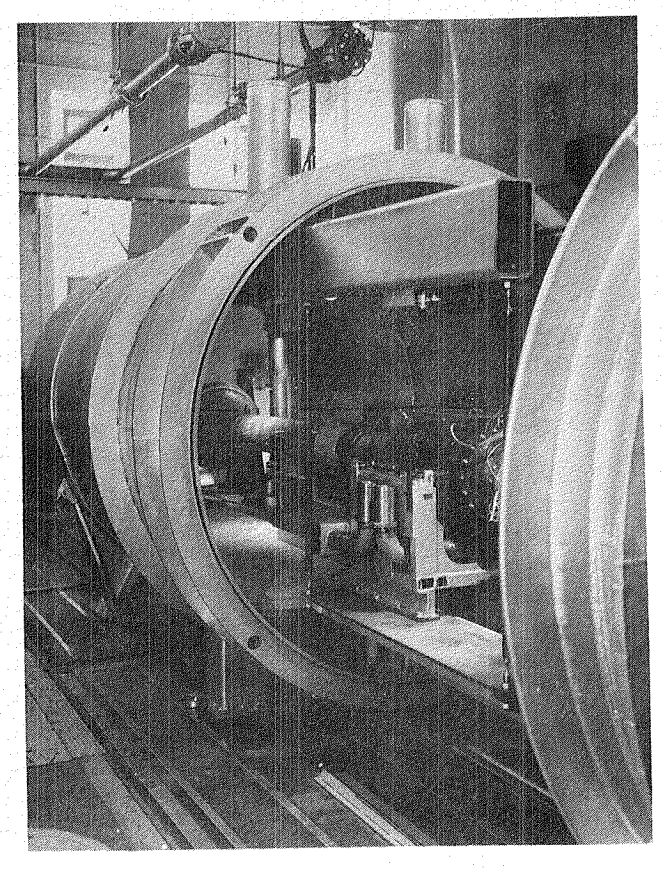

Figure 23. - CE-22 test facility with tank rolled back.

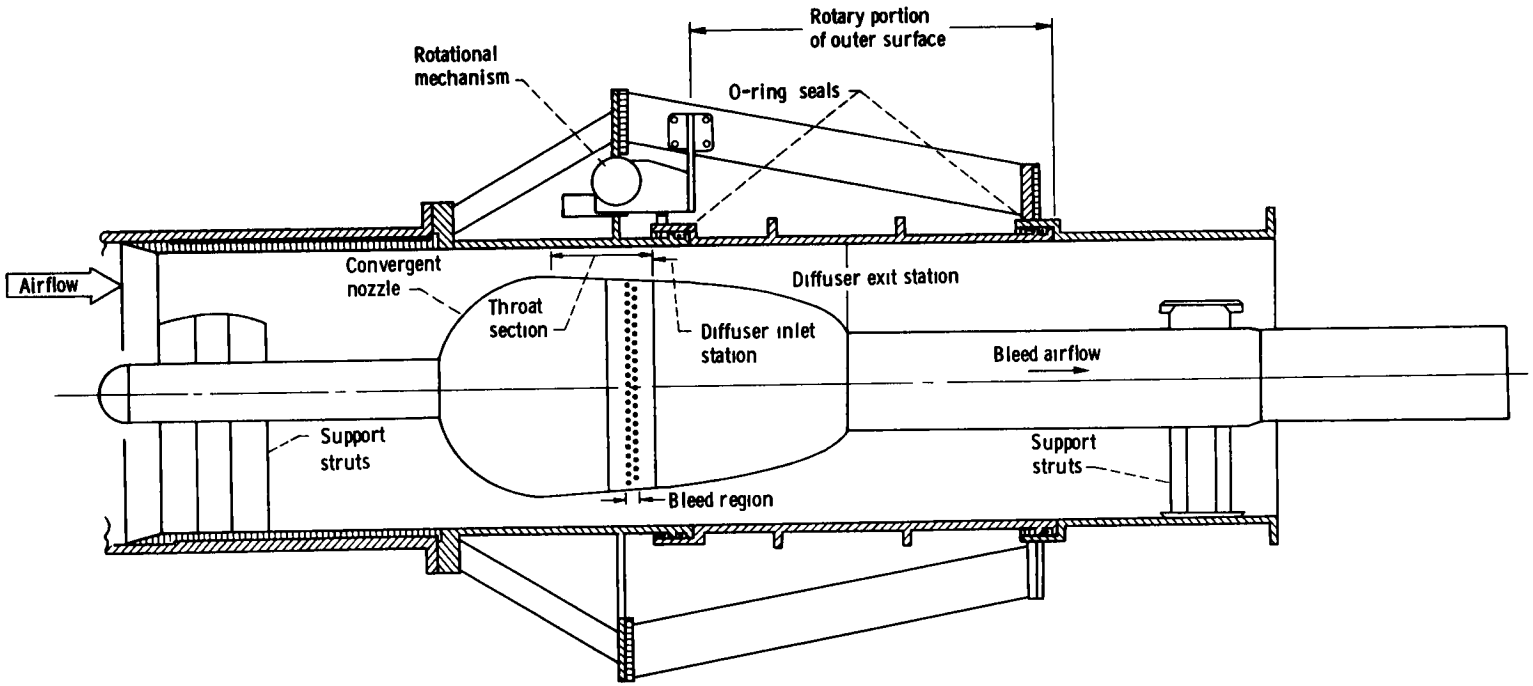

Figure 24. - CE-2 diffuser test section details

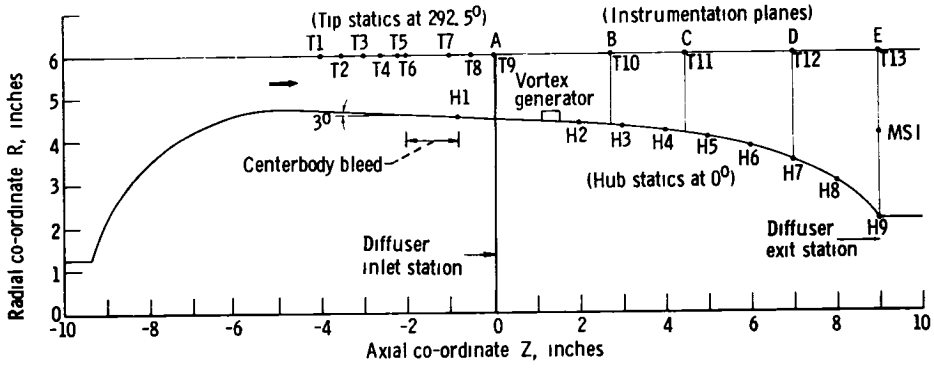

Figure 25 - Diffuser test section instrumentation

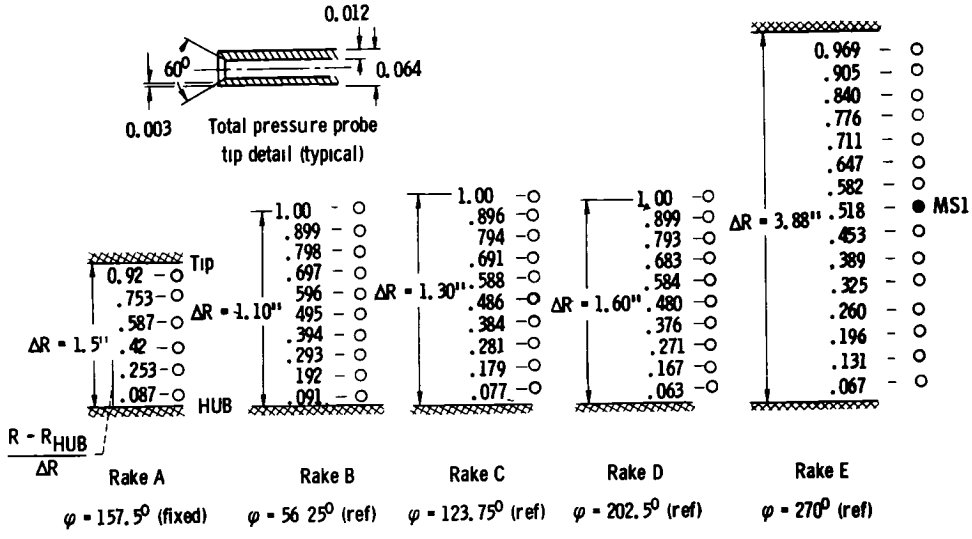

Figure 26 - Diffuser total pressure rake dimensions

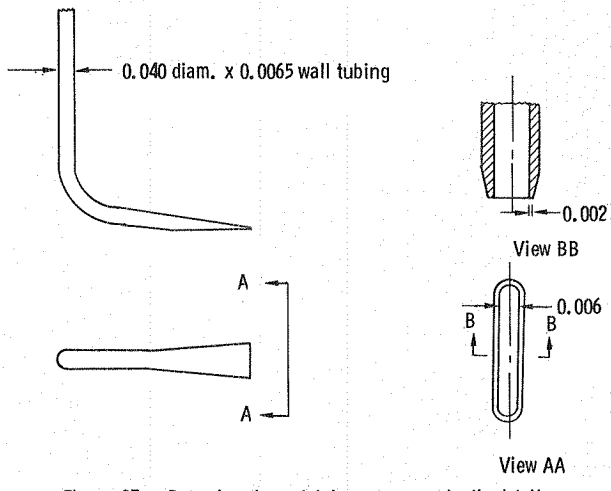

Figure 27. - Boundary layer total pressure probe tip details (all dimensions shown are in in.).

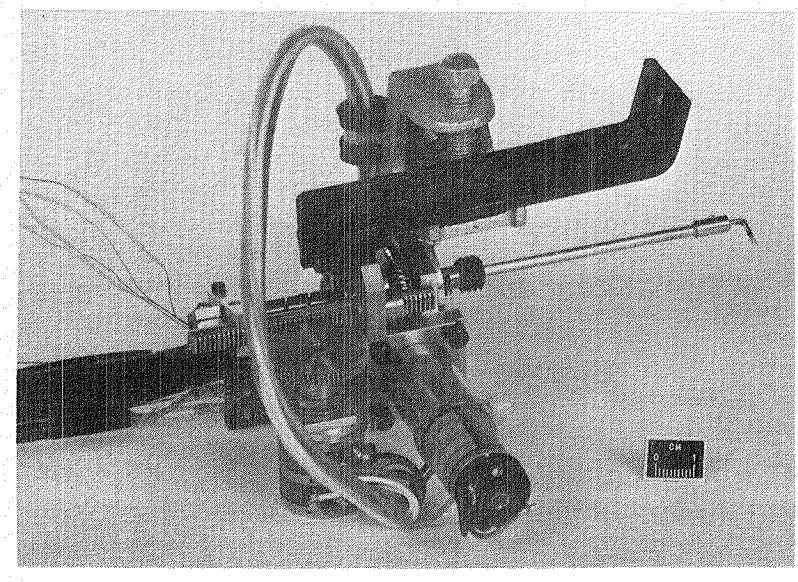

Figure 28. - Boundary-layer probe actuator.

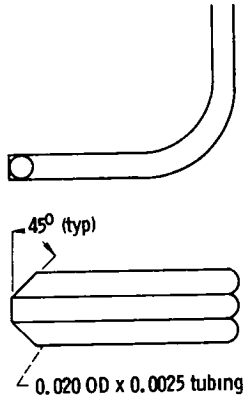

Figure 29. - Flow angularity probe details (all dimensions shown are in in.).

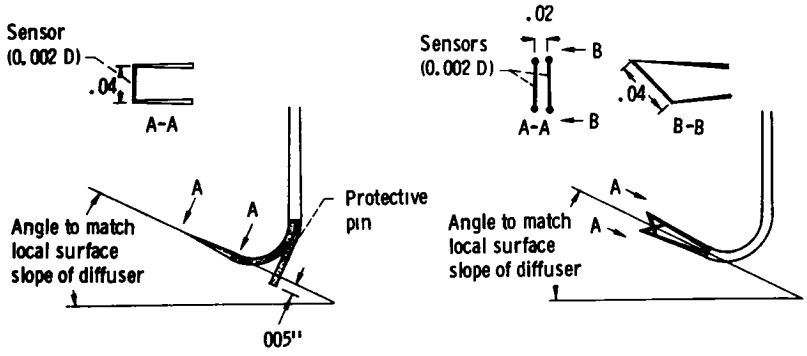

(a) Single film probe.

(b) Cross film probe.

Figure 30. - Hot film anemometry probe details (all dimensions shown are in in.).

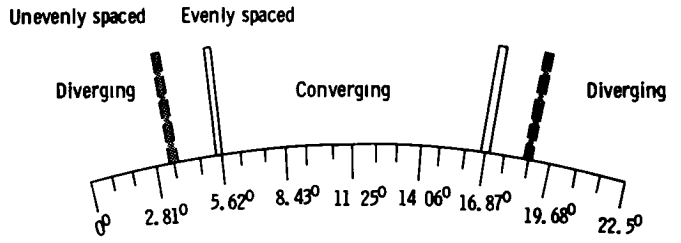

Instrumentation plane B
Axial location 2.75 in.
Local hub radius 4.33 in.
Rake angular location 56.25° (ref)
Traversing probe angular location 33.75° (ref)

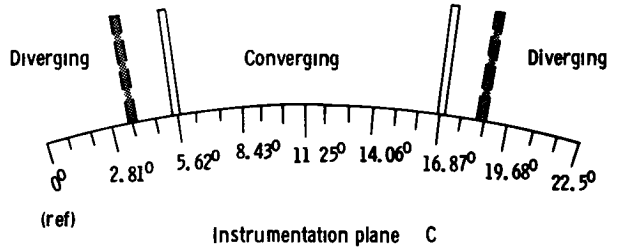

Instrumentation plane C
Axial location 4.50 in.
Local hub radius 4.14 in.
Rake angular location 123.75° (ref)
Traversing probe angular location 101.25° (ref)

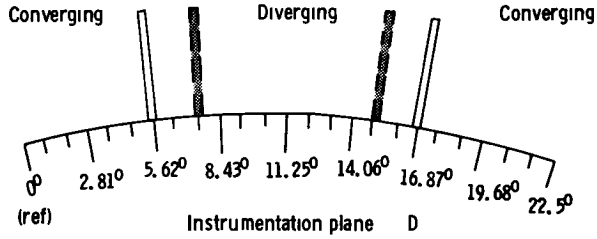

Instrumentation plane D
Axial location 7 00 in.
Local hub radius 3.50 in.
Rake angular location 202 5° (ref)
Traversing probe angular location 180° (ref)

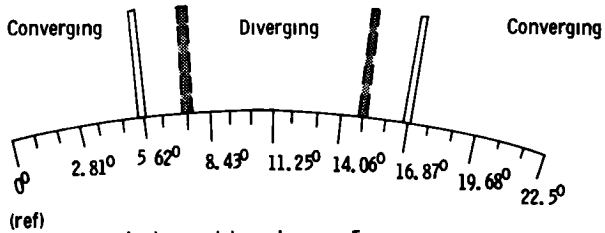

Instrumentation plane E
Axial location 9.00 in.
Local hub radius 2.12 in.
Rake angular location 270° (ref)
Traversing probe angular location 247.5° (ref)

Figure 31. - Instrumentation locations relative to vortex generators.

CHAPTER IV

RESULTS AND DISCUSSION

dM/dz Diffuser Performance with no Vortex Generators Installed

The overall performance of the dM/dz diffuser is presented in Figures 32 and 33 as the area weighted total pressure recovery and total pressure distortion as functions of the average inlet Mach number ($\bar{M}_{inlet}$). The recovery was in excess of 0.99 for inlet Mach numbers of 0.3 and less. As the inlet Mach number was increased beyond 0.3 the recovery continually decreased and reached a value of about 0.95 for an inlet Mach number of 0.65. A slight increase in recovery was then noted followed by a continuing decrease.

The distortion was roughly a linear function of inlet Mach number reaching a value of 0.15 for an inlet Mach number of 0.7.

Reference 30 attributed this increase in recovery to a reduced skin friction in the region of the terminal shock. Reference 30 also indicated that a normal shock (or shock train) occurred upstream of the diffuser inlet station as indicated by the tip surface static pressure distributions.

Figure 34 shows several tip surface static pressure distributions in the diffuser throat region for inlet Mach numbers between 0.58 and 0.75. The presence of an upstream shock can be seen for inlet Mach numbers of 0.66 and higher. As the inlet Mach number was increased, the shock moved downstream toward the diffuser inlet station.

To paraphrase reference 30, the integrated skin friction coefficient over the shock-boundary layer interaction region was less than the corresponding quantity for an undisturbed boundary layer. This decrease in skin friction was manifested as an increase in diffuser exit total pressure recovery.

The diffuser inlet station velocity profiles shown in Figure 35 for the same operating condition as shown in Figure 34 reveal that the occurrence of the diffuser shock system also resulted in a distortion of the inlet profile in the region near the hub surface. The distortion became more severe as the inlet Mach number was increased.

The diffuser performance did not appear to be degraded by the inlet profile distortion. That is the total pressure recovery actually increased slightly while the total pressure distortion showed no change in trend.

Figure 36 shows the static pressure distributions for both the hub and tip surfaces for a range of inlet Mach numbers. It should be noted that the Reynolds number was not held constant for the various conditions shown. The inlet Mach number was set by simultaneously adjusting the upstream supply total pressure level and the downstream vacuum exhaust pressure level. The inlet Mach number was monitored by a control room readout which displayed the ratio of the supply pressure to a static pressure at the diffuser inlet station.

The tip static pressures increased continually from diffuser inlet to exit station. The hub static pressures increased only to about 7 inches from the inlet station where a leveling off or even a slight decrease occurred. This abrupt change in static pressure is indicative of possible boundary layer separation from the hub surface. This result is in qualitative agreement with the analytical performance predictions already presented. Also the abrupt change in static pressure occurred for all conditions shown. The tip surface static pressure distributions gave no indication of any boundary layer separation being present for any inlet Mach number.

Figure 37 shows the rake total pressure profiles for the five measurement planes (stations A, B, C, D, and E) for three inlet Mach numbers ($\bar{M}_{inlet}$ = 0.29, 0.48, and 0.75) presented in the form of U/U_{max} where the maximum velocity is the maximum measured value for each of the five rakes.

A constant static pressure was assumed for rakes A, B, C, and D for purposes of converting the measured pressures to velocities. For each measurement plane, the appropriate hub and tip static pressures were averaged to yield a representative value. If a static pressure was not measured on the hub surface at the appropriate axial position, a linear interpolation of adjacent measured pressures was employed. For rake E a linear interpolation of the three measured static pressures was employed to determine the static pressure at the position corresponding to each total pressure measurement.

The velocity profiles for the three operating conditions chosen show the same qualitative results. The initially small amount of diffusion was reflected in profiles B and C which shown an essentially uniform channel flow and an apparently thin hub surface boundary layer. However, the profiles at station D indicate a rapid thickening of the boundary layer while the diffuser exit profiles (station E) show a separated hub surface boundary layer. The separated zone appeared to be anywhere from 20 to 40 percent of the diffuser exit channel height.

Again the results are in qualitative agreement with the analytical predictions of performance already discussed. The hub surface boundary layer was well behaved until station D where a rapid thickening and subsequent separation occurred. This reflects the rapid variation in curvature which occurs near the exit of the diffuser.

An inspection of the velocity profiles for the inlet Mach number of 0.75 reveals that the inlet profile distortion already discussed appeared to be completely dissipated by station C. This could explain why the dM/dz diffuser appeared to be tolerant to inlet profile distortion. The initial length of the diffuser had little area variation and thus sufficient natural mixing could occur in this region to essentially smooth out the profile.

The boundary layer profiles corresponding to the same three inlet Mach numbers already discussed are presented in Figure 38. The profiles corresponding to an inlet Mach number of 0.29 were measured with the single film anemometry probes while the profiles corresponding to the inlet Mach numbers of 0.48 and 0.75 were measured with the boundary layer total pressure probes. (An identical scheme to that discussed above was used to determine the static pressure for use in reducing the measured total pressure profiles to velocity profiles.)

For all three inlet Mach numbers, the boundary layer profiles indicate the same trends as shown by the total pressure rake profiles already discussed. For all conditions, the inlet profile indicated a well behaved hub surface boundary layer. The presence of a terminal shock system ($\bar{M}_{inlet} = 0.75$) appeared to thicken the boundary layer as would be expected, but no significant profile distortion could be detected.

Profiles corresponding to stations B and C showed a gradually thickening boundary layer but again no profile distortion could be detected. However, profiles measured at station D showed a thick, distorted profile. In particular, the profile corresponding to $\bar{M}_{inlet} = 0.48$ revealed a peculiar behavior which was possibly a transitory separation.

The velocity profile at station E is not presented for any of the three inlet conditions since the rake profiles indicated a separated zone was present.

Figure 39 presents the pertinent parameters for the hub surface boundary layer as determined from the boundary layer profiles already presented. The displacement and momentum thicknesses are two-dimensional values. The compressible versions were calculated for the velocity profiles derived from the total pressure probe measurements ($\bar{M}_{inlet} = 0.48$ and 0.75) while the incompressible version was

calculated for the velocity profiles derived from the hot film anemometry probes ($\bar{M}_{inlet}$ = 0.29). The shape factor was simply the ratio of the displacement to momentum thicknesses.

The skin friction distributions were determined using the Clauser plot analysis technique. This analysis assumes the boundary layer obeys the universal law of the wall. The Clauser plot analysis strictly applies only for an incompressible turbulent boundary layer. However, the analysis was extended to the two cases of inlet Mach number where the flow was obviously compressible. The aim was simply to show approximate trends in wall shear stress rather than obsolute levels. A more complete discussion of this technique is given in Appendix D.

The boundary layer property variations indicate the hub surface boundary layer grew at a slow rate over the first half of the diffuser length (stations A to C). Both integral thicknesses appeared to approximately double while the shape factor remained essentially unchanged indicating no appreciable profile distortion had occurred.

However, at station D, the integral thicknesses were 3 to 4 times greater than the corresponding values at station C. Also the shape factor increased by about 40 to 50 percent indicating significant boundary layer profile deterioration had occurred between stations C and D.

The skin friction distributions indicate ordered reductions in level up to station C but followed by a rapid reduction between stations C and D. The profiles at station D were so distorted that the skin friction coefficient levels shown are only "best guesses" from the Clauser plots. It is doubtful that such distorted profiles would even follow a law of the wall variation.

Thus it can be stated that regardless of inlet Mach number, the hub surface boundary layer was well behaved over approximately the first half of the diffuser length. However, rapid profile deterioration then occurred and the hub surface boundary layer separated some place in the vicinity of station D (7 in. downstream of the diffuser inlet station). The separated zone was on the order of 20 to 40 percent of the channel height at the diffuser exit station.

Figure 40 presents the measured boundary layer profiles for stations A, B, C, and D for an average inlet Mach number of 0.29. No profiles are presented for measurement plane E. For stations B, C, and D, profiles of mean velocity, axial turbulence intensity, and Reynolds shear stress are presented. Each turbulence quantity is nondimensionalized by the average inlet velocity U_0 while the mean velocity is nondimensionalized by the appropriate maximum measured mean velocity. For station A only the mean velocity and

axial turbulence intensity profiles are shown as no shear stress profiles were measured for that station.

The profiles are in qualitative agreement with those presented elsewhere for conical diffusing flows[32-33] and two-dimensional diffusing flows.[34] The inlet station A axial turbulence intensity profile had a maximum value of about 8 percent, which occurred very close to the hub surface. However, the axial intensity profiles for stations B, C, and D had maxima which were displaced further from the hub surface as the boundary layer flow proceeded downstream. The maximum turbulence intensity measured at station D was about 15 percent and was located over 0.2 inch away from the hub surface.

The Reynolds shear stress profiles showed trends similar to those exhibited by the axial intensity profiles. That is as the hub surface boundary layer proceeded downstream against the imposed adverse pressure gradient, the level of Reynolds shear stress increased and the location of the maximum moved away from the hub surface.

The increase in level of both the axial turbulence intensity and Reynolds shear stress between stations C and D, as well as, the corresponding mean velocity profile degradation indicates the hub surface boundary layer did deteriorate over the aft end of the diffuser.

The fact that boundary layer deterioration occurred over the aft end of the diffuser indicates that vortex generators should be useful in retarding separation since a sufficient axial length would be available for vorticity rollup and subsequent forced mixing to occur.

A quantity often used to describe the level of turbulent mixing present within a boundary layer is the eddy viscosity coefficient ε which is an analogous fashion to the laminar viscosity coefficient relates the local mean velocity gradient to the local fluid stress level present. However, the value of the eddy viscosity coefficient must be determined from experimental data since its value cannot be determined from theoretical considerations.

Clauser[35] determined that for incompressible, flat plate, zero pressure gradient boundary layer flows, the eddy viscosity in the outer portion of the boundary layer could be described by

$$\frac{\varepsilon}{\delta^* U_e} = 0.016 \tag{10}$$

Such a correlation has been used in many turbulence models to predict the characteristics of many more general boundary layer flows and as such its usage is often viewed to be a reasonable engineering approach.

Prandtl formulated the mixing length concept to describe the turbulent mixing process by drawing an analogy with the kinetic theory of gases. The basic governing relation is:

$$\varepsilon = \ell^2\left(\left|\frac{\partial u}{\partial y}\right|\right) \tag{11}$$

where ℓ is the mixing length, and it must be determined from experimental data. In the outer regions of the flat plate boundary layer, experimental data has indicated that the ratio of the mixing length to some convenient boundary layer thickness (δ, δ^*, or θ) is approximately a constant.

Again this correlation strictly holds only for a flat plate (zero pressure gradient) boundary layer although it has also been used in turbulence models to predict more generalized boundary layer flows. As such, the assumption of a constant nondimensional mixing length is also viewed to be a reasonable engineering approach.

Turbulence models which rely upon either of the two correlations described above rely upon a different modeling of turbulent mixing in the near wall region where the relative importance of the physical processes occurring within the turbulent boundary are different than they are in the outer region. As such the turbulence models are termed two layer models.

Figures 41 and 42 present the nondimensional eddy viscosity and mixing length distributions calculated from the Reynolds shear stress and mean velocity profiles already presented for stations B, C, and D. Inaccuracies in the absolute levels of these quantities are undoubtedly present as data from two separate measurements had to be combined to achieve the desired result. A cubic fit of the mean velocity profile was used to generate the required spatial derivative and this may be the largest source of error. Nevertheless general trends and levels should be discernible.

The nondimensional eddy viscosity profiles for all three stations show that the level was not constant across the boundary layer as the Clauser model suggests. For each station, the eddy viscosity level near the hub surface was significantly less than 0.016 but exceeded that value in the outer region of the boundary layer. These trends are similar to those shown in reference 32 for a conical diffuser operating in a state of incipient separation.

A reference 32 points out the assumption of constant nondimensional eddy viscosity underestimates the actual outer region turbulent mixing level present since a larger value of the constant

indicates an increased mixing level present. Similarly the actual mixing level present in the inner region of the boundary layer was less than the level assumed by the Clauser model.

The mixing length distributions shown in Figure 42 were nondimensionalized by the appropriate boundary layer displacement thickness. The experimentally determined distributions indicate that the assumption of constant nondimensional mixing length was not verified. The experimental distributions show mixing lengths which continually increased with distance from the hub surface. Comparison of the three profiles (stations B, C, and D) indicates that the nondimensional mixing length was reduced as the hub boundary layer proceeded downstream.

These trends were noted for similar measurements made in an annular diffuser and discussed in reference 36 where it was postulated that the reduction in level of mixing length was due to the shear stress distribution lagging behind the development of the mean velocity profile.

The eddy viscosity and mixing length models were formulated from data for zero pressure gradient boundary layer flows which are examples of equilibrium boundary layer flows. Equilibrium boundary layer flows are those for which the transport effects are small and as such only the local characteristics are important in describing the boundary layer. The diffuser flow is definitely one for which transport effects are important in describing the boundary layer.

The levels of eddy viscosity and mixing length shown in Figures 41 and 42 will be compared with the levels present with vortex generators installed to ascertain the forced mixing effects.

dM/dz Diffuser Performance with Vortex Generators Installed

Overall diffuser performance is generally presented in terms of static pressure recovery, total pressure recovery, or total pressure distortion at the diffuser exit station as a function of some inlet station variable. Comparisons of the diffuser performance with the three vortex generator configurations installed are shown in Figures 43 to 49. Figure 43 shows the average exit static pressure coefficient variation with average diffuser inlet Mach number. The exit and inlet static pressures were simply taken to be an average of the appropriate hub and tip values. The static pressure difference was nondimensionalized by the average inlet dynamic pressure. All three vortex generator configurations provided significant increases in the exit static pressure over the complete Mach number range. The increase in static pressure coefficient was about 0.1 for all inlet Mach numbers.

The differences between the configurations were less distinct. For inlet Mach numbers of about 0.67 and less configuration II provided a small increase (about 0.01) over the other configurations. Above a Mach number of 0.67 configuration III had static pressure coefficient levels of about 0.05 greater than the other configurations.

The diffuser exit total pressure recovery performance for the three configurations is shown in Figures 44 to 46. A comparison of these figures with Figure 32 indicates that the total pressure recovery levels were about 0.005 higher for the vortex generator configurations than for the no vortex generator configuration especially over the higher inlet Mach number range. The differences were less noticeable for the lower inlet Mach numbers since the diffuser recovery tended to be very high (in excess of 0.99). No noticeable differences in recovery between the various vortex generator configurations could be detected.

The figures also indicate that the inclusion of the vortex generators resulted in the disappearance of the hump in total pressure recovery for inlet Mach numbers around 0.65 which was already discussed.

The diffuser exit total pressure distortion variation with inlet Mach number is shown in Figures 47 to 49 for the three vortex generator configurations. A comparison with Figure 33 for the no vortex generator configuration reveals that in a similar manner to the total pressure recovery, as the inlet Mach number was increased, the vortex generators were successful in reducing the level of distortion. The reductions were as much as 2 to 3 percent.

Slight differences between the three configurations could be detected especially at the higher Mach numbers. For inlet Mach numbers of about 0.7 and above, the larger vortex generator configuration III had distortion levels somewhat less than did the other two configurations.

Thus in terms of overall diffuser performance, all three vortex generator configurations were successful in increasing performance. The increase in diffuser performance was most noticeable in terms of static pressure coefficient although slight increases in total pressure recovery and decreases in distortion were also observed.

The surface static pressure distributions for a range of inlet Mach numbers are presented in Figures 50 to 52 for the three configurations. The tip surface distributions show qualitatively the same trends as did the no vortex generator configuration distributions. However, the hub surface distributions no longer indicated a pressure plateau starting about 7 inches downstream of the inlet station. Rather it can be seen that the hub static pressures either continually

rose to the exit station or leveled off about 8 inches downstream of the inlet station. These distributions indicate that the vortex generator configurations were able to effect sufficient mixing to allow the hub surface boundary layer to proceed further against the imposed adverse static pressure gradient.

The hub surface static pressure taps were located midway between a converging pair of vortex generators. Since the induced vortical motion was away from the surface behind converging pairs of generators, the boundary layer in this region would be expected to be more retarded than the boundary layer behind diverging pairs since in this region the vortical motion was toward the surface.

Also it is apparent that the inclusion of vortex generators on the hub surface did not result in tip boundary layer separation. It is an acknowledged fact that the inclusion of vortex generators on one surface of an annular diffuser can induce boundary layer separation from the other surface. However, the tip surface static pressure distributions failed to reveal any such separation had occurred.

Since vortex generators introduce a marked asymmetry to the diffuser flow field, it is instructive to examine the circumferential variation in the appropriate diffuser exit quantitatives as a function of inlet Mach number. Figures 53 to 55 present the circumferential variation in total pressure recovery for the three configurations for three selected inlet Mach numbers, while Figures 56 to 58 present the circumferential variation in total pressure distortion for the same inlet Mach numbers.

The figures indicate that circumferential variations in recovery became more pronounced as the diffuser inlet Mach number was increased. However, no such circumferential variation in distortion could be noted.

For the total pressure recovery variation, the differences were as much as 2 to 3 percent for the highest inlet Mach number. As the inlet Mach number was increased, the strength of the vortices shed from the vortex generators was increased since the effective velocity past the generators was increased. The stronger vortices increased the mixing (especially behind the diverging pairs of vortex generators) which allowed the boundary layer to proceed further against the imposed adverse pressure gradient. The circumferential variation in recovery indicates that a complete circumferential mixing of the hub boundary layer was not accomplished at the diffuser exit plane.

Another parameter commonly used to assess steady state diffuser performance is the diffuser loss coefficient. As defined in reference 37, the diffuser loss coefficient is the difference between the average inlet and exit station total pressures divided by the average inlet dynamic pressure and is a measure of inefficient diffusion occurring in the diffuser. That is, it represents the integrated loss of available energy due to viscous effects.

Figures 59 to 61 show the circumferential variation of loss coefficient for the three vortex generator configurations for the three selected inlet Mach numbers. The figures indicate a large amount of scatter existed in the data but the general trends were as anticipated. That is the loss coefficient levels were the smallest behind diverging pairs of vortex generators where the mixing action of the vortices was favorable. This corresponds to the location where the total pressure recovery levels were the highest (Figs. 53 to 55). In addition, for all the inlet Mach numbers, the figures indicate the vortex forced mixing reduced the loss coefficient level below the appropriate level for the no vortex generator configuration when the measurements were made behind diverging pairs of vortex generators. The levels were higher than the no vortex generator levels when the measurements were made behind converging pairs of generators.

The circumferential variations in total pressure recovery and exit loss coefficient point out the asymmetric characteristics of the diffuser flow field behind the pairs of vortex generators. The net induced vortical motion sweeps the high energy free stream fluid towards the wall and energizes the boundary layer behind diverging pairs of vortex generators. This results in a higher energy, lower loss region of fluid. Behind converging pairs the low energy boundary layer is swept out into the free stream resulting in a lower energy, higher loss fluid region.

In order to present the measured total pressure rake profile data in some concise format, a contour plot presentation was adopted. It will be recalled that 25 profiles were measured behind two consecutive pairs of vortex generators at each of four measurement planes (stations B, C, D, and E) to definitely map out the pressure fields.

Figures 62 to 64 present the velocity contours measured for configuration I vortex generators installed for the three selected diffuser inlet Mach numbers. It should be noted that for comparison, the appropriate velocity levels for the no vortex generator configuration are also shown on the right side of each figure. These were determined from Figure 37.

Qualitatively the contours for each station looked the same regardless of the inlet Mach number. The general positions of the vortices can be seen at each station including station E. This indicates the vortices still existed at the diffuser exit plane and thus had not burst.

The mixing action of the vortices is clearly evident from the contours when they are compared to the appropriate no vortex generator configuration velocity levels. Behind the diverging pairs of vortex generators the boundary layer thickness was significantly reduced at stations B, C, and D. However, behind converging pairs of generators, the boundary layer thickness was significantly increased.

The contours show that, as already discussed, the mixing action of the vortices had not smoothed out circumferentially at the diffuser exit station. That is there still appeared to remain distinct regions of improved boundary layer (behind diverging pairs of vortex generators) and of retarded boundary layer (behind converging pairs of vortex generators).

The station E contours also show that the hub boundary layer was still separated at the diffuser exit station for all three inlet Mach numbers. However, the separated zone height was reduced by about 50 percent which indicates the vortices were able to cause sufficient forced mixing to allow the hub boundary layer to proceed further prior to separation.

The existence of the hub surface slope discontinuity at the diffuser exit plane would always result in hub boundary layer separation to effectively smooth out the contour. This separation would occur regardless of the presence of vortex generators. An actual flight diffuser design would not have such a surface discontinuity.

A comparison of the contours with those of Figure 5 show qualitatively the same characteristics. Initially, the shed vortices were well defined (stations B and C) but become progressively diffused due to viscous dissipation as they were convected downstream (station D and E). Although it is somewhat difficult to tell from the contour plots it appears the vortices remained approximately the same distance from the hub at stations B and C but had moved away from the hub surface at station D.

Measurement station B was about 12 blade heights downstream of the generator midchord station (for both configurations I and II). The contours indicate that the trailing vorticity had wrapped up into a single vortex prior to that station (station B). Recall it was already pointed out that the shed vorticity behind a vortex generator rolls up into (ideally) a vortex in the first 1 to 2 blade heights downstream.

Figures 65 and 66 present similar rake velocity contours with configurations II and III installed. The average inlet Mach number in each case was 0.29. A comparison of the appropriate contours for the other inlet Mach numbers showed no significant differences from the characteristics exhibited by the contours for $\bar{M}_{inlet} = 0.29$ so they will not be presented.

Two differences should be pointed out when Figure 62 is compared with Figures 65 and 66. For configuration II, the spacing between two adjacent converging vortex generators was increased over that for configurations I and III. Also for configuration III, the vortices were further away from the surface by virtue of the fact that the generator height was 1.5 times greater than that for configurations I and II.

Similar conclusions can be drawn when Figures 65 and 66 are examined as were already discussed in conjunction with Figure 62. For both configurations II and III, the vortices were initially well defined but were markedly diffused toward the diffuser exit station. The vortices did not appear to move away from the hub surface until about station D. The hub boundary layer was still separated at the diffuser exit station with either configuration II or III vortex generators present, but again the height of the separated zone was reduced by about one-half over that for no vortex generator configuration.

A comparison of the contours of Figure 66 with those of Figures 62 and 65 also show the effect of vortex strength and position on the hub boundary layer. Even though the vortices of configuration III were positioned about 1.5 times further from the hub surface than were the vortices of configurations I and II, the increased vortex strength was able to carry the de-energized boundary layer fluid particles a further distance away from the surface. This becomes even more apparent as the flow proceeded downstream. A comparison of contours for stations C and D show that configuration III vortices carried the low energy fluid particles a significantly further distance such that a larger percentage of the circumferential span of hub boundary layer was thin and apparently unretarded.

Such comparisons point out the important fact that if vortex strength is not sufficient, the vortical motion will not be able to carry the retarded fluid particles far enough away from the surface and the retarded fluid can then be swept back into the boundary layer region which will destroy the favorable forced mixing action. This problem becomes especially critical when adjacent vortex generators are spaced very closely.

The contours for configurations I and II do show that the vortices did have sufficient strength to carry away the retarded fluid.

The contour plots for configuration III show that the core size of the vortices shed were significantly larger than those shed for configurations I and II. This is to be expected since the circulation about each vortex generator is approximately proportional to the chord and the chord of configurations III was 1.5 times that of configurations I and II. Thus, it would follow that the vortex core size would be larger.

An examination of the various contours reveal the existence and approximate locations of the vortices. However, in an attempt to determine more accurately the vortex locations at each station for each of the three configurations, the individual total pressure rake profiles were examined. The results are shown in Figures 67 ad 68.

Figure 67 shows the circumferential position of the two vortices making up a vortex pair while Figure 68 shows the height of the vortex axes above the hub surface.

The vortex positions were determined only corresponding to $\overline{M}_{inlet} = 0.3$ since the contour plots showed little variation with inlet Mach number. For reference, Figure 68 also shows the appropriate hub surface boundary layer displacement thickness variation.

While there is some scatter in the results, the vortex paths show the expected results. After forming, the vortices move toward each other in the region behind the converging pairs of generators. The amount of movement is greatest for configuration II (the unevenly spaced configuration) which is in agreement with Gould's predicted trends shown in Figure 7.

Figure 68 shows that the vortices did remain at an approximately constant distance from the hub surface until the vicinity of station D where they began to move away from the surface at an increasing rate. As already discussed, the movement away from the surface coincides with the adjacent vortices exerting an induced velocity away from the surface. The movement away from the surface decreases the mixing effectiveness of the vortices and could partially explain the limiting performance levels attained.

Figure 68 also indicates that the vortices were initially approximately 0.2 inch from the hub surface for configurations I and II and 0.3 inch for configuration III. The respective ratios of vortex axis height-to-vortex generator span were 0.8 and 0.86 which are in agreement with Taylor's value of 0.9.

The vortex path characteristics did not appear to change with vortex generator height (and, hence, vortex strength) other than the vortices were initially positioned further away from the hub surface. However, it must be pointed out that the vortex positions can only be considered to be approximate due to the coarseness of the measurements.

It is interesting to note that the vortex paths of the three configurations exhibited some different trends than those predicted by potential flow path prediction techniques such as Gould's.[26] In particular, Figure 5 shows that evenly spaced vortex generator configurations (D/d = 2) should be relatively poor mixers because they almost immediately lift off the surface. However, the experimentally determined axial paths did not appear to change with vortex generator spacing. Rather, the vortices for the two evenly spaced configurations (I and III) did indeed remain close to the surface as did the vortices for the unevenly spaced configuration. This discrepancy between analytical path prediction and actual vortex path further points out the inadequacy in using potential flow analysis to in essence design vortex generators for actual diffuser

applications. Many diffuser applications can be found in the literature which have successfully employed evenly spaced vortex generator configurations to improve performance. Indeed, the performance of the dM/dz diffuser discussed herein was not adversely affected by the use of the two evenly spaced vortex generator configurations.

In order to determine the strength and size characteristics of the shed vortices, the angularity profiles were examined. Figure 69 shows the profiles measured at stations B and C for configuration I vortex generators for an inlet Mach number of 0.3. Profiles for the other configurations were similar in general trends so they will not be presented.

The profiles show the mixing action at stations B and C was localized near the vortex location as the flow angularity levels behind diverging pairs deviated from zero only in the vicinity of the vortices. However, a distinct yaw component of as much as 10^{o} to 15^{o} at station B and 10^{o} at station C was measured behind the converging pairs. For convenience, the profiles through the estimated vortex centers are noted on Figure 69.

The yaw angle also approached zero about 1 inch away from the hub surface for configurations I and II. However, as might be expected, the yaw angle for configuration III was still nonzero at the 1 inch location.

The vortex core sizes were estimated by taking the distance between the maximum positive and negative yaw angles for the profiles which were judged to be those through the vortex center. Such estimations were made from the profiles measured at stations B and C for all three configurations and the results are shown in Figure 70.

The data shows some scatter which is to be expected since the angularity measurements were coarsely spaced outside the boundary layer, but the approximate core size can be seen to be about 0.2 of the vortex generator chord for both stations B and C.

This core size agrees qualitatively with the sizes of shed vortices measured by several investigators and discussed by Mitchell.[38] These vortices were generated by wings installed in low speed wind tunnels and thus essentially represent vortices shed from wings immersed in a inviscid flow field ($h/\delta >> 1$). Thus, it appears that the fact that for the present test the vortex generators were essentially immersed in a viscous flow field ($h/\delta \approx 1 - 2$) did not measurably affect the vortex size.

The results shown in Figure 70 also indicate that the shed vortices did not appear to grow measurably in size between stations B and C. This was especially true for configuration III where the vortices were positioned further away from the surface and, hence, further away from the viscous boundary layer ($h/\delta = 1.79$).

Following the technique discussed by Dosanjh, Gasparek, and Eskenazi,[27] the strength distributions of the shed vortices were calculated from the angularity profiles measured through the estimated vortex centers.

Briefly, the local vortex strength was related to the local flow angularity, local velocity, and distance from the estimated vortex center by

$$\frac{\Gamma\Gamma}{2\pi\ell U_{max}} = \tan\beta \frac{U}{U_{max}} \cdot \frac{R - R_{center}}{\ell} \qquad (12)$$

Figures 71 and 72 present the vortex strength distributions for the three configurations for stations B and C, respectively. Note that profiles are shown for two vortices for each configuration for each station.

The profiles show a fair amount of scatter which is especially noticeable for the few measurements made above the vortex. Part of the scatter can be attributed to a difficulty in determining the vortex center position from the few measurements made outside the boundary layer.

Comparison of the levels of circulation in the boundary layer between stations B and C for each configuration indicates that the vortex strength through the boundary layer had decreased due to viscous dissipation. The local circulation was nondimensionalized by the local free stream velocity at each station. However, since little diffusion occurred between stations B and C, the two velocities were essentially equal ($U_{max_B} / U_{max_C} = 1.03$) and thus the profiles can be compared directly.

In order to correlate the reduction in vortex strength due to viscous dissipation, the maximum value of circulation measured in the boundary layer for each configuration for each station was determined and ratioed to an estimated initial vortex strength calculated using Gould's technique already discussed. For this calculation the factor B was taken to be equal to 1.0, δ^* was taken to be 0.002 inch, and C_L was determined using $2\pi\alpha$. The results are shown in Figure 73. Again note that two values exist for each configuration at each station. A fair amount of scatter exists in the data which is expected but again trends can be determined.

The data was also fitted using a least squares technique to a curve of the form $\Gamma/\Gamma_0 = (1 - e^{[-(U\cdot\text{constant})/(Z-Z_{VC})]})$ which is also shown. This curve is of the same general form as that suggested by Nishi and Senoo[17] but with a different constant. The constant determined by Nishi and Senoo was $2 \cdot 10^{-2}$ seconds while the curve fit of the data discussed herein yielded a value of $8 \cdot 10^{-4}$ seconds.

The two values of the constant do not agree which might be expected since the two experiments involved different diffuser configurations tested at different conditions. This constant can be viewed as a decay time constant which describes the rate at which viscosity acts to dissipate the vortex strength.

As Figure 73 indicates, the vortex strength had dissipated only to about 90 percent of its initial strength upon reaching station B, but viscosity effects then became much more significant as the vortex strength was reduced to about 60 percent of its initial strength at station C. Thus, the mixing action of the vortices had become significantly reduced downstream of station B due to the action of viscosity.

It is interesting to note that the effects of viscosity appeared to be similar for all the vortex generator configurations. This is especially surprising since the vortices of configuration III were positioned further away from the surface than were those for configurations I and II.

It might be speculated that if a vortex generator configuration would have been tested which had maintained a larger portion of its initial vortex strength for a longer axial run, the performance of the dM/dz diffuser tested would have been improved. With the vortex generator configurations tested, the correlation of the vortex strength dissipation indicates that the vortices would only have about 45 percent of their initial strengths at station D and thus the forced mixing would be expected to be severely limited.

Figures 74 through 76 present the circumferential variation of the boundary layer integral properties measured at stations B, C, and D for configuration I vortex generators installed for average inlet Mach numbers of 0.29, 0.48, and 0.75. The effects of the forced mixing on the hub boundary layer can be seen at all stations. For reference, the appropriate values for the no vortex generator case are also shown. Although the absolute levels of the various quantities vary with inlet Mach number as would be expected, the qualitative trends appear to be the same and, thus the data corresponding to $M_{inlet} = 0.3$ for all three configurations will be discussed.

As Figure 74(a) shows, the mixing action was clearly evident at station B. Behind the diverging pairs of vortex generators, the inward vortical motion of high energy air reduced the boundary layer displacement and momentum thicknesses to about 75 percent of their respective no vortex generator levels. However, behind the converging pairs of generators the outward vortical motion of the low energy boundary layer fluid resulted in integral thicknesses about twice their respective no vortex generator levels.

Surprisingly, the shape factor distribution shows higher values behind the diverging pairs of generators. Behind the converging pairs of generators, the shape factor was roughly equivalent to the no vortex generator level. These results are surprising because it would be expected that the favorable mixing behind diverging pairs of generators would reduce the shape factor. The marked variance in integral thicknesses shown clearly indicates that the mixing action was present so the variation in shape factor cannot be explained. At the higher inlet Mach numbers it will be noted that this trend was not present and the shape factor was indeed reduced behind divergent pairs of generators.

The circumferential variations in integral properties at station C (Fig. 74(b) indicate the mixing action became more pronounced as the integral thicknesses were reduced to as little as one third or one fourth of their respective no vortex generator levels. Behind the converging pairs of generators, the thicknesses became even higher with peak values of about twice those measured at station B.

The variation in shape factor shows some marked differences when compared to that at station B. The shape factor was measurably reduced in two regions below the no vortex generator level. A comparison of this figure with the axial vortex paths of Figure 67(a) shows that these correspond with the locations of the two vortex centers. Thus, the forced mixing can be seen to have reduced the shape factor (and, thus, increased the boundary layer health) in the immediate vicinity of the vortex center. Again, it is interesting to note that regions of boundary layer flow which had the lowest values of integral thicknesses did not have the lowest shape factors.

Thus, at station C, the mixing action was still localized. That is, only certain regions of the hub boundary layer had felt the favorable effects of forced mixing.

However, the variations measured at station D and shown in Figure 74(c) clearly show that the mixing action had spread circumferentially by that station to favorably affect about all the boundary layer flow. The integral thicknesses measured behind convergent generators were only slightly higher than the no vortex generator levels while the levels behind divergent generators were reduced by about two thirds.

Also the circumferential variation in shape factor shows much less variation than that measured at stations B and C and the level was everywhere less than the no vortex generator levels.

No profiles are shown for station E since it has already been shown that the boundary layer was separated at the diffuser exit plane.

Figures 77 and 78 present the variations of the integral properties for configurations II and III for a nominal inlet Mach number of 0.3.

The variations measured at station B for configuration II (Fig. 77(a)) show an effect of spacing the converging vortex generators further apart. Two distinct peaks in the integral thicknesses occurred which coincide with the boundary layer fluid being expelled into the free stream. However, between these two peaks, the thicknesses tended to return to the no vortex generator levels which is to be expected. Thus, at station B, the low energy boundary layer fluid expelled by the vortices had not yet mixed into one low energy pocket as it had for configuration I.

The reductions in integral thicknesses were about the same magnitude as were those for configuration I which might be expected since the vortices were of the same strength.

The shape factor variation at station B shows the same trends as it did for configuration I.

At station C (Fig. 77(b)), the two distinct peaks in the integral thicknesses disappeared which indicates that the two distinct low energy pockets of fluid had become mixed. However, the maxima in integral thicknesses were considerably less than those for configuration I (Fig. 74(b)). The minima in integral thicknesses are comparable with those of configuration I.

Again, the shape factor distribution shows the mixing action remained localized in the vicinity of the vortex center.

At station D, the favorable mixing action appeared to have been felt over a significant portion of the circumferential extent; however, the integral thicknesses show regions with levels considerably higher than those of the no vortex generator configuration, and thus, is reflected in corresponding shape factor levels being higher than the no vortex generator level.

Thus, a comparison with the corresponding profiles of configuration I (Fig. 74(c)) would indicate that the configuration II vortex generators did not have as favorable mixing characteristics over the aft end of the diffuser as did configuration I.

As expected, the variations for configuration III vortex generators showed some differences in level when compared with the results of the other two configurations. This is expected since the strength of the shed vortices are greater due to the larger airfoil semi-span and chord.

At station B (Fig. 78(a)) the integral thicknesses exhibited peaks measurably higher than those for the other configurations. This

can be attributed to increasing the vortex strength and size resulting in more lower energy boundary layer fluid being swept further out into the free stream. However, the minima in integral thicknesses were coincident with those for configurations I and II. The peaks were much sharpter and narrower than those for the other configurations.

At station C (Fig. 78(b)), the peaks in integral thicknesses were again sharper than those for the other configurations but the peaks were no higher. The shape factor distribution indicates the mixing action had spread circumferentially over a greater extent than it had for the other configurations as evidenced by the longer circumferential extent of reduced values below the no vortex generator level. No local increase in shape factor could be noted behind the converging generators.

The station D thickness profiles (Fig. 78(c)) exhibited the increased mixing levels as the thicknesses were reduced below the no vortex generator levels throughout the circumferential extent. This compares with the corresponding profiles of the other two configurations which had local values greater than the no vortex generator level. Likewise, the shape factor distribution was markedly below the no vortex generator level over approximately the whole circumferential extent.

As indicated previously, the skin friction distributions were determined at stations B, C, and D using a Clauser plot analysis technique discussed in Appendix D. As already mentioned, Spangler and Wells[24] showed that boundary layer profiles measured downstream of generators placed in a pipe flow did follow the law of the wall variation. Figures 79 through 81 present the circumferential variations in skin friction coefficient for the three configurations tested.

The station B profiles (Figs. 79(a), 80(a), and 81(a) show the effect of the mixing action in increasing the skin friction coefficient behind converging pairs relative to the no vortex generator level. Peaks in coefficient level occurred for configurations II and III at positions coincident with the determined vortex centers but no such peaks were noted for configuration I.

A fair amount of scatter in the distribution behind the convergent pair was noted for configuration III (Fig. 81(a)). It is not clear why this occurred although it is possible it could be attributed to the increased outward flux of boundary layer fluid resulting in a significant deviation from the law of the wall variation.

The station C profiles (Figs. 79(b), 80(b), and 81(b)) exhibited peaks for configuration I and II only. The plateau exhibited by configuration III is indicative of the increased circumferential extent of forced mixing as already discussed.

A comparison of the three profiles shows the increased mixing levels achieved by configuration III reflected in the minima of skin friction coefficient compared to the no vortex generator level. For configuration III, the two levels are roughly coincident while the other two configurations have minima below the no vortex generator level.

The station D profiles (Figs. 79(c), 80(c), and 81(c) indicate that configurations I and III had effected an essentially complete spanwise mixing while configuration II still had a more localized mixing effect. This result for configuration II might be anticipated since the distance between diverging pairs of generators was reduced and it is the portion of the boundary layer flow behind diverging generators which receives the favorable flux of high energy fluid. Thus, this smaller region of fluid would receive a more concentrated mixing effect into the boundary layer. A comparison of the peak levels in skin friction coefficient level attained shows that configuration II had a level about 1.5 times those for the other configurations.

However, configuration II also showed a fair circumferential extent of boundary layer flow which had a skin friction level essentially identical to that for the no vortex generator case.

Comparison of the skin friction coefficient variations for configurations I and III shows that configuration I had a larger extent of higher skin friction coefficient that did configuration III. This is opposite to what one might expect and the reason for this occurrence is not understood.

The circumferential variations in skin friction coefficient shown here agree qualitatively with the results of Spangler and Wells.[24] The variations in wall shear stress shown herein are more pronounced but that is to be expected since the freestream velocity was much higher ($\approx$ 300 ft/sec) than it was for the study of Spangler and Wells ($\approx$ 50 ft/sec).

It is instructive to examine the average boundary layer quantities at each station to determine if on the whole the forced mixing has favorably affected the boundary layer. Figures 82 and 83 present the average integral thicknesses (δ^* and θ) and skin friction coefficient C_f variations for the three configurations tested. In each case, the variables were nondimensionalized by the appropriate value for the no vortex generator configuration. The average values were simply an average of the circumferential variations already shown.

The displacement thickness variations were similar for configurations I and III with the level being reduced to about 60 percent of the no vortex generator level at station D. At station B, the levels were about 20 percent higher for all configurations tested

than for the no vortex generator level. This increase is indicative of the blockage effects of the individual vortex generators. Configuration II had somewhat higher levels of displacement thickness which is indicative of the more localized mixing effect which has already been noted.

The reductions in momentum thickness were not as great as the reductions in displacement thickness. The levels of momentum thickness at stations B and C were greater for configuration III than those for the other two configurations. This indicates the increased losses occurring due to the drag of the individual vortex generators.

Configuration II shows the least variation in momentum thickness which again could be indicative of the more localized mixing.

All configurations show a reduction in momentum thickness at station D relative to the no vortex generator level.

The variations in average skin friction coefficient (Fig. 83) shows similar trends for all configurations. The average skin friction coefficient levels were as much as 3 to 4 times the no vortex generator level.

Thus, on a basis of the average quantities, it can be said that all three configurations improved the health of the hub surface boundary layer relative to its state with no vortex generators present.

Figures 84 to 86 present the hub surface boundary layer velocity and axial turbulence intensity contours for the three vortex generator configurations tested. For comparison the appropriate no vortex generator levels are shown on the right side of each figure.

The velocity contours provide the same information as did the circumferential variations of integral parameters already discussed (Figs. 74 to 78). The station B contours for configurations I and III (Figs. 84(a) and 86(a)) indicate the forced mixing was felt across a significant portion of the circumferential span while for configuration II, the effect was still more localized. The contours for configuration III when compared to those for configuration I indicate that the increased strength of the shed vortices had more of a favorable effect on the forced mixing than did the further positioning of the vortices away from the hub surface have an unfavorable effect. This can be seen when the distances from the hub surface of comparable velocity contours are compared for the two configurations.

The increased spacing behind the converging pairs of vortex generators for configuration II resulted in the low energy fluid being confined to only a portion of the circumferential span. The contours

indicate that in the region approximately midway between the converging pairs, the boundary layer profile was essentially the same as the no vortex generator profile.

The axial intensity contours for station B indicate that forced mixing appreciably changed the turbulence characteristics of the hub boundary layer. The intensity level near the hub surface was as much as 8 to 9 percent for the three configurations. The highest levels of turbulence in the near wall region occurred at circumferential positions which were essentially beneath the estimated vortex axes locations (Fig. 67). The approximate locations of the vortices are also evident from the increased levels of turbulence present as compared to the no vortex generator free stream level of 2 to 3 percent.

As might be expected, the character of the turbulence intensity profiles was much different when measured at various positions behind the vortex generators. The reduction of the boundary layer thickness behind diverging pairs of vortex generators resulted in correspondingly compated intensity profiles although the maximum in level compared with the no vortex generator maximum in level. The outward flux of low energy fluid behind the converging pairs resulted in appreciably thicker, more retarded velocity profiles and corresponding turbulence intensity profiles which had significant regions of almost constant turbulence level.

The station C velocity contours (Figs. 84(b) to 86(b)) show the same general features as did the station B contours. The contours indicate a better definition of the vortices than did those for station B. The contours for configuration II indicate the mixing effect had spread across a larger portion of the circumferential span for that configuration. That is the outward displacement of low energy fluid occurred across the whole circumferential span behind converging pairs of vortex generators.

The station C axial intensity contours for all these configurations indicate that the near wall region of maximum turbulence intensity which had occurred beneath the vortex axes for station B had grown in size and had been swept into the region behind the converging pairs and away from the hub surface. The movement of these high turbulence intensity zones was in the same direction as the induced vortical motion present. Again the approximate locations of the vortices could be determined from the increased turbulence intensity levels present in the core region of the vortices.

A comparison of the mean velocity profiles for station D (Figs. 84(c) to 86(c)) indicate that only for configuration III had the favorable effect of forced mixing spread circumferentially across the complete span behind two pairs of vortex generators. For the other two configurations, regions of boundary layer flow still existed which had velocity contours displaced further from the hub surface than were the corresponding no vortex generator contours.

The axial turbulence contours for station D indicate a further growth in the size of the high intensity fluid region near the hub surface. For all three configurations significant regions of flow behind converging pairs of vortex generators had turbulence intensities larger than the maximum measured level for no vortex generators present. Behind converging pairs of vortex generators the maximum in turbulence intensity level approximately agreed with the no vortex generator maximum level.

The turbulence contours also indicate that only for configuration III could the approximate vortex positions be determined from the increased free stream turbulence levels. The vortices for configurations I and II were apparently more diffused at station D than were the vortices for configuration III.

Figures 87 to 89 present selected boundary layer profiles measured at stations B, C, and D for configuration I. Profiles are presented of mean velocity (U/U_{max}), axial turbulence intensity ($\sqrt{\overline{u'^2}}/U_o$ and Reynolds shear stress($-\overline{u'v'}/U_o^2$). The five circumferential positions chosen for each station for presentation of data were (1) the reference position (0^o), (2) the position judged to be coincident with the local vortex axis, (3-4) the two positions immediately adjacent to the vortex axis position, and (5) the circumferential position corresponding to 11.25^o (for reference, see Fig. 31). Note that the profiles in the immediate vicinity of the vortex are shown for only one of the two vortices which form a vortex pair. These profiles were felt to be representative of the variation in boundary layer properties which existed behind two consecutive pairs of vortex generators.

Similar profiles will not be presented for configurations II and III as the observed trends were similar although absolute levels varied as would be expected.

The profiles measured at the 0^o circumferential position for stations B and C indicate the boundary layer properties midway between diverging pairs of vortex generators. This location corresponds to a position of favorable forced mixing since the inward induced motion of both vortices making up the pair should be felt. A comparison of Figures 87(a) and 88(a) indicate the increasingly favorable effect of the forced mixing as the hub boundary layer proceeded downstream. The mean velocity profile at station C indicated a significantly healthier profile in comparison to the appropriate no vortex generator profile than did the station B profile. In particular, the velocity levels near the hub surface were increased at station C while they remained essentially unchanged at station B.

The axial intensity profiles for the two stations both had the same trends as did the appropriate no vortex generator profiles although in each instance the effective reduction in the boundary layer thickness due to the favorable effects of forced mixing resulted in a compressed profile.

The Reynolds shear stress levels for each station were also reduced relative to the no vortex generator levels. The accuracy of these shear stress measurements can be questioned since for measurements made behind diverging pairs of vortex generators, the cross film probe was of significant size with respect to the local boundary layer thickness. Thus the sensors were possibly measuring an average of the fluctuating velocity components taken over a significant portion of the boundary layer thickness rather than the desired local values.

The profiles measured in the immediate vicinity of the vortex (Figs. 87(b), (c), and (d) and 88(b), (c), and (d)) showed some significantly different characteristics depending on the direction of the induced motion. The mean velocity profiles for both stations showed a healthier profile for the favorable mixing position (Figs. 87(b) and 88(b)) with the effects being more pronounced at station C. The profiles measured coincident with the vortex axis location (Figs. 87(c) and 88(c)) differed between the two stations. The station B profile was somewhat retarded in the near wall region while the station C profile was significantly more developed. The profiles measured in the unfavorable mixing position (Figs. 87(d) and 88(d)) also differed between the two stations. The station B profile was more retarded while the station C profile was more developed in the inner region of the boundary layer.

The approximate position of the vortex core could be more easily deduced from the station C profiles than it could be from the station B profiles. The reductions in mean velocity were more distinct at station C.

The axial turbulence intensity profiles also differed depending on the measurement position relative to the vortex axis. For the favorable mixing positions (Figs. 87(b) and (c) and 88(b) and (c)) the intensity profiles had two distinct components - one associated with the boundary layer and a second associated with the vortex. In the unfavorable mixing position (Fig. 87(d) and 88(d)) no such distinction could be made. Rather as the profiles indicate, a significant region of increased turbulence intensity existed in the outer regions of the boundary layer which corresponded to the low energy fluid which was swept away from the inner region of the hub boundary layer. Again the effect was more pronounced at station C.

The shear stress profiles in the immediate vicinity of the vortex generally had levels which were less than the appropriate no vortex generator levels. In addition a sizeable component of shear stress existed in the core region of the vortex. Several of the profiles (Figs. 87(b), 87(d), and 88(d)) showed regions of large negative shear ($-\overline{u'v'}/U_o^2 < 0$) while the remaining profiles exhibited large positive values of shear stress. The reason for the large negative shear component is not known. Similar regions of negative shear stress were noted for the other vortex generator configurations.

The profiles corresponding to a circumferential position of 11.25° (Figs. 87(e) and 88(e)) represent measurements made midway between a converging pair of vortex generators. This is an unfavorable forced mixing region since the induced motion was away from the surface. The mean velocity profiles for both stations substantiate this as they were both significantly retarded relative to the appropriate no vortex generator profile.

The axial turbulence intensity profiles for both stations indicate significant regions of almost constant level. The characteristic boundary layer distribution of turbulence intensity was completely altered.

The Reynolds shear stress profiles for the two stations had somewhat different characteristics. The station B profile was similar to the station B turbulence intensity profile in general characteristics. That is the profile had a region of almost constant shear stress level. The station C shear stress profile showed a large peak approximately 0.3 inch from the hub surface. A similar peak in shear stress level was noted for configuration III.

Comparable station D profiles are shown in Figure 89. It should be recalled that the station D probe was oriented differently with respect to the vortex generators than were probes B and C (see Fig. 31). Profiles measured at a circumferential position of 0° for station D indicate the boundary layer properties which existed midway between two converging vortex generators as opposed to properties which existed midway between two diverging vortex generators for stations B and C.

The five mean velocity profiles presented indicate that a circumferential variation in the mixing effect was still present at station D. The profile measured midway between the converging vortex generators (Fig. 89(a)) shows only a slight improvement in the mid region of the boundary layer. The velocity levels near the hub surface were essentially coincident with the corresponding no vortex generator levels. The velocity levels in the outer region were noticeably less than the no vortex generator level and indicated the existence of the vortex core.

The three velocity profiles measured in the immediate vicinity of the vortex (Figs. 89(b), (c), and (d)) were significantly improved over the no vortex generator profile. The improvement was noticeable across all the boundary layer except for the region of the vortex core where again the velocity levels were reduced relative to the no vortex generator levels.

The velocity profile measured midway between the diverging pair of vortex generators (Fig. 89(e)) indicates the major effect the forced mixing exerted on the hub surface boundary layer. The velocity

profile had a fully developed characteristic with a thickness which appeared to be about one half the value of the thickness of the corresponding no vortex generator profile.

The axial turbulence intensity and Reynolds shear stress profiles both exhibited similar trends. The general shapes of the two curves were similar to the no vortex generator curves although the favorable effects of the forced mixing which essentially reduced the thickness and improved the health of the boundary layer resulted in the peaks occurring closer to the hub surface. As would be expected, the peaks occurred closest to the surface for the measurements made midway between diverging pairs of vortex generators (Fig. 89(e)). The levels of the peaks in intensity and shear stress for this circumferential position were approximately equal to the respective level for the no vortex generator configuration.

The turbulence intensity profiles for all positions except that midway between the diverging pair indicated increased levels of turbulence in the outer region of the boundary layer. This increased turbulence level is attributable to the existence of the vortex core.

The shear stress profiles presented for stations B and C (Figs. 87 and 88) have indicated that the height of the boundary layer relative to the cross film anemometry probe made the accuracy of the shear stress measurements doubtful. For this reason, eddy viscosity and mixing length profiles will be presented only for station D. For reference the appropriate no vortex generator profiles will also be presented so as to determine the increases in mixing which were achieved.

The nondimensional eddy viscosity distributions are presented in Figure 90 for the three vortex generator configurations. Profiles are shown for the same five circumferential positions for which property profiles were presented for configuration I (Figs. 87 to 89). A degree of scatter exists in the calculated levels of eddy viscosity but the general increases in mixing due to the vortex generators can be determined.

For configurations I (Fig. 90(a)) and II (Fig. 90(b)), the increased mixing levels were confined to a partial circumferential extent as the levels were less than the no vortex generator levels for the profiles measured midway between the converging pair of vortex generators. For configuration III, the eddy viscosity levels were essentially always greater than the no vortex generator levels.

Figure 91 presents the nondimensional mixing length variations for the three configurations for the same profiles. Similar conclusions can be drawn from these profiles regarding the effectiveness of the three vortex generator configurations as forced mixers. That is configurations I and II still had regions of the boundary layer flow for which the favorable effects of the forced mixing had

not been fully felt while for configuration III, the favorable effects had been felt across the complete circumferential span.

The eddy viscosity and mixing length profiles presented indicate that it is not possible to determine a single value of the appropriate constant (i.e., $\varepsilon/\delta^* U_{max}$ or ℓ/δ^*) to replace in the conventional two layer turbulence model to account for the effects of forced mixing on the hub boundary layer. On the average, for all these configurations, the eddy viscosity and mixing lengths were increased by a factor of about 2 to 3 at station D.

This should not be too surprising since the boundary layer profiles presented (Figs. 87 to 89) have indicated a distinct asymmetry persisted in the hub boundary layer characteristics once the vortex generators were installed. An adequate modeling of the forced mixing process should account for the asymmetric characteristics which have been shown as well as the axial variation in forced mixing levels which unfortunately could not be determined from this experiment.

Such a forced mixing model would require a three-dimensional boundary layer computer code which would have a three-dimensional turbulence model incorporated and such codes are presently in the development stage. To incorporate the forced mixing effects in existing two-dimensional code, the best that apparently can be done is to incorporate some function in the turbulence model which describes the axial variation in forced mixing level present. Data such as that shown in Figures 90 and 91 could be used to determine the values of the forced mixing function; however, it will be necessary to make similar measurements at several axial locations. This was attempted in the experiment discussed herein, but the problem of the hot film probe size compared to the boundary layer thickness resulted in the accuracy of the measurements made at stations B and C being in doubt.

A comparison of the forced mixing effectiveness of the three vortex generator configurations made using the eddy viscosity and mixing length distributions indicates that none of the three vortex generator configurations was clearly the superior forced mixing configuration. This conclusion may seem surprising but it is in agreement with the overall diffuser performance levels which were presented and discussed earlier. It will be recalled that it was determined that all three vortex generator configurations provided increases in performance over the no vortex generator configuration. However, little difference could be detected between the increases in performance provided by the three configurations tested.

The detailed boundary layer profile data which has been presented has shown that only configuration III could effect a complete span-wise favorable mixing of the hub surface boundary layer at station D. However, this improvement in forced mixing achieved was apparently not of sufficient importance to significantly affect the overall diffuser performance.

It would appear that additional experimental efforts are required to better understand the forced mixing process. In particular tests of larger scale relative to the measurement probe size would be helpful in understanding the axial variation of the forced mixing process. The use of three-dimensional hot film anemometry probes would also allow the investigation of the remaining components of the Reynolds stress tensor which should be useful in generating truly three-dimensional forced mixing models.

Also, an area of interest in recent turbulence research has been that of coherent structures in the turbulent boundary layer. If proper experimental measurements are made, large scale, long life time eddy structures can be identified in the outer extremes of the turbulent boundary layer. It is thought that these large scale eddies determine the rate at which the turbulent boundary layer grows. That is, the large eddies are responsible for the outer inviscid flow near the edge of the boundary layer being swept into the boundary layer and thus causing the turbulent boundary layer to grow. This mechanism is conceptually similar to the forced mixing phenomenon discussed herein so possibly future experimental studies could make use of these recent turbulence measurement techniques and concepts to even better understand the forced mixing process.

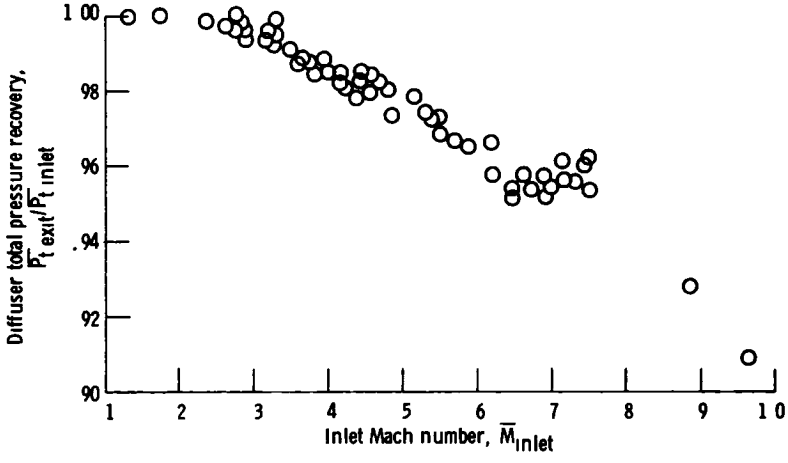

Figure 32. - Diffuser total pressure recovery with no vortex generators installed.

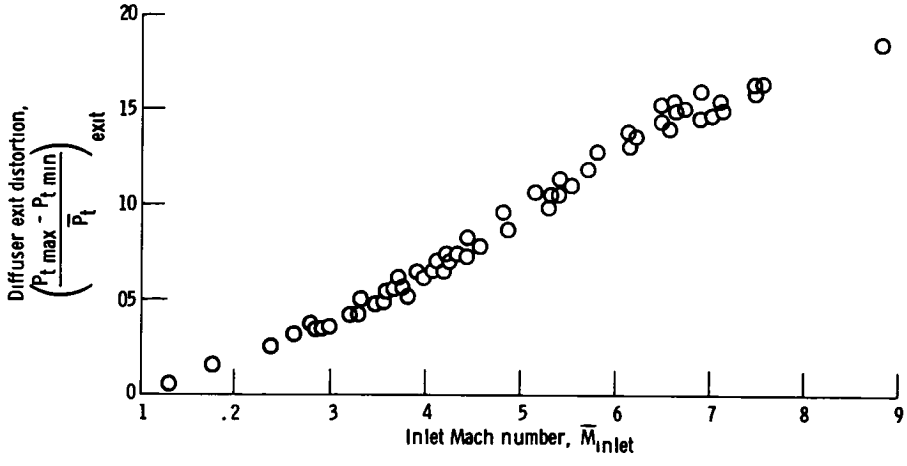

Figure 33 - Diffuser exit total pressure distortion with no vortex generators installed.

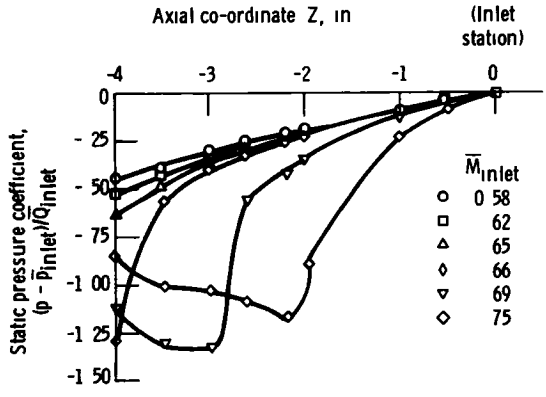

Figure 34 - Tip surface static pressure distributions in diffuser throat region

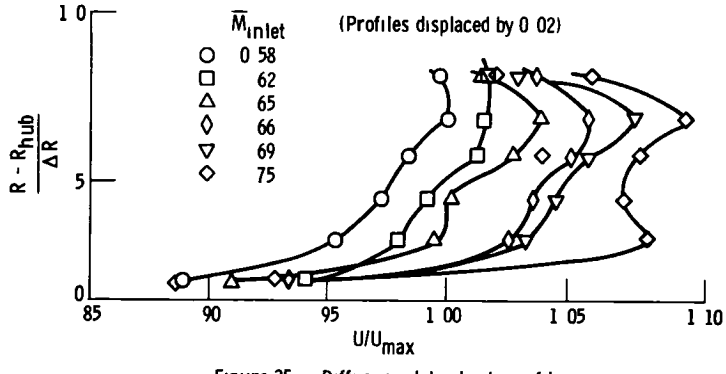

Figure 35 - Diffuser inlet velocity profiles.

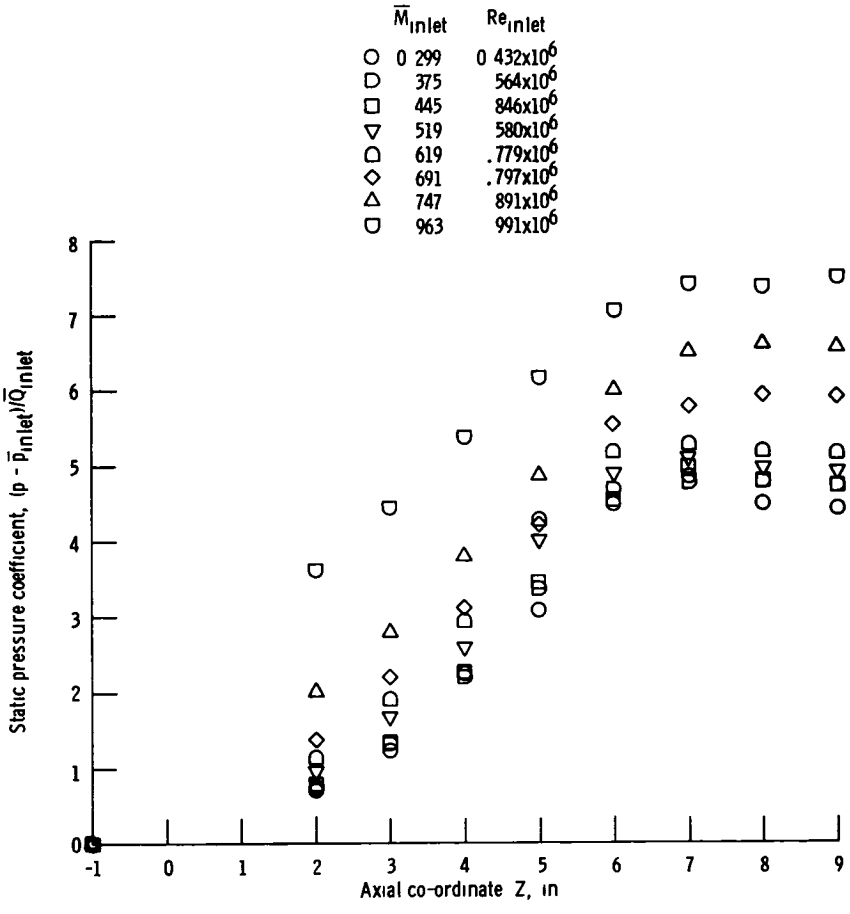

(a) Hub surface

Figure 36 - Surface static pressure coefficient variation with no vortex generators installed

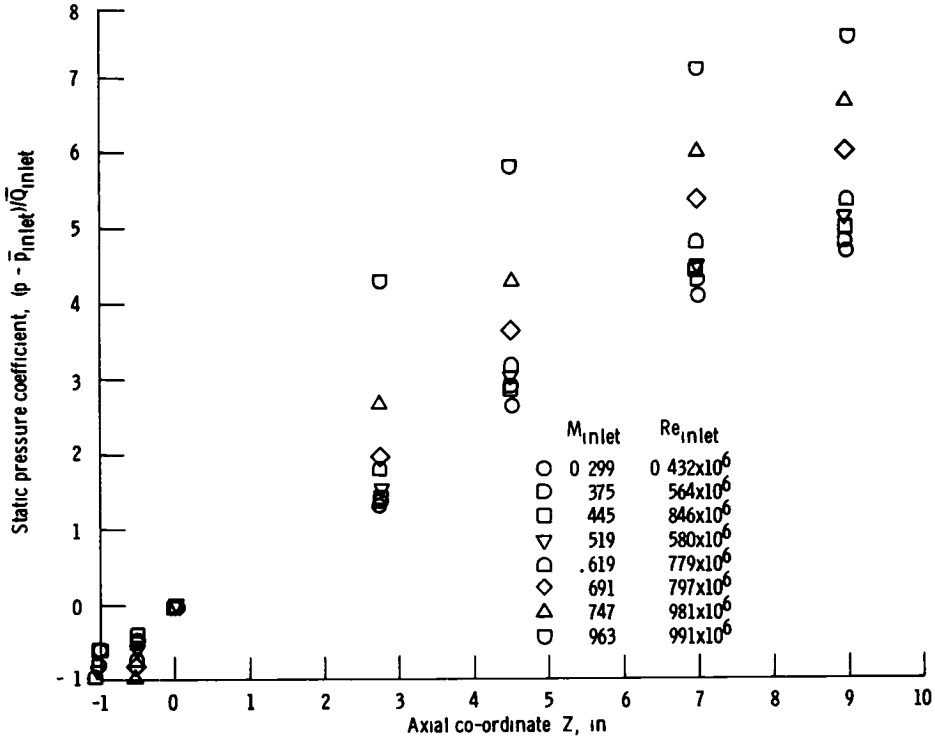

(b) Tip surface

Figure 36 - Concluded.

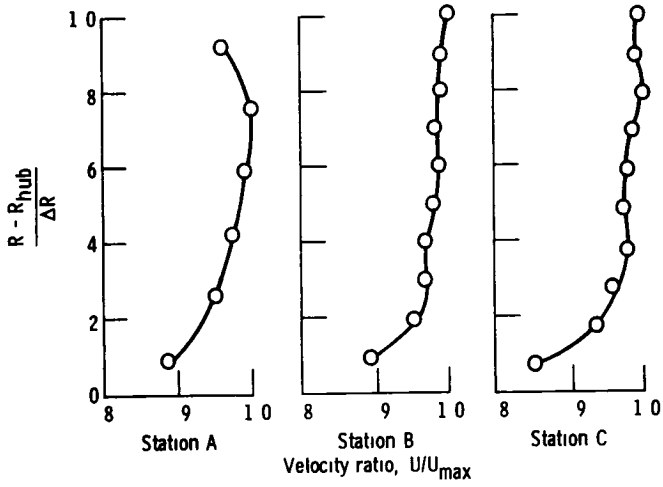

(a) $\overline{M}_{inlet} = 0.29$

Figure 37 - Diffuser velocity profiles with no vortex generators installed.

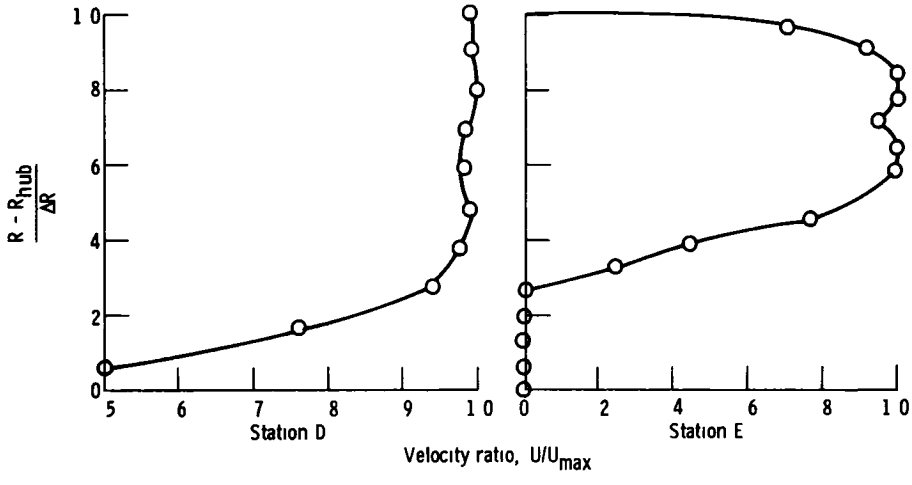

(a) Concluded

Figure 37 - Continued

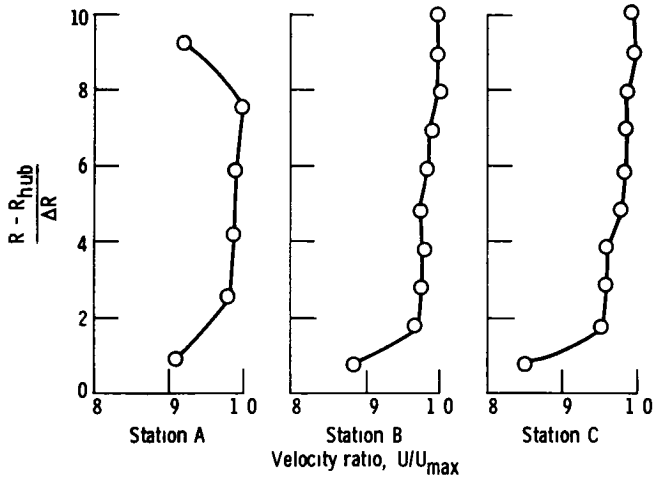

(b) $\overline{M}_{inlet} = 0.48$

Figure 37 - Continued

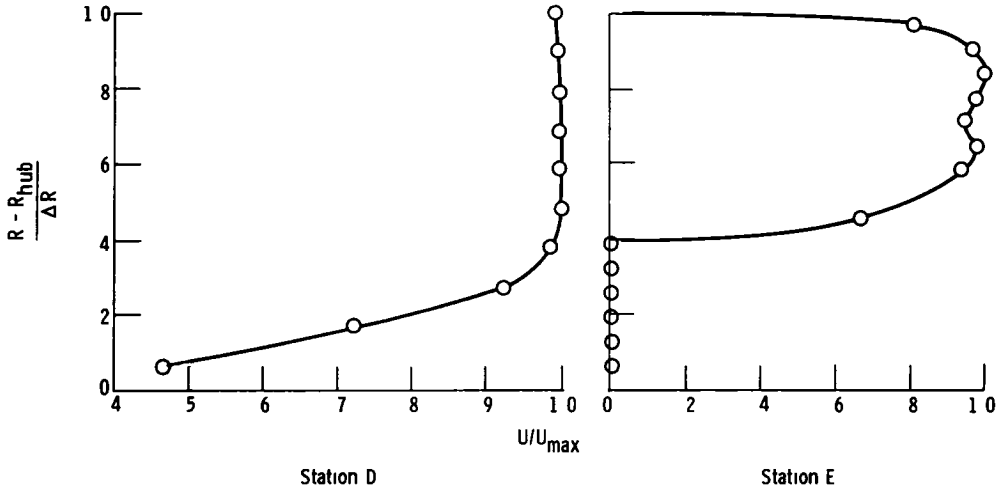

(b) Concluded

Figure 37 - Continued

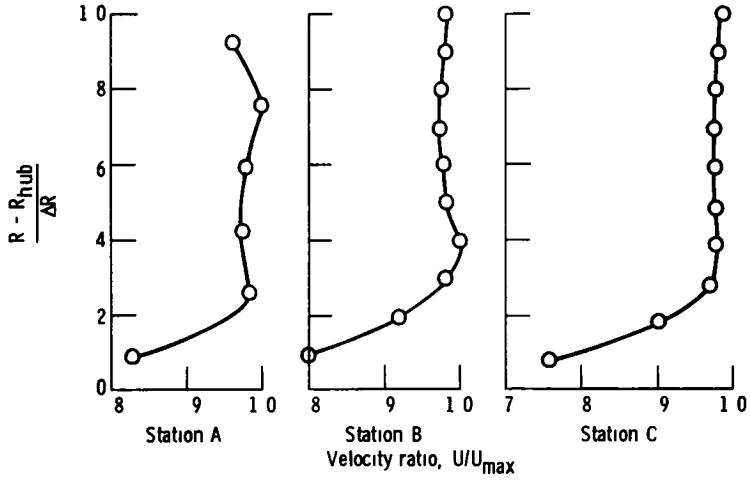

(c) $\overline{M}_{inlet} = 0.75$

Figure 37 - Continued

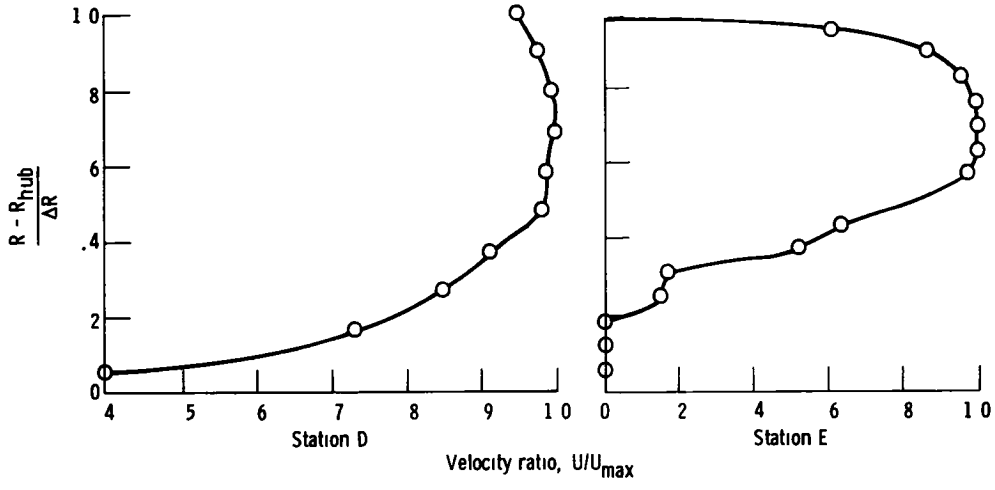

(c) Concluded

Figure 37 - Concluded

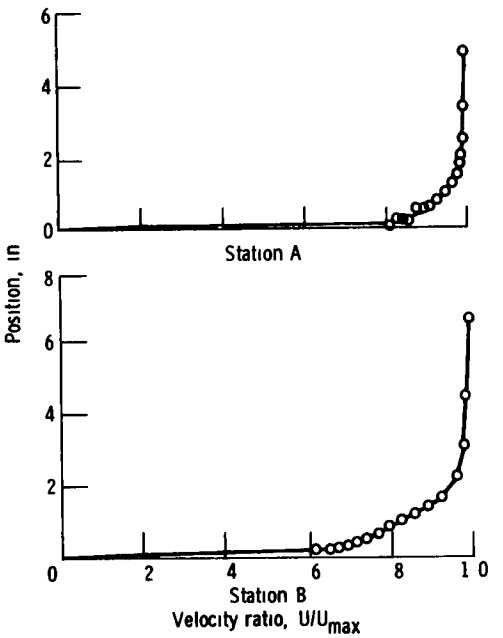

(a) $\overline{M}_{inlet}$ = 0 29

Figure 38 - Diffuser hub boundary-layer profiles with no vortex generators installed

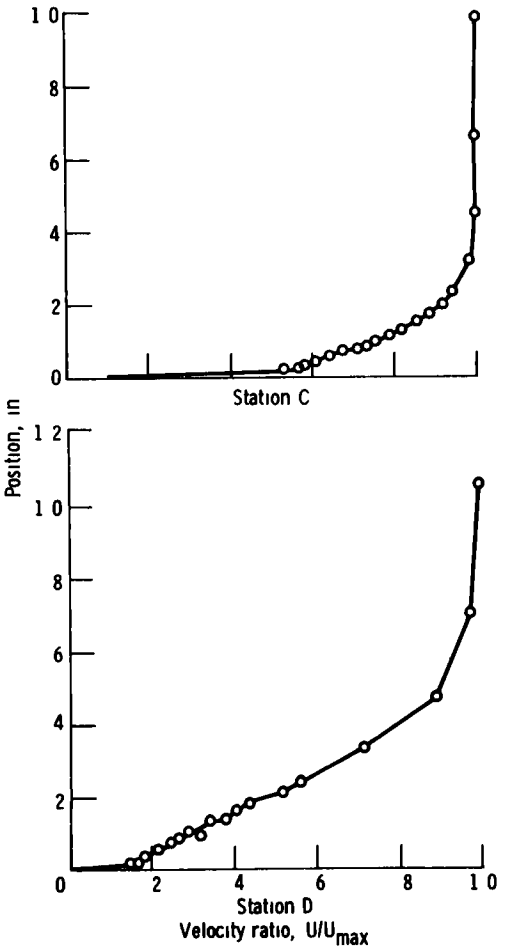

(a) Concluded.

Figure 38 - Continued

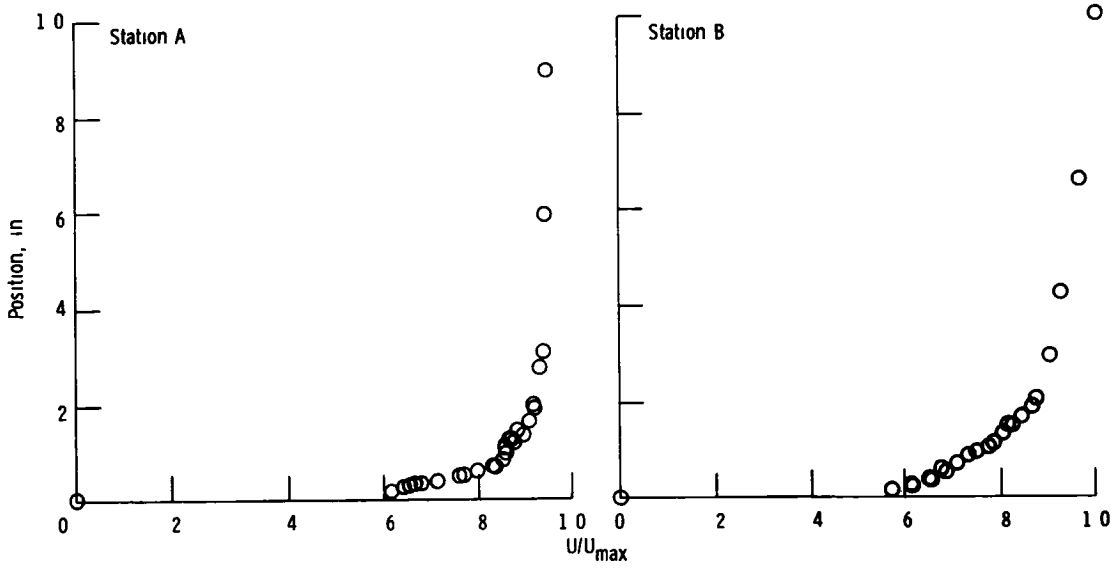

(b) $\bar{M}_{inlet}$ = 0 48

Figure 38 - Continued

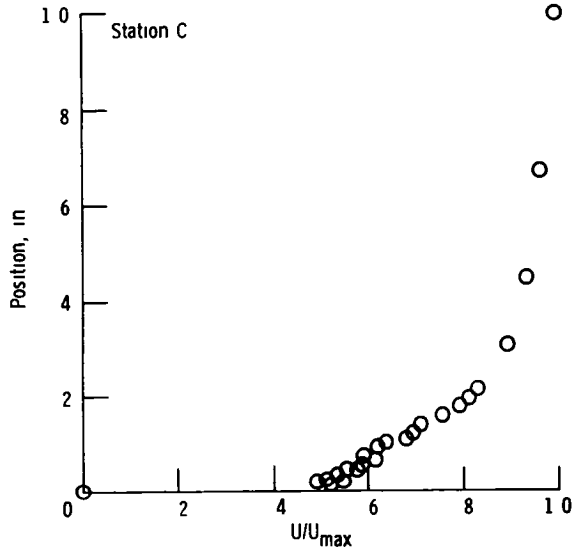

(b) Continued

Figure 38 - Continued

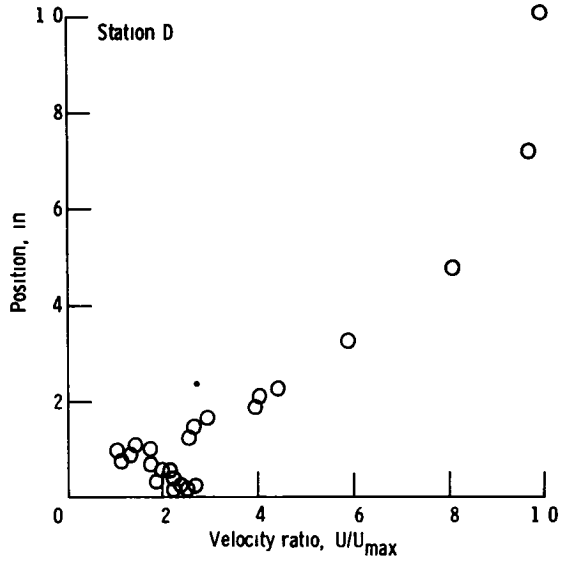

(b) Concluded.

Figure 38 - Continued

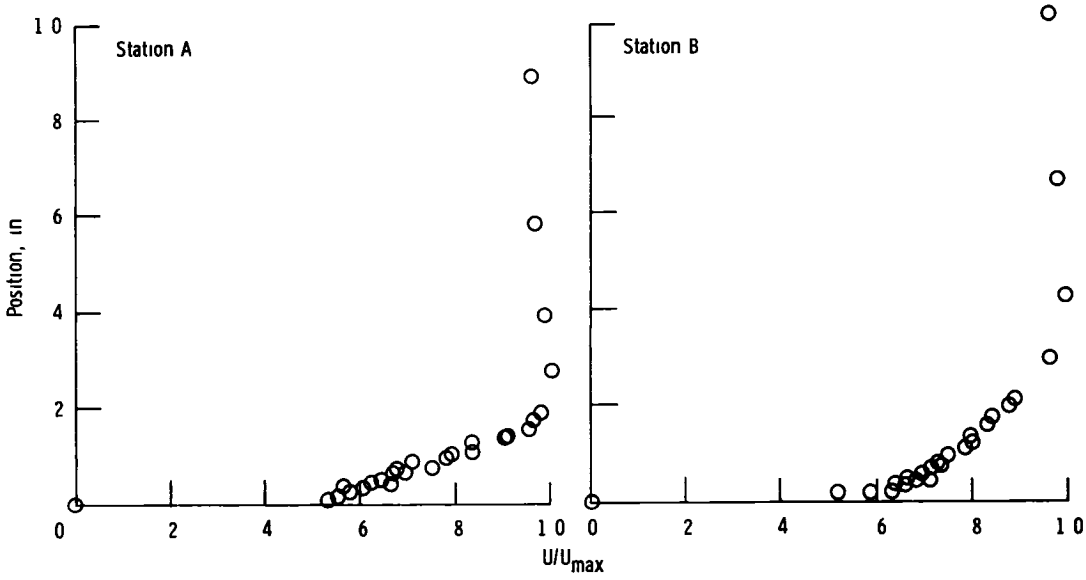

(c) $\bar{M}_{inlet}$ = 0 75

Figure 38 - Continued

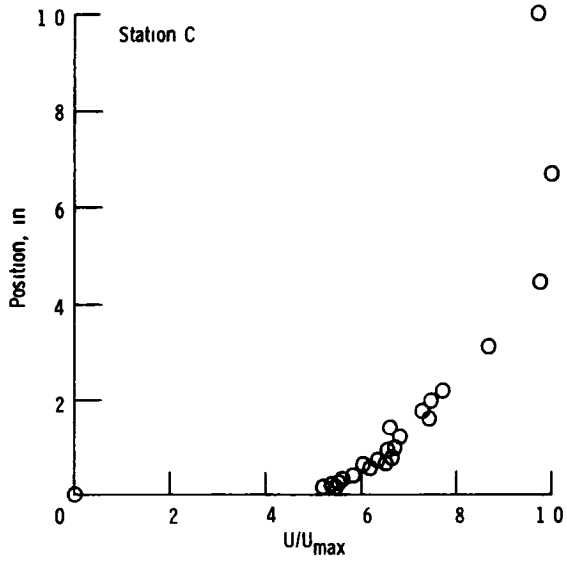

(c) Continued

Figure 38 - Continued

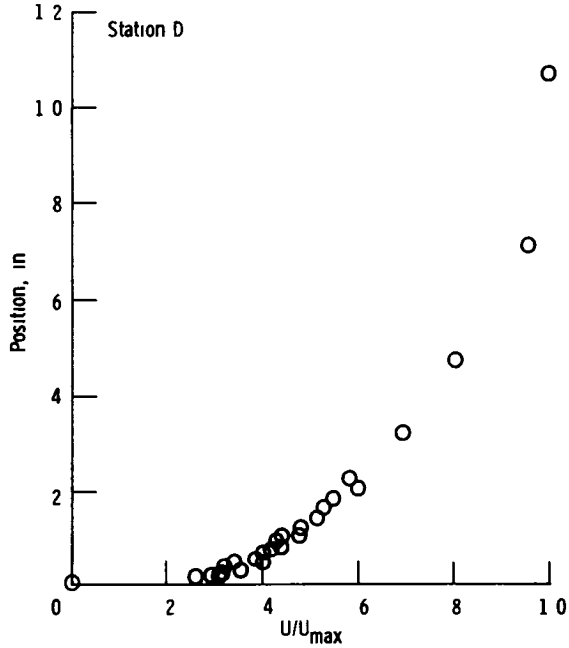

(c) Concluded

Figure 38 - Concluded

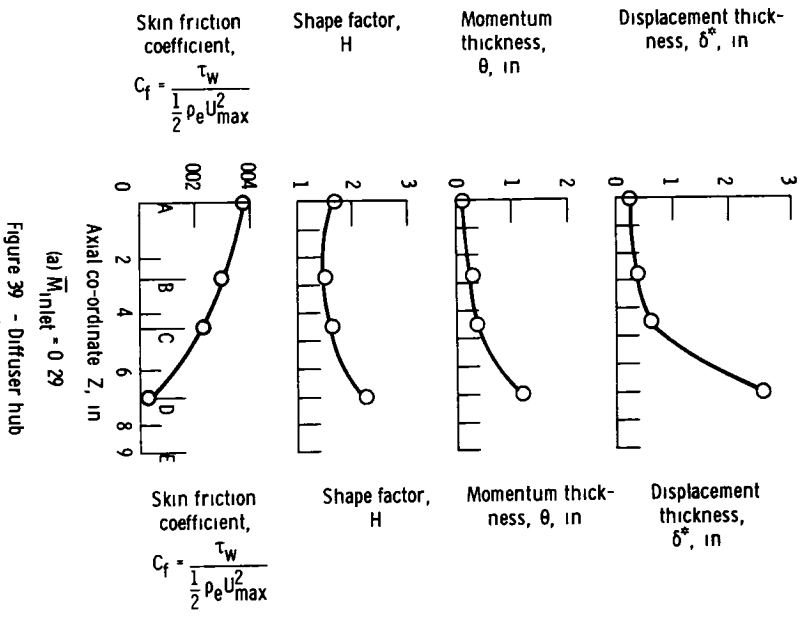

(a) $\bar{M}_{inlet} = 0.29$

Figure 39 - Diffuser hub boundary layer property variations with no vortex generators installed

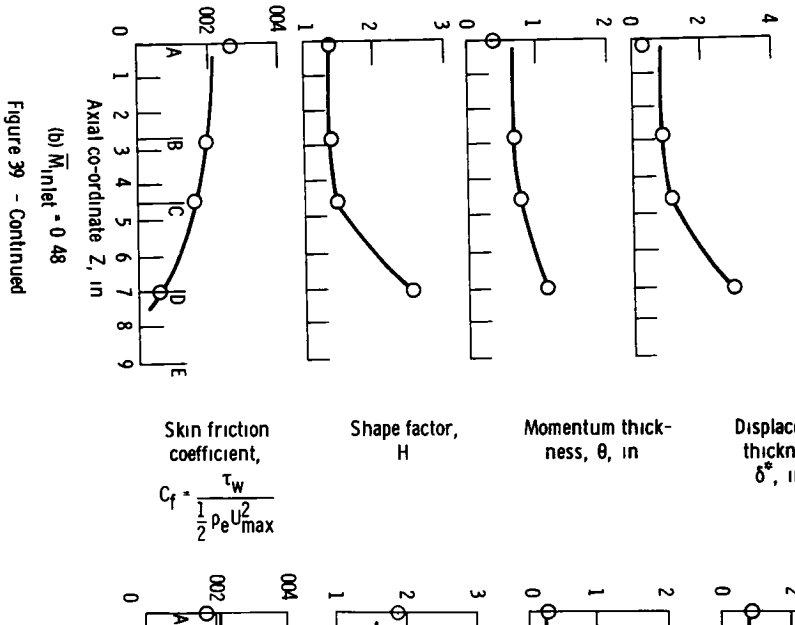

(b) $\bar{M}_{inlet} = 0.48$

Figure 39 - Continued

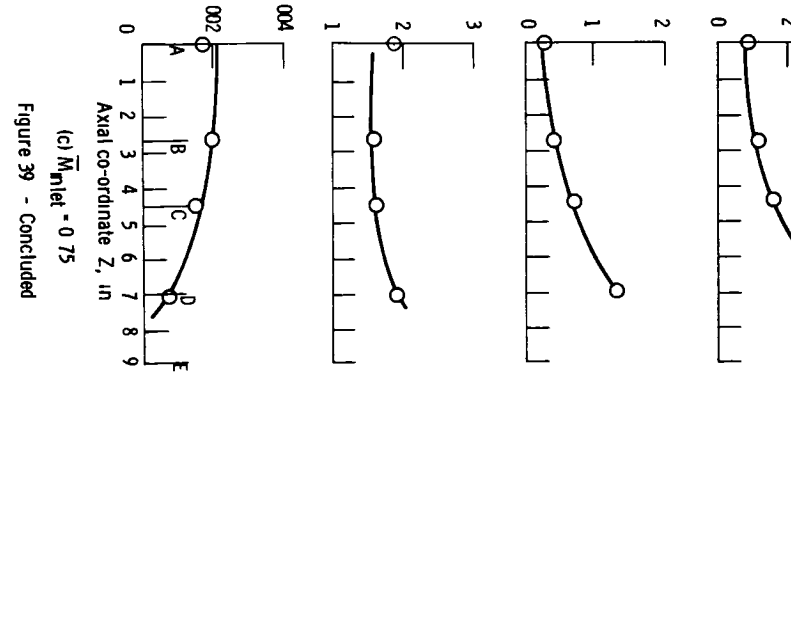

(c) $\bar{M}_{inlet} = 0.75$

Figure 39 - Concluded

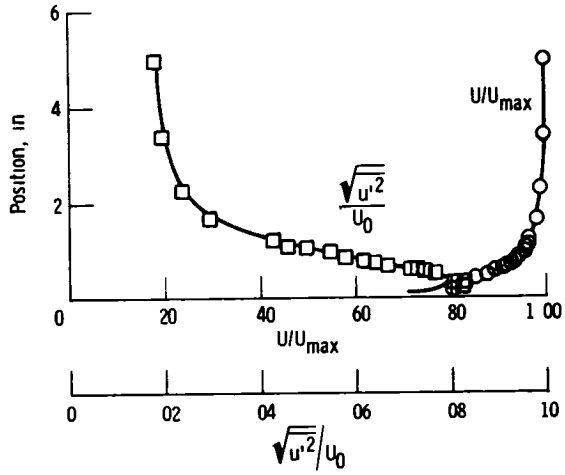

(a) Station A

Figure 40 - Diffuser hub boundary layer property profiles with no vortex generators installed, $\bar{M}_{inlet}$ = 0 29

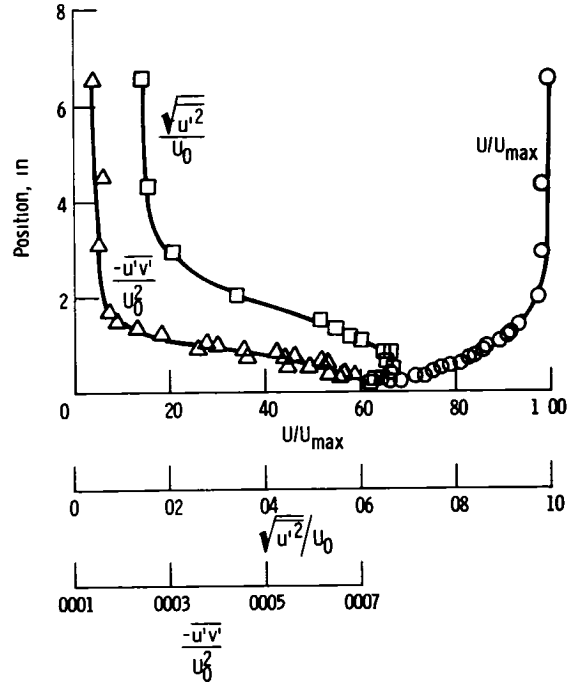

(b) Station B

Figure 40 - Continued

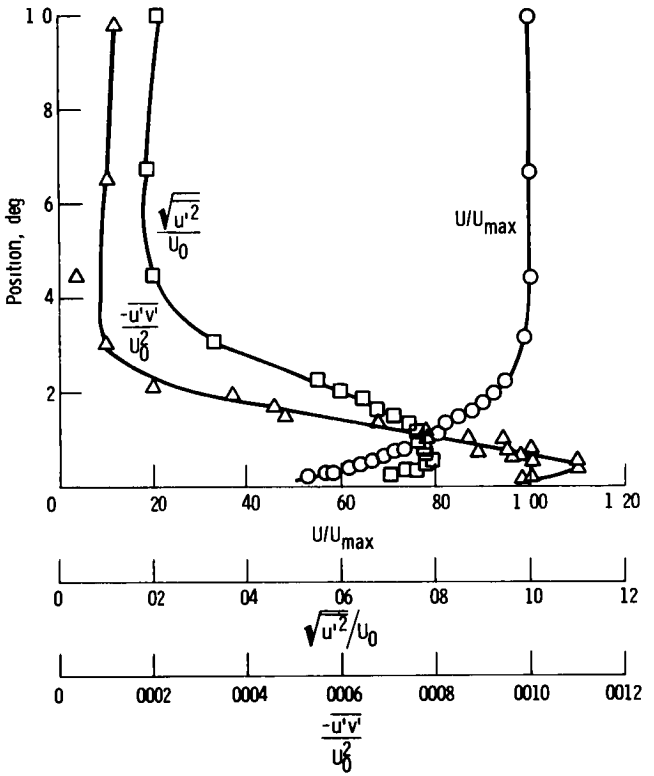

(c) Station C

Figure 40 - Continued

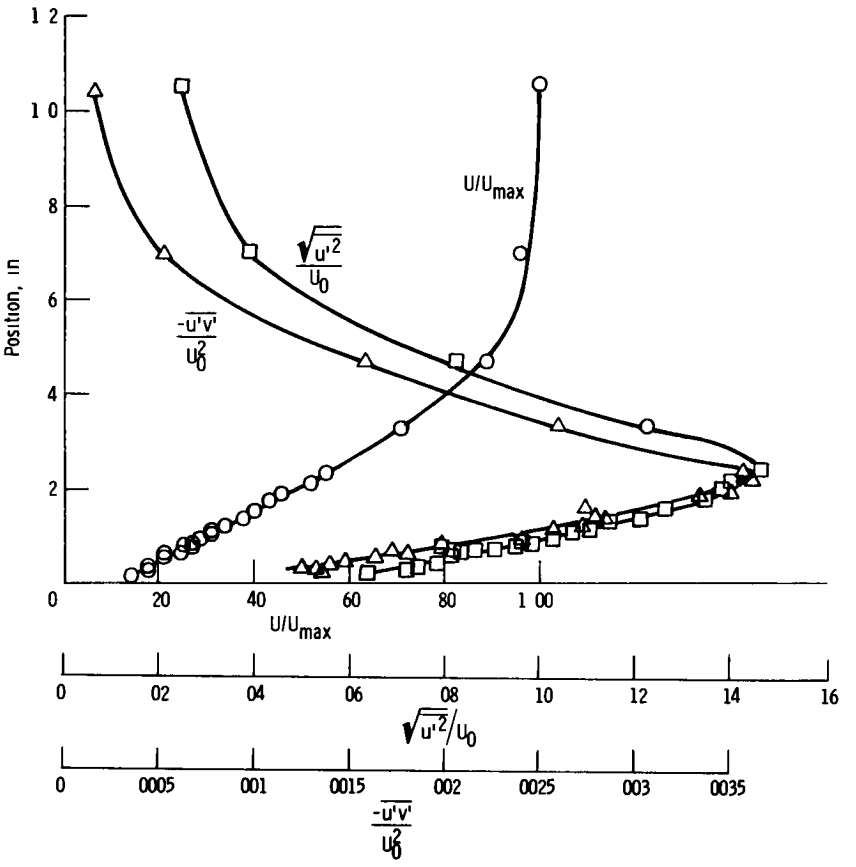

(d) Station D

Figure 40 - Concluded

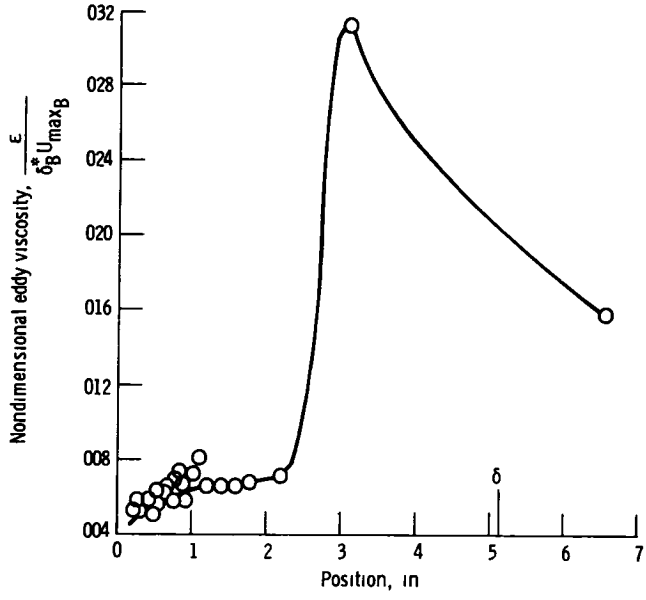

(a) Station B

Figure 41 - Nondimensional eddy viscosity distributions for hub boundary layer

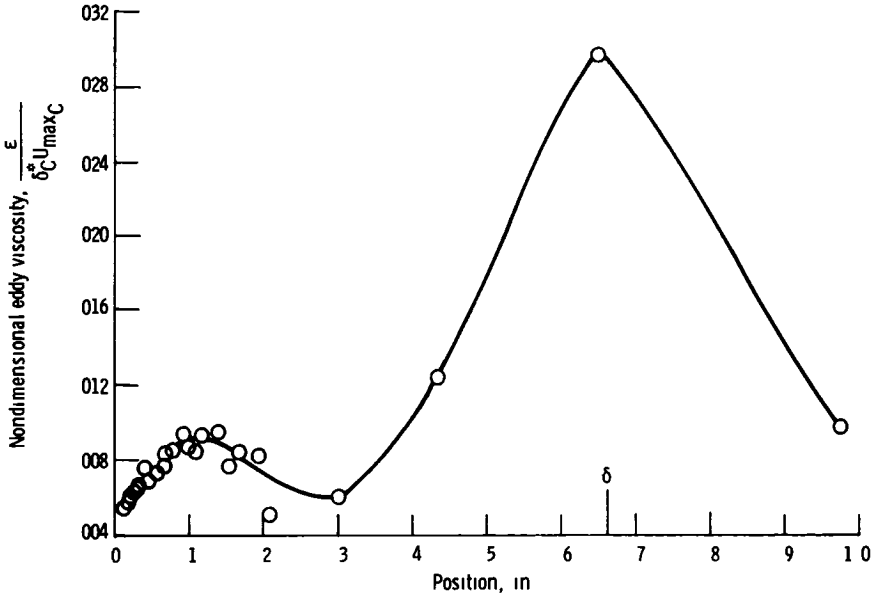

(b) Station C

Figure 41 - Continued

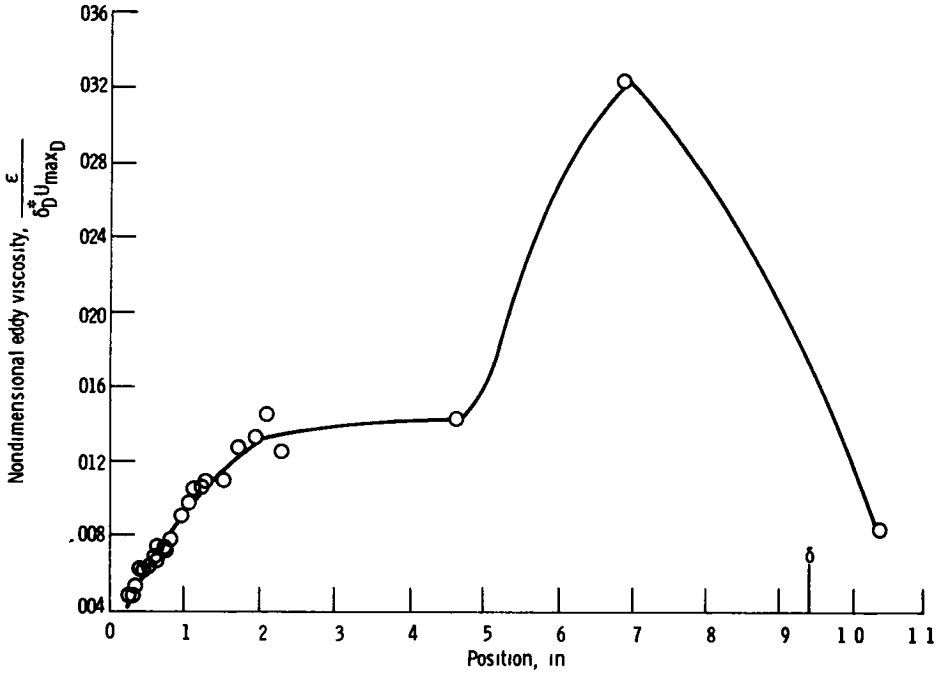

(c) Station D

Figure 41 - Concluded

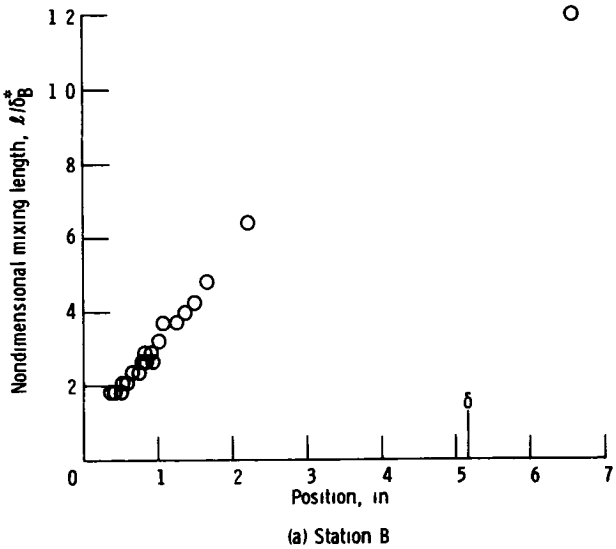

(a) Station B

Figure 42 - Nondimensional mixing length distributions for hub boundary layer

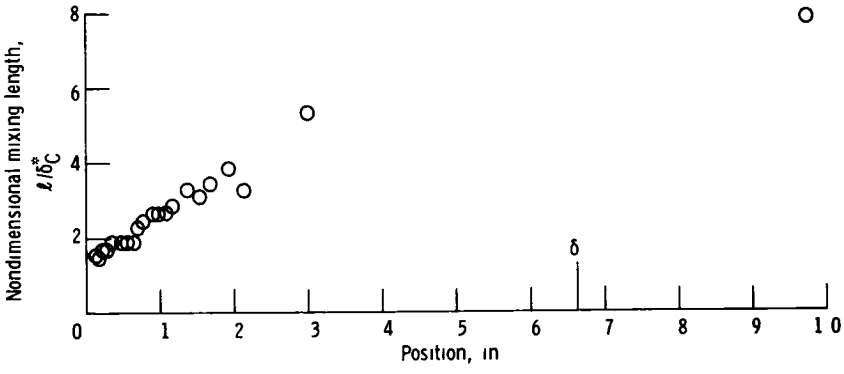

(b) Station C

Figure 42 - Continued

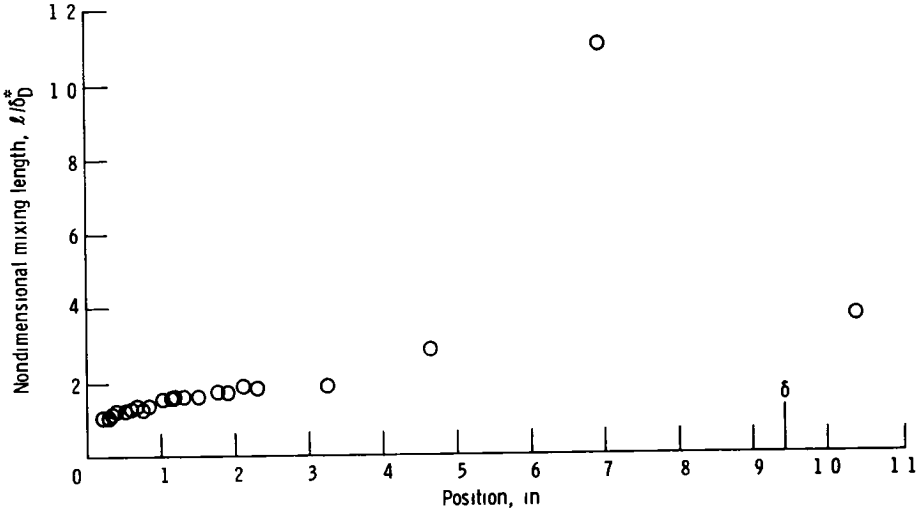

(c) Station D

Figure 42 - Concluded

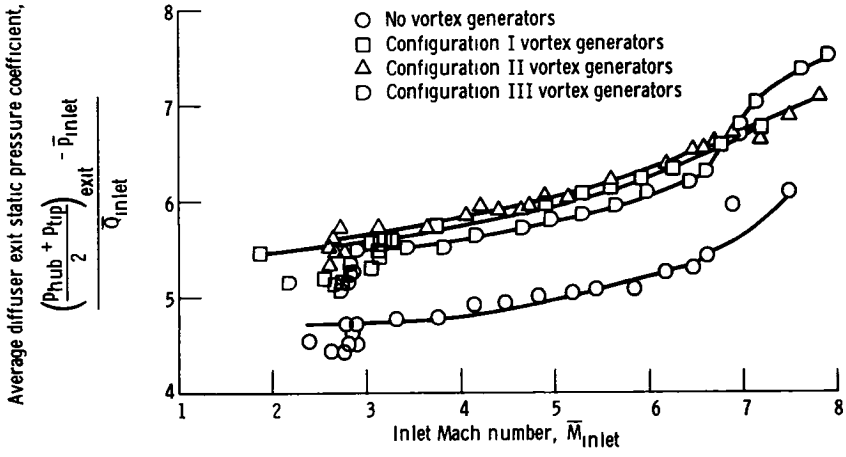

Figure 43 - Average diffuser exit static pressure coefficient variation with average inlet Mach number

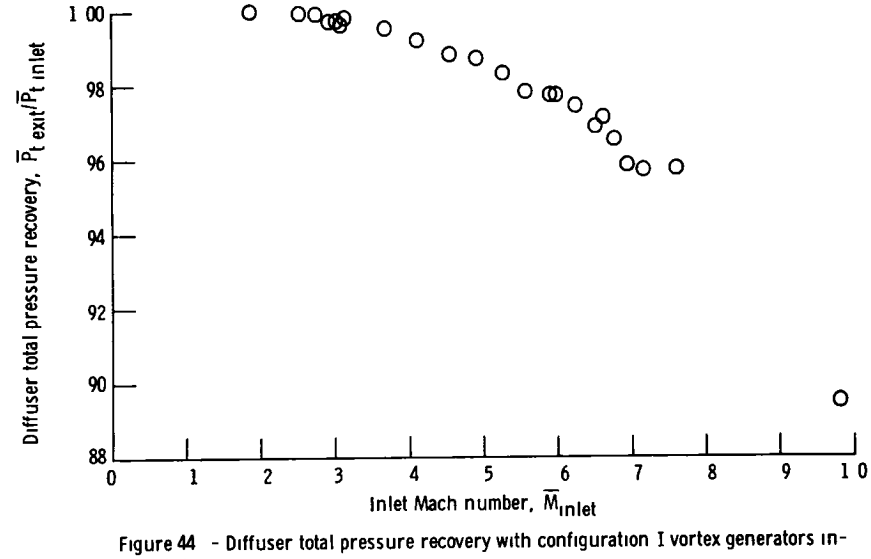

Figure 44 - Diffuser total pressure recovery with configuration I vortex generators installed

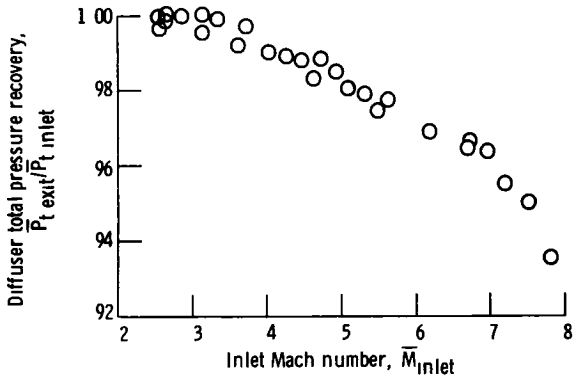

Figure 45 - Diffuser total pressure recovery with configuration II vortex generators installed

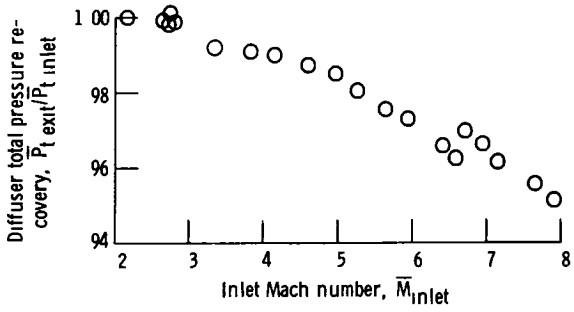

Figure 46 - Diffuser total pressure recovery with configuration III vortex generators installed

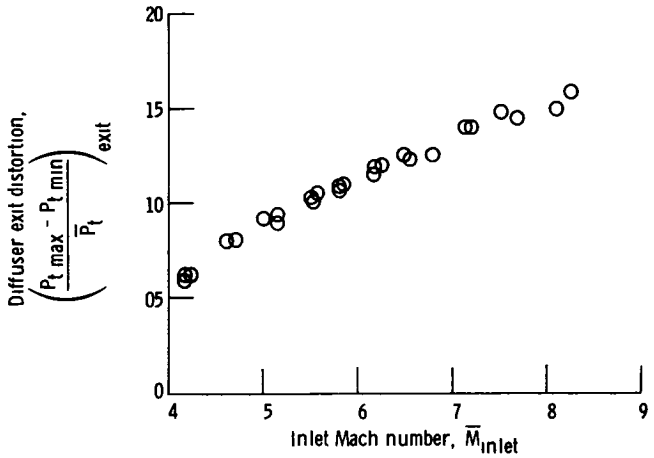

Figure 47 - Diffuser exit total pressure distortion with configuration I vortex generators installed

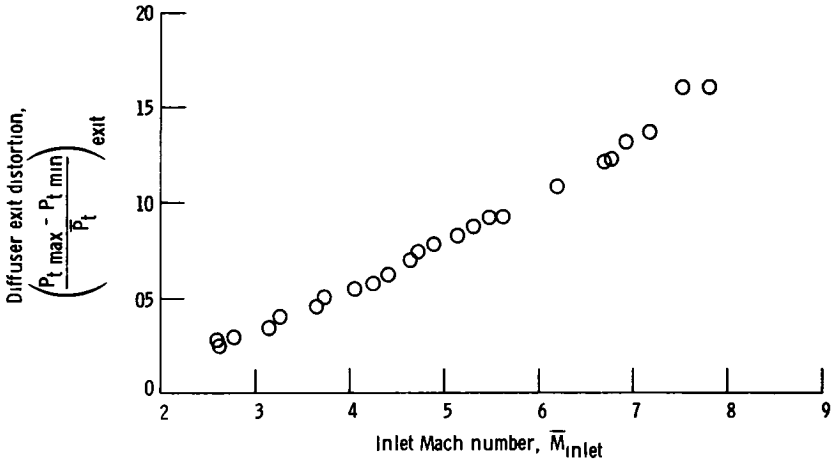

Figure 48 - Diffuser exit total pressure distortion with configuration II vortex generators installed

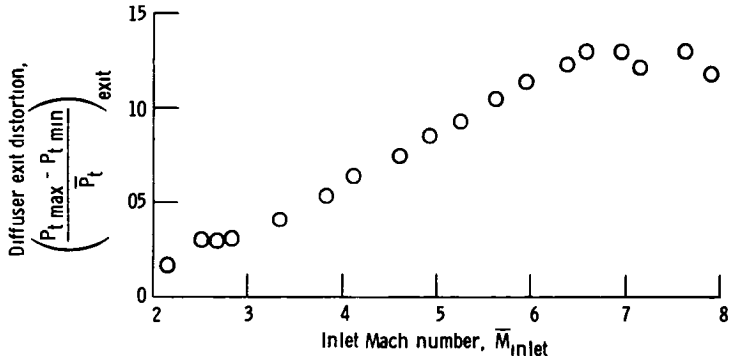

Figure 49 - Diffuser exit total pressure distortion with configuration III vortex generators installed

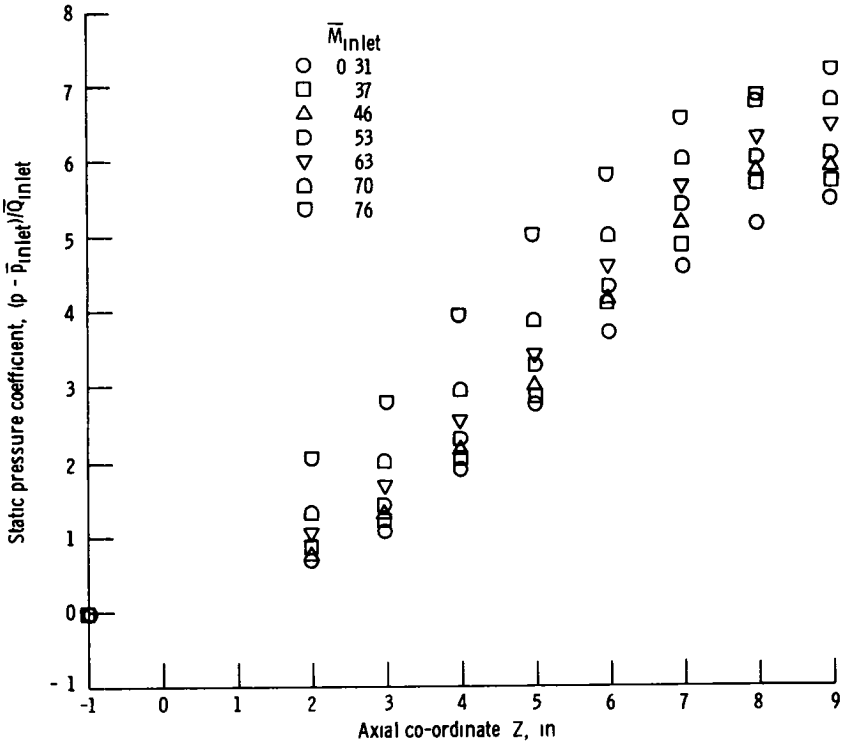

(a) Hub surface

Figure 50 - Surface static pressure coefficient variation with configuration I vortex generators installed

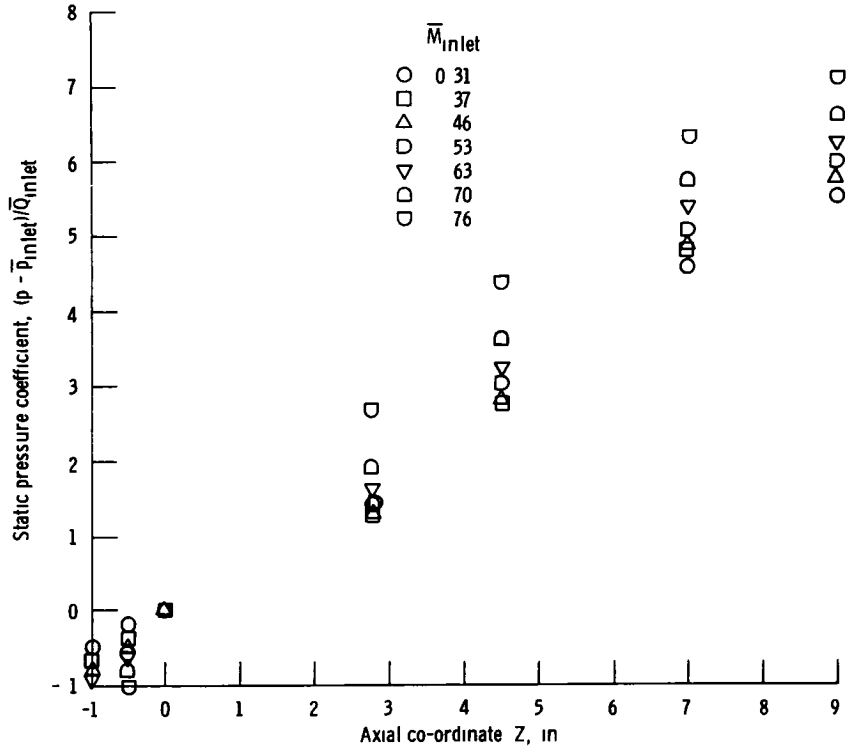

(b) Tip surface

Figure 50 - Concluded

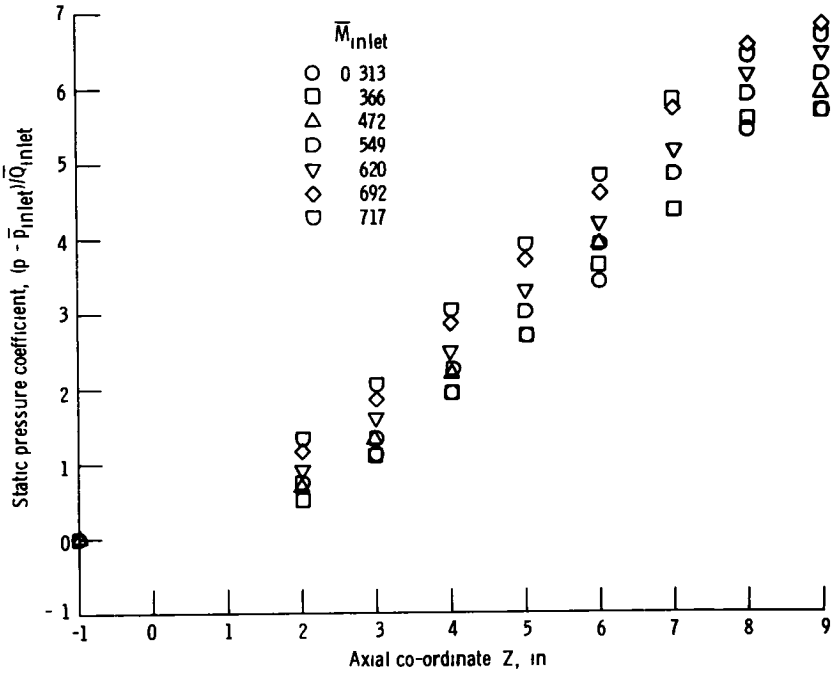

(a) Hub surface

Figure 51 - Surface static pressure coefficient variation with configuration II vortex generators installed

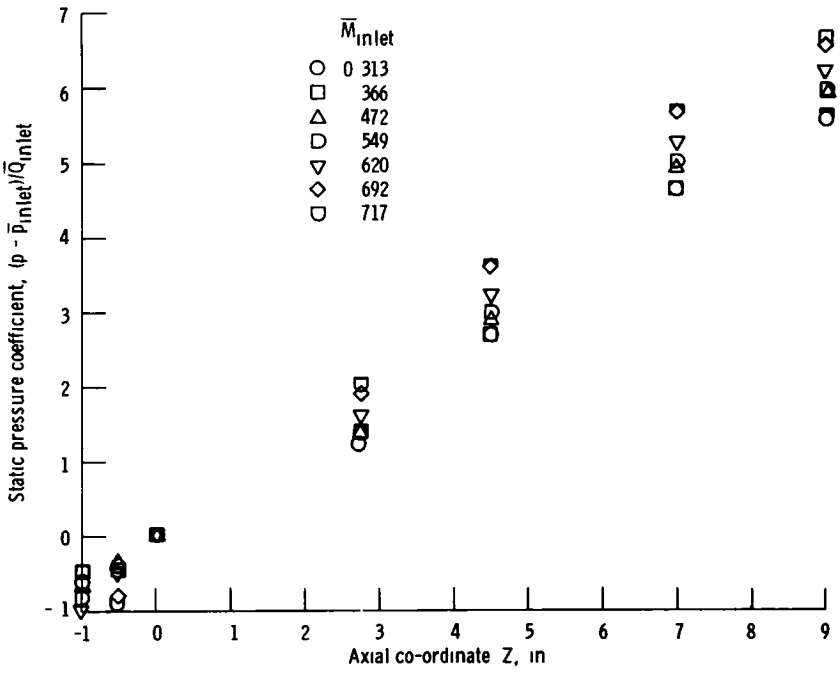

(b) Tip surface

Figure 51 - Concluded

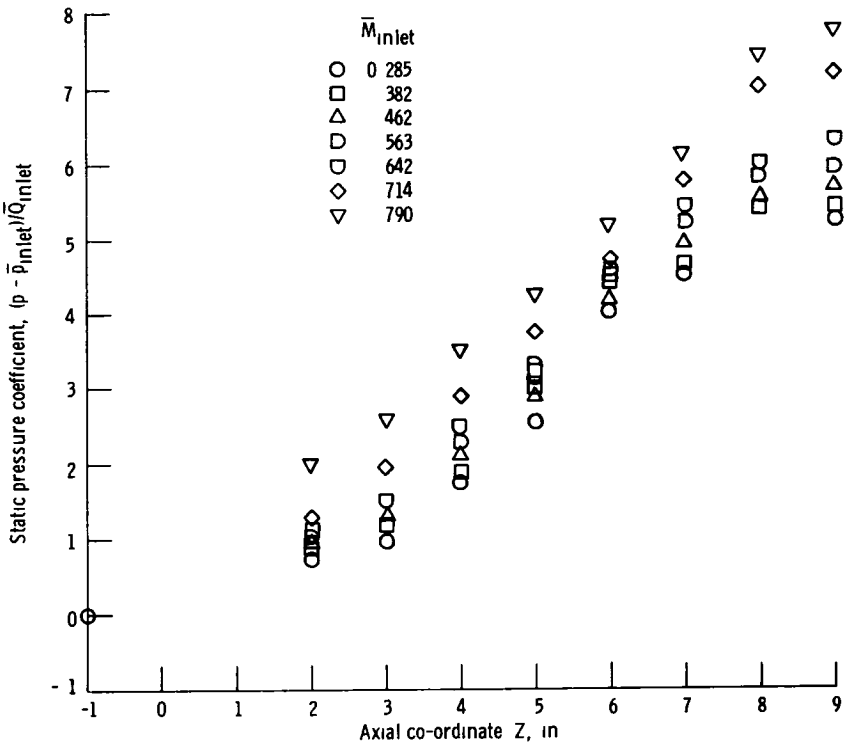

(a) Hub surface

Figure 52 - Surface static pressure coefficient variation with configuration III vortex generators installed

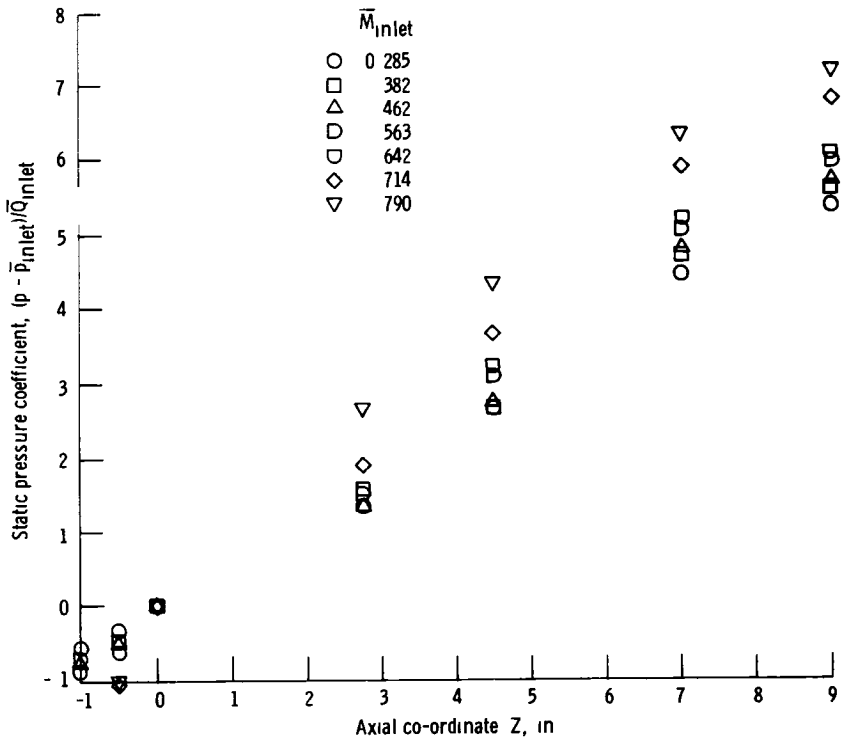

(b) Tip surface

Figure 52 - Concluded

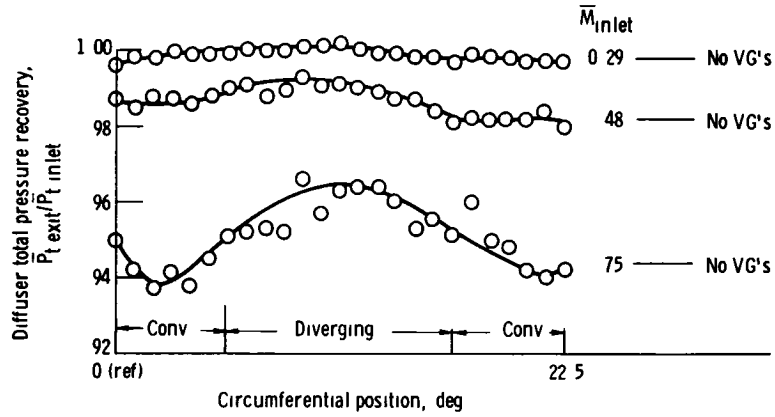

Figure 53 - Circumferential variation in diffuser total pressure recovery with configuration I vortex generators installed

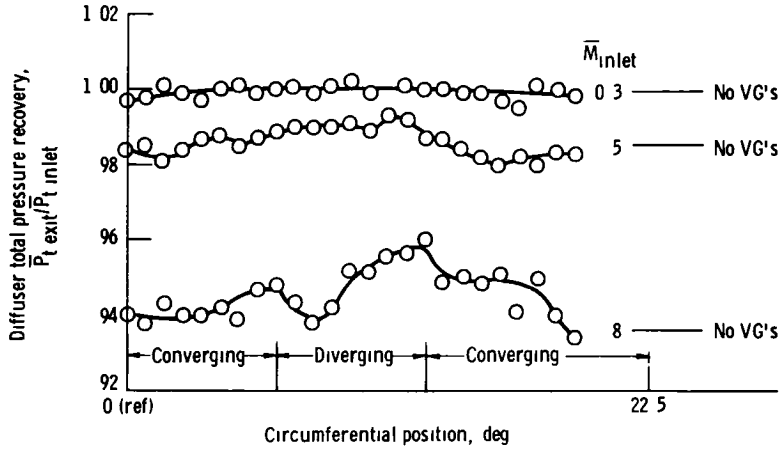

Figure 54 - Circumferential variation in diffuser total pressure recovery with configuration II vortex generators installed

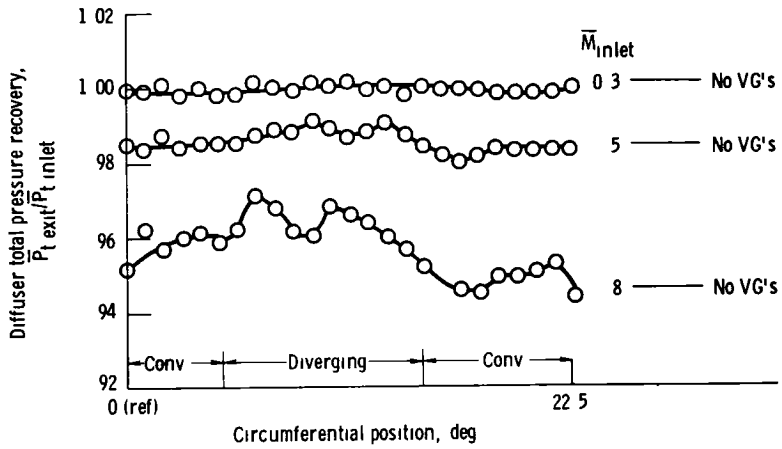

Figure 55 - Circumferential variation in diffuser total pressure recovery with configuration III vortex generators installed

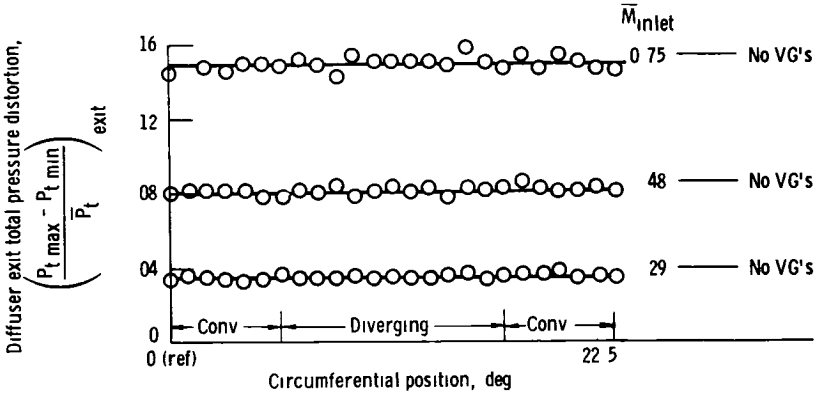

Figure 56 - Circumferential variation of diffuser exit total pressure distortion with configuration I vortex generators installed

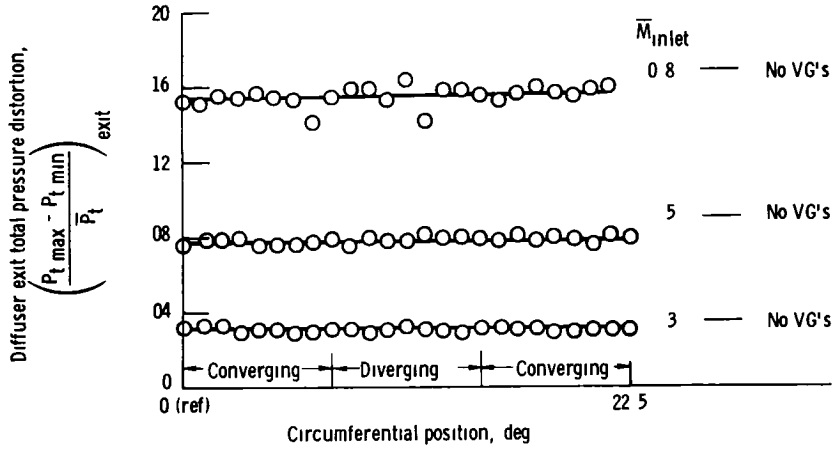

Figure 57 - Circumferential variation of diffuser exit total pressure distortion with configuration II vortex generators installed

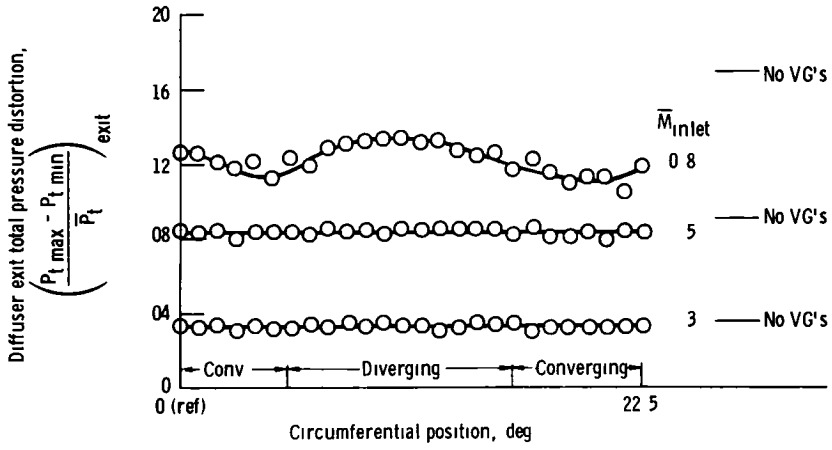

Figure 58 - Circumferential variation of diffuser exit total pressure distortion with configuration III vortex generators installed

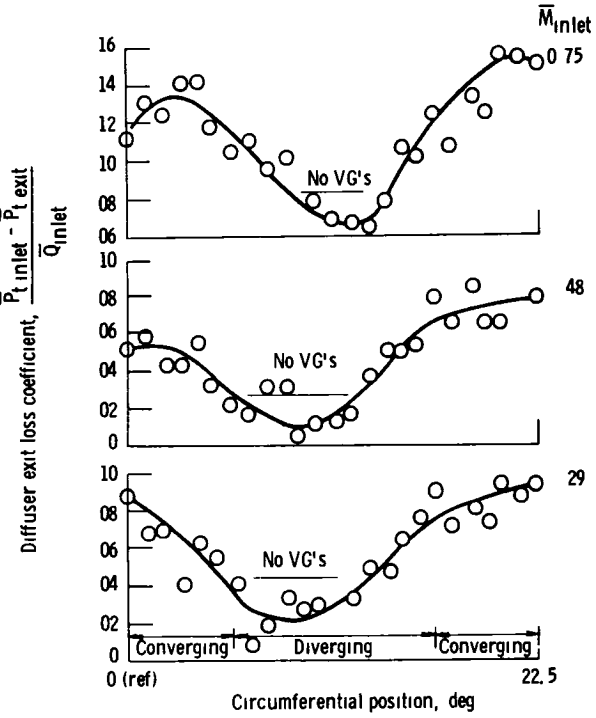

Figure 59 - Circumferential variation of diffuser exit loss coefficient with configuration I vortex generators installed

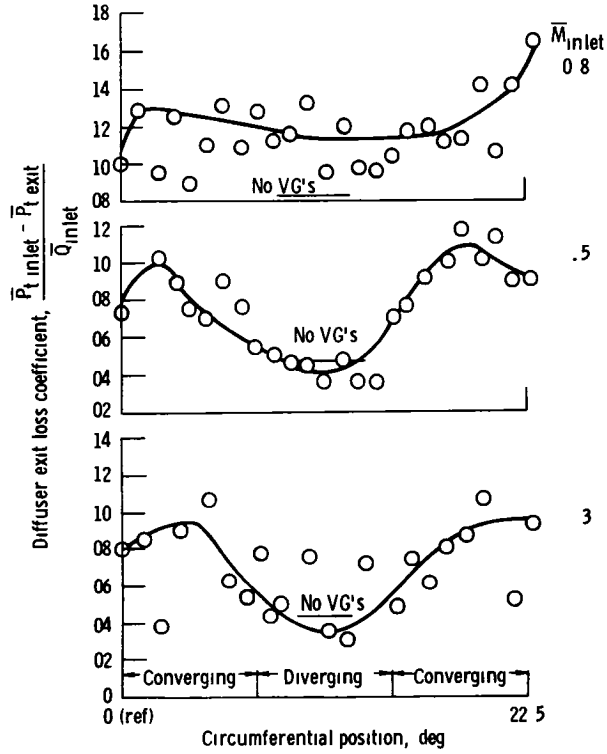

Figure 60 - Circumferential variation of diffuser exit loss coefficient with configuration II vortex generators installed

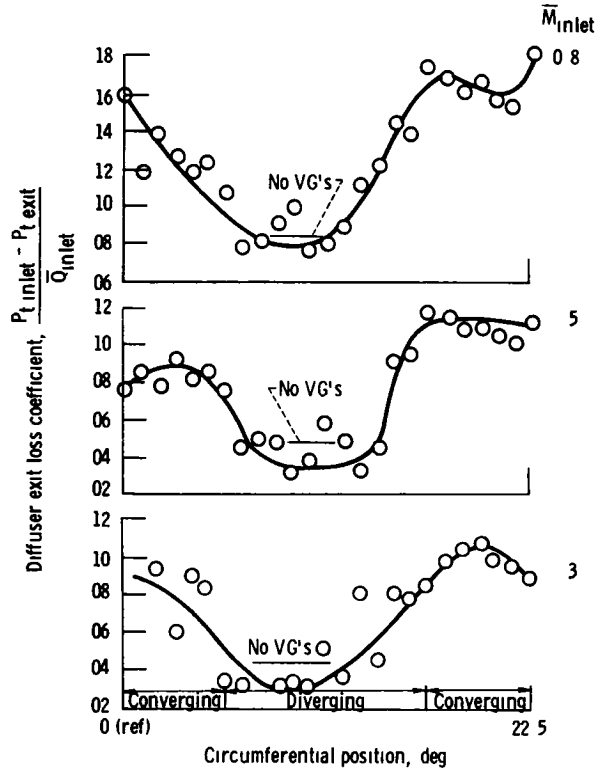

Figure 61 - Circumferential variation of diffuser exit loss coefficient with configuration III vortex generators installed

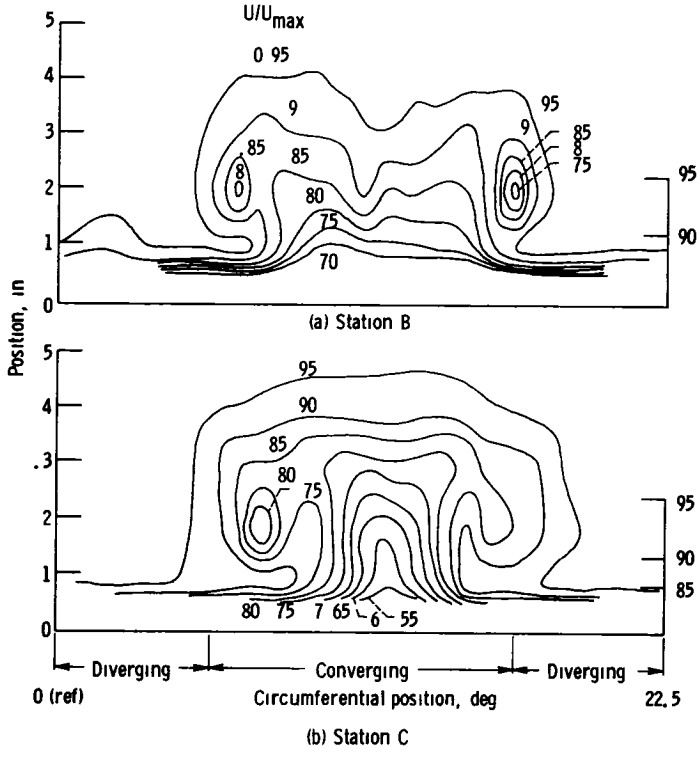

Figure 62 - Rake velocity contours for configuration I vortex generators installed, $\bar{M}_{inlet} = 0\ 29$

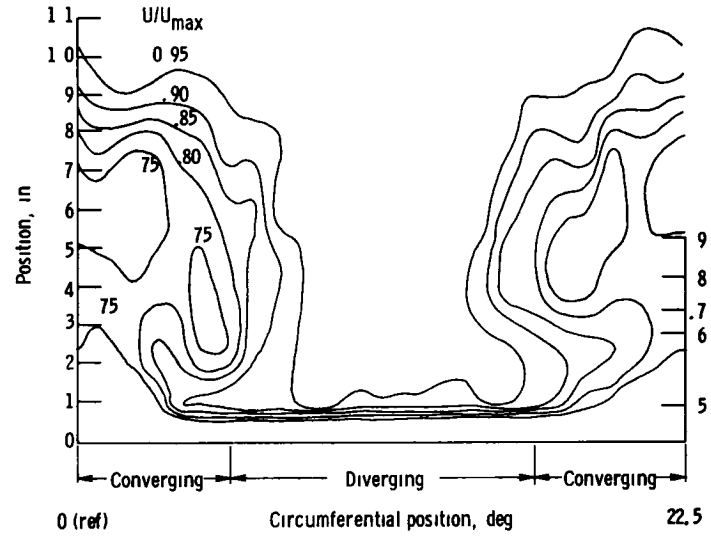

(c) Station D

Figure 62 - Continued

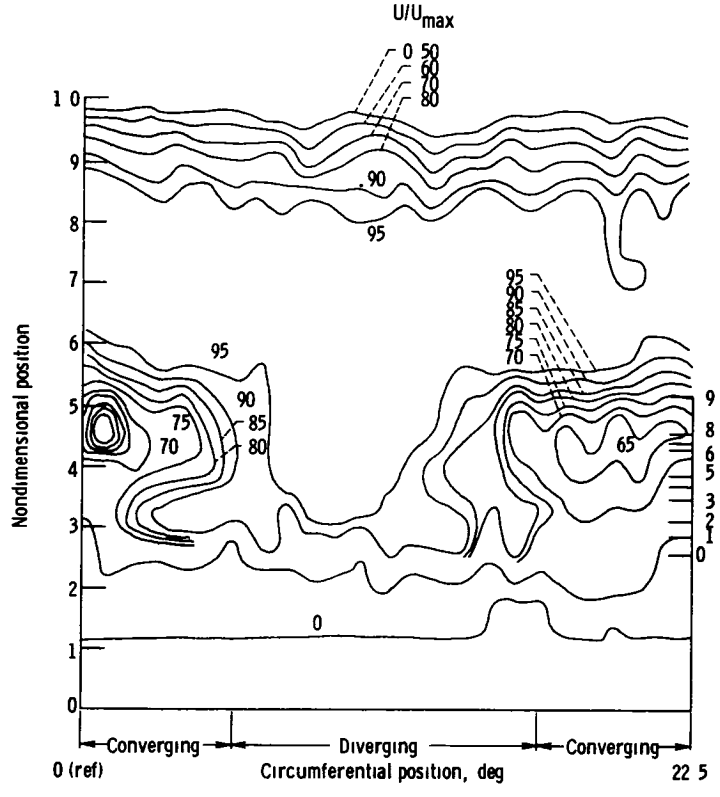

(d) Station E.

Figure 62 - Concluded

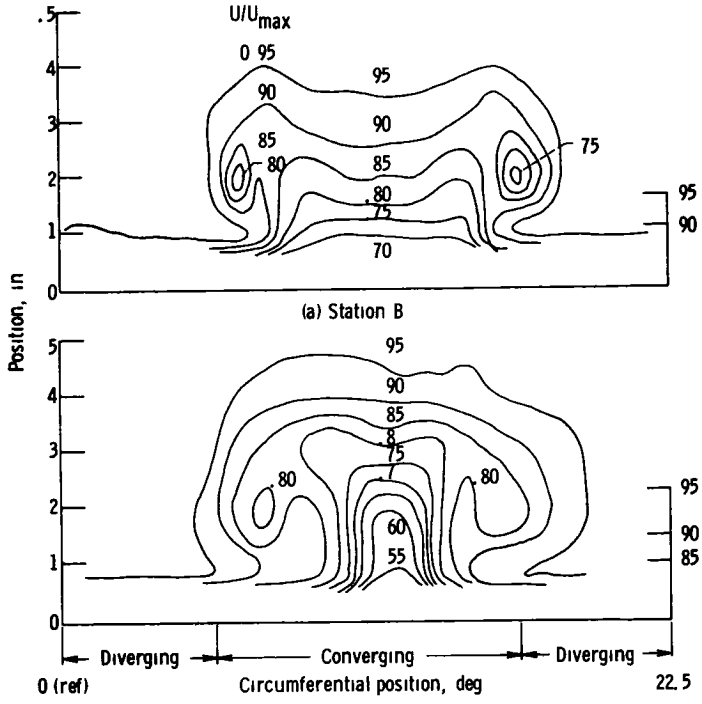

(a) Station B

(b) Station C

Figure 63 - Rake velocity contours for configuration I vortex generators installed, $\overline{M}_{inlet}$ = 0 49

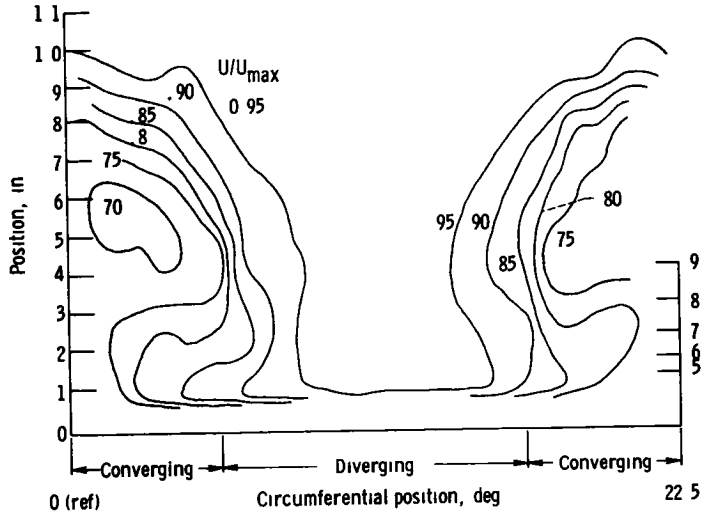

(c) Station D

Figure 63 - Continued

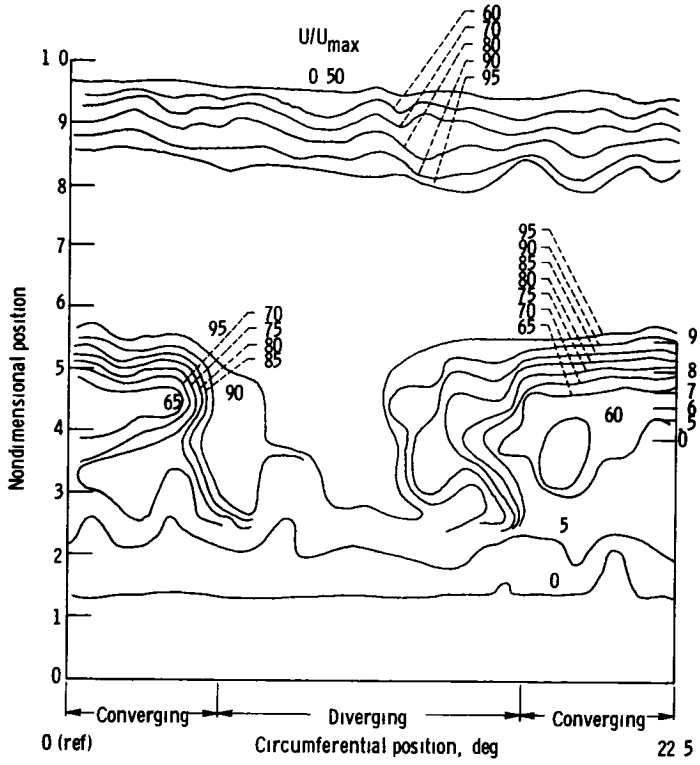

(d) Station E.

Figure 63 - Concluded

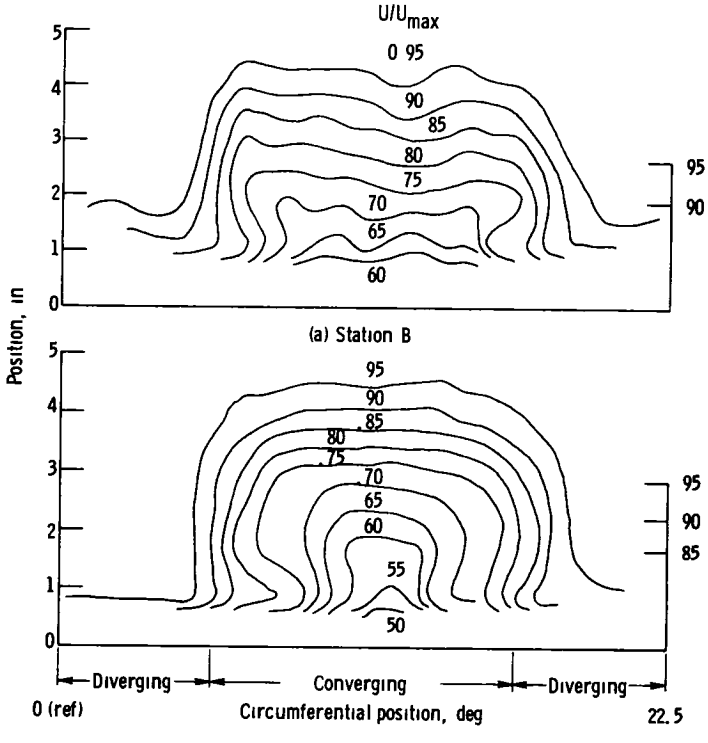

(a) Station B

(b) Station C

Figure 64 - Rake velocity contours for configuration I vortex generators installed, $\bar{M}_{inlet}$ = 0 81

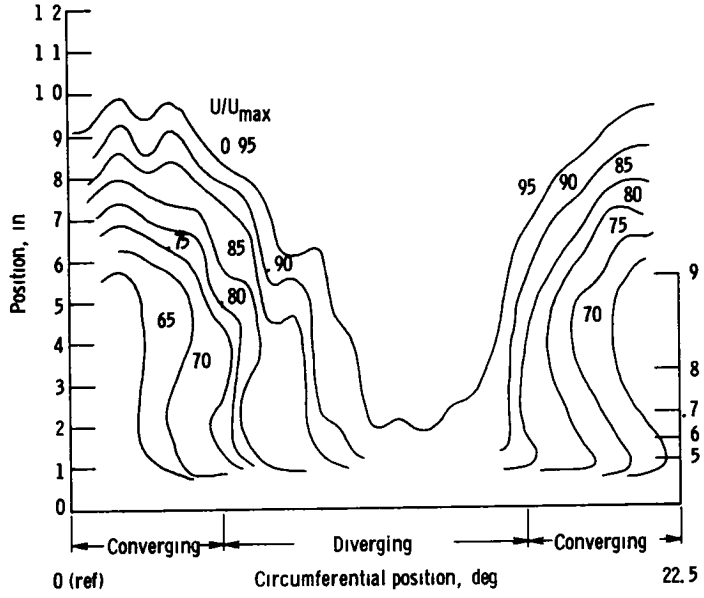

(c) Station D

Figure 64 - Continued

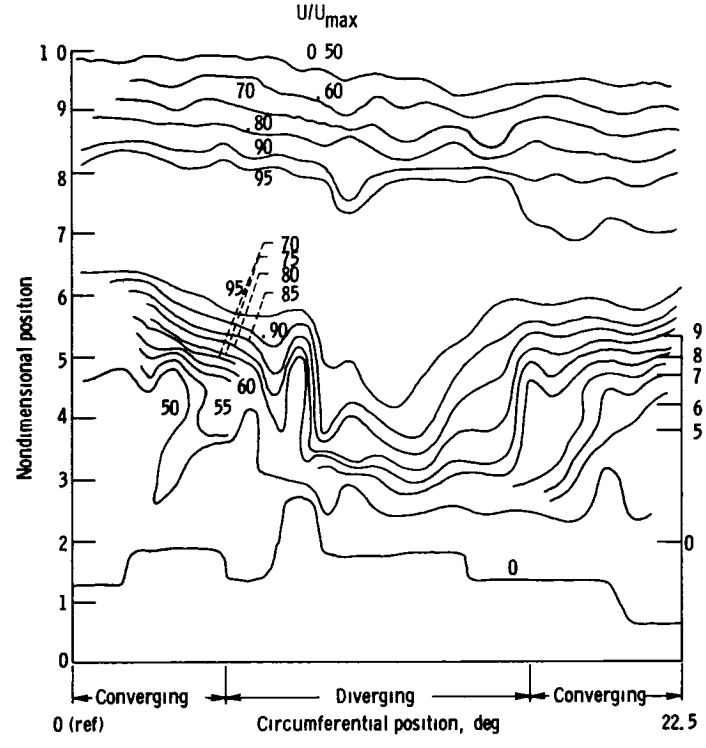

(d) Station E.

Figure 64 - Concluded

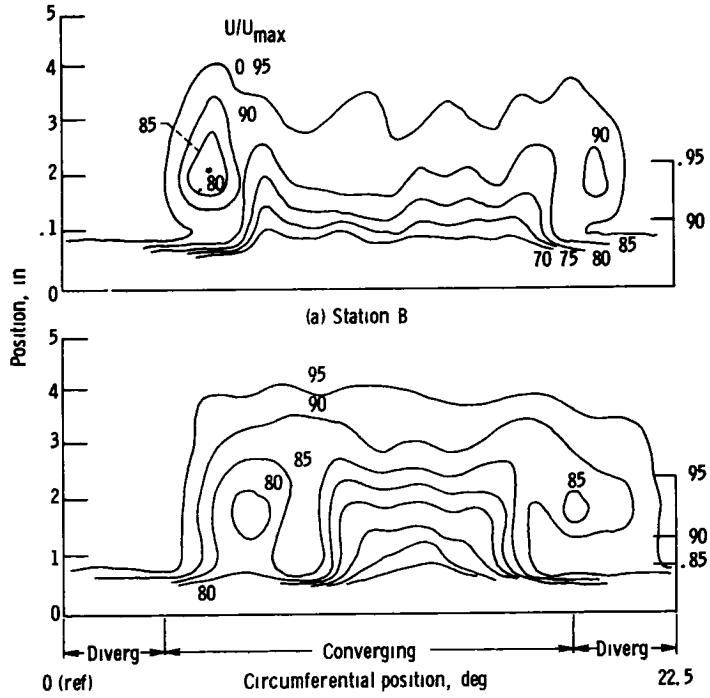

(a) Station B

(b) Station C

Figure 65 - Rake velocity contours for configuration II vortex generators installed, $\bar{M}_{inlet}$ = 0 29

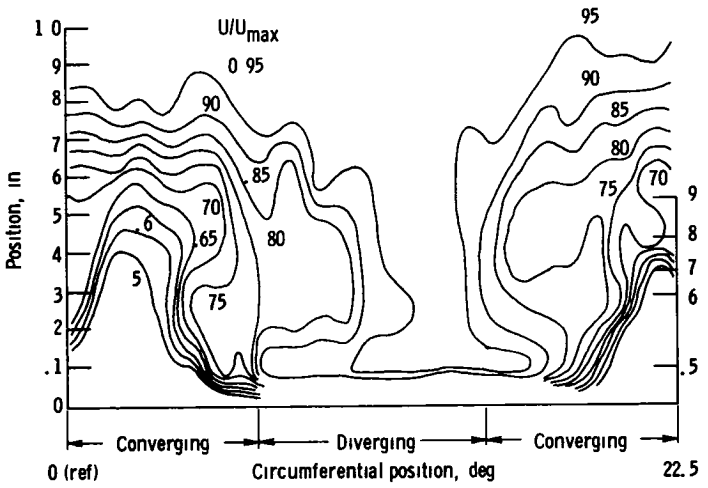

(c) Station D

Figure 65 - Continued

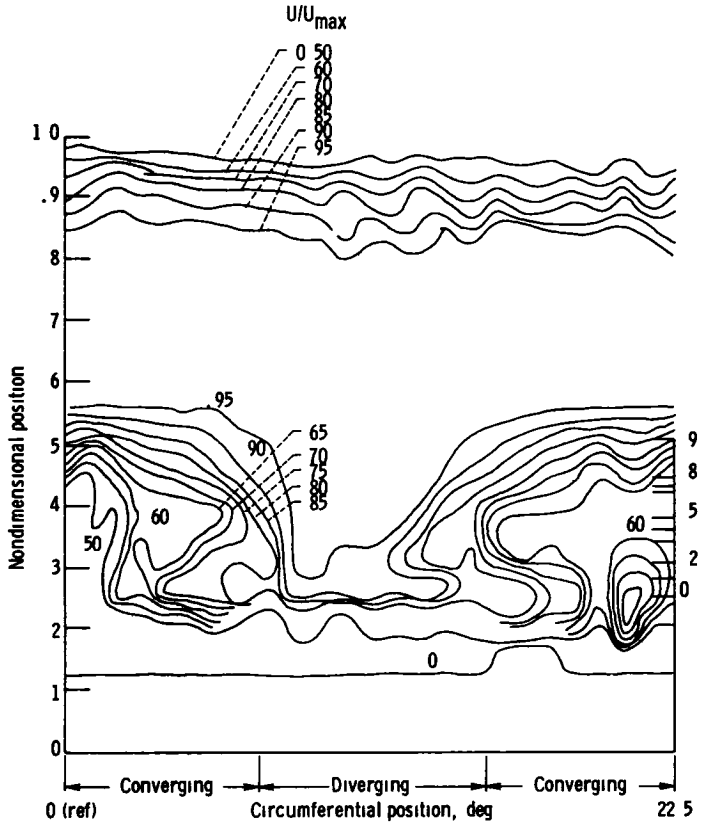

(d) Station E.

Figure 65 - Concluded

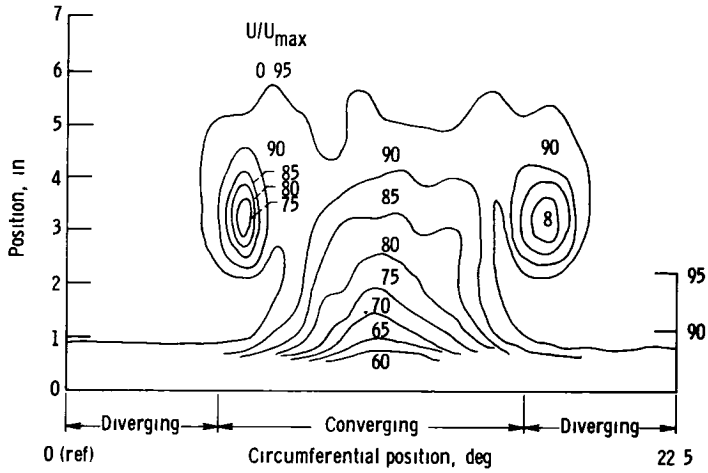

(a) Station B

Figure 66 - Rake velocity contours for configuration III vortex generators installed, $\bar{M}_{inlet} = 0.29$

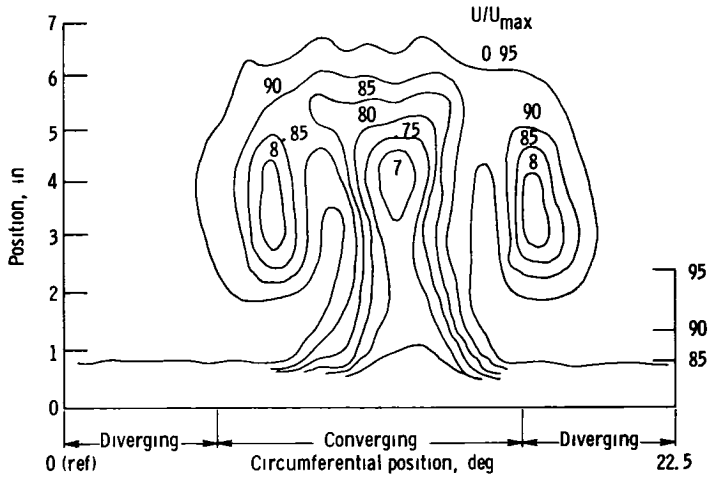

(b) Station C

Figure 66 - Continued

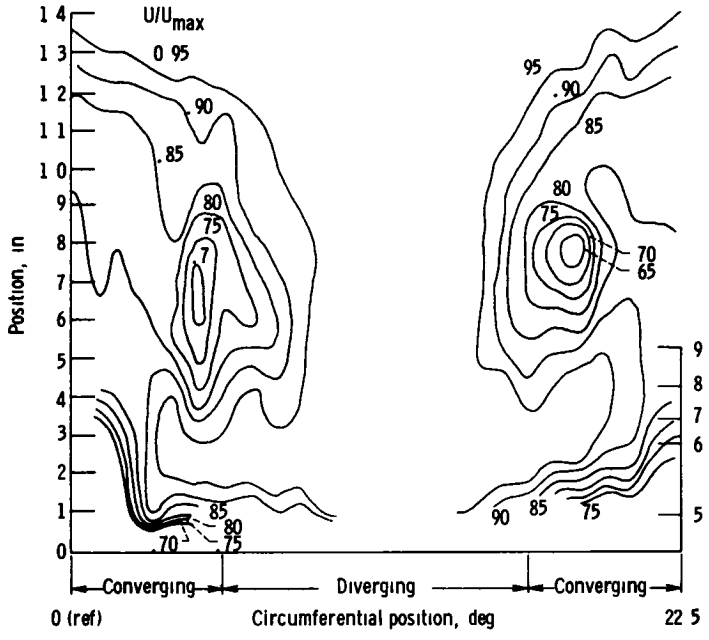

(c) Station D

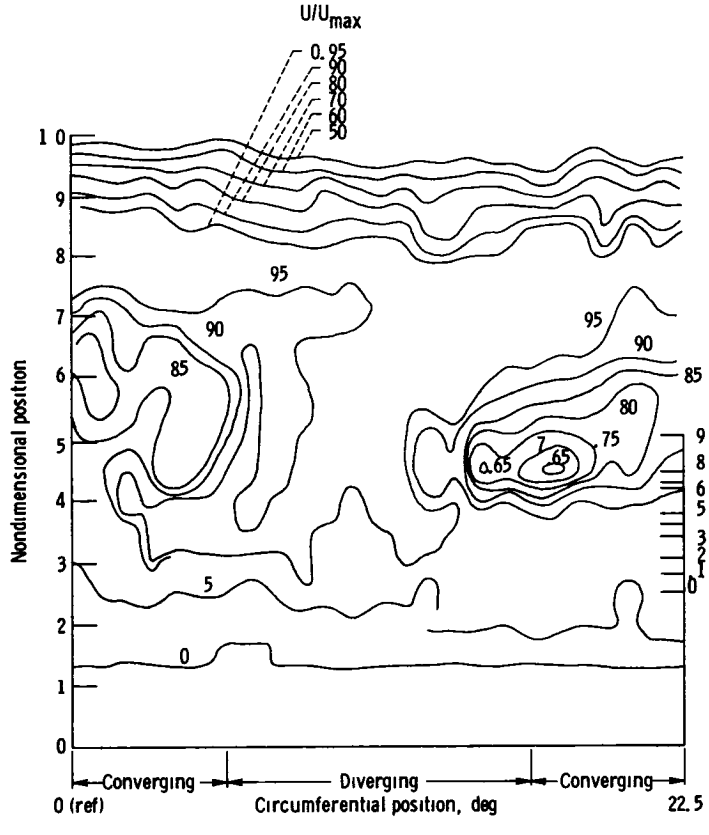

(d) Station E.

Figure 66 - Concluded

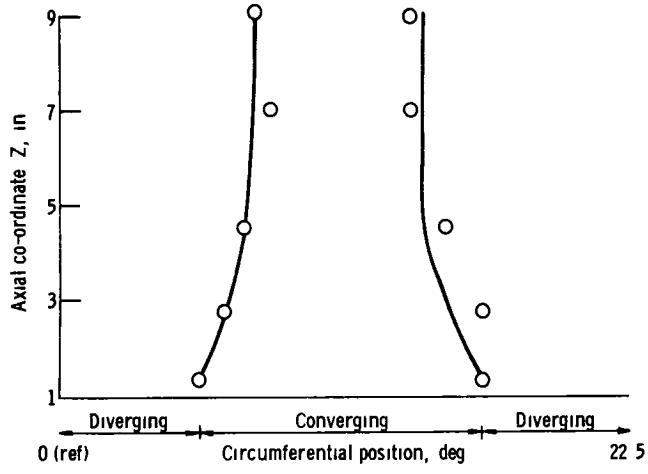

(a) Configuration I, $\bar{M}_{inlet} = 0.29$

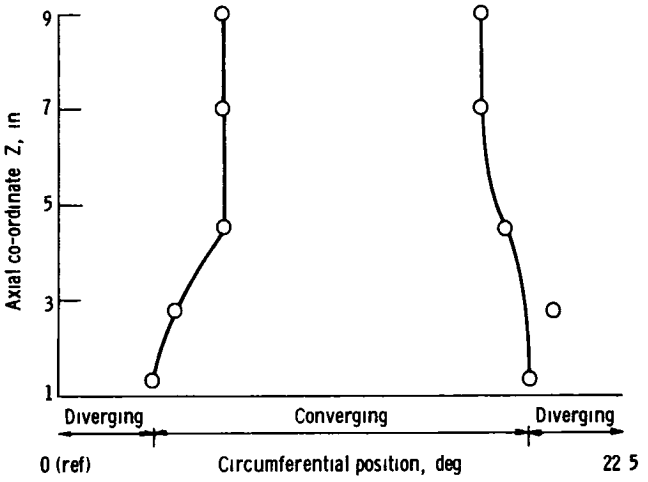

(b) Configuration II, $\bar{M}_{inlet} = 0.3$

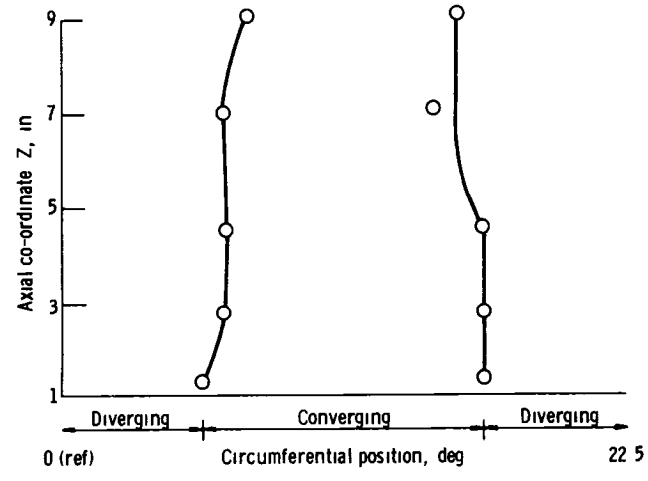

(c) Configuration III, $\bar{M}_{inlet} = 0.3$

Figure 67 - Vortex axial location.

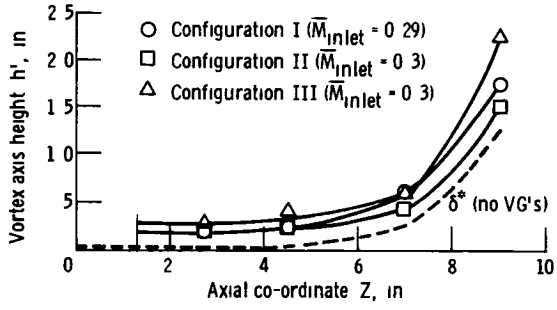

Figure 68 - Vortex axis height above hub surface

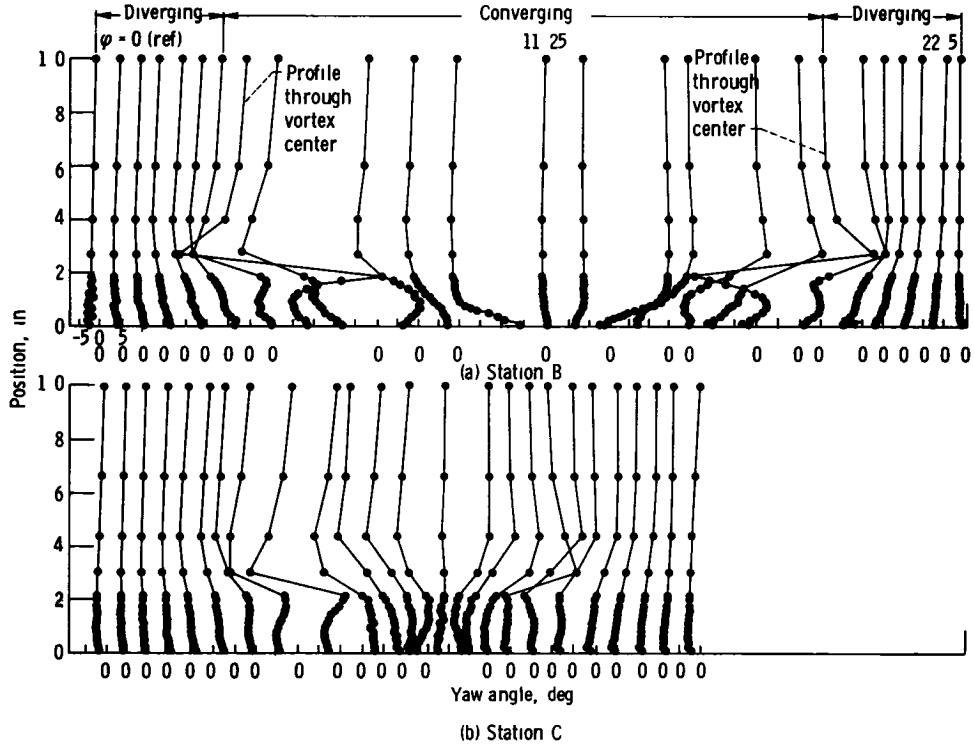

Figure 69 - Hub boundary layer yaw angularity profiles for configuration I vortex generators installed, $\bar{M}_{inlet}$ = 0 29

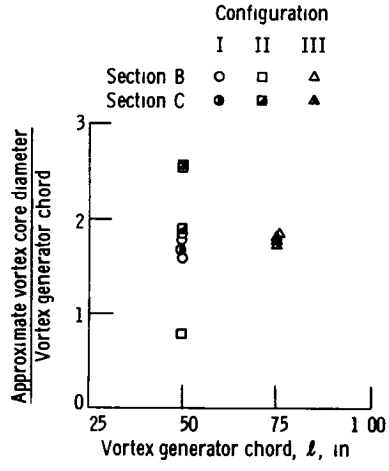

Figure 70 - Approximate vortex core size

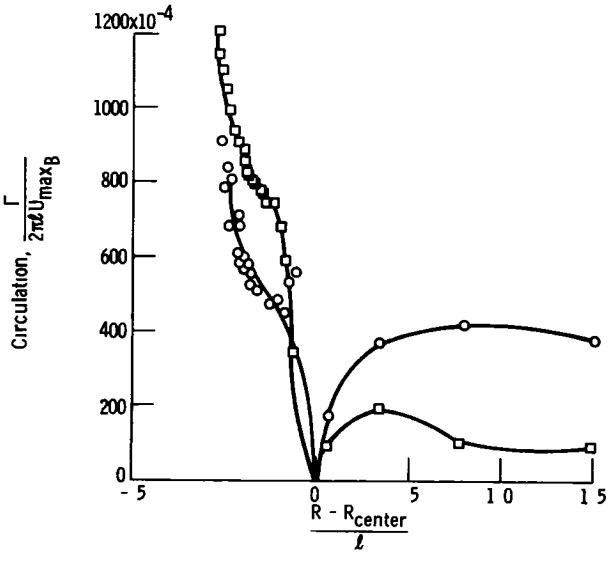

(a) Configuration I

Figure 71 - Vortex strength distribution for station B

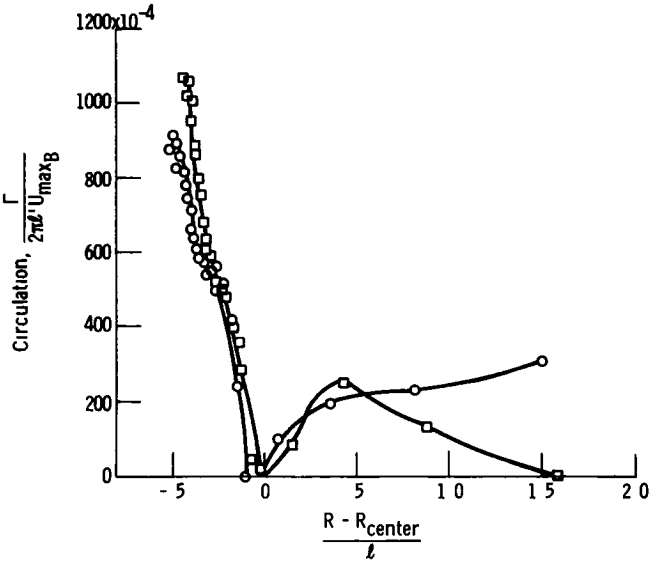

(b) Configuration II

Figure 71 - Continued

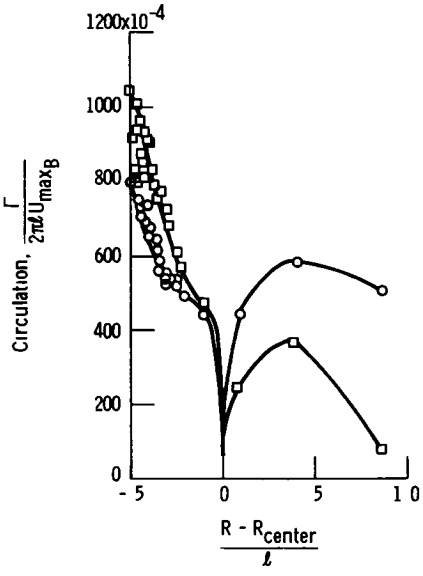

(c) Configuration III

Figure 71 - Concluded

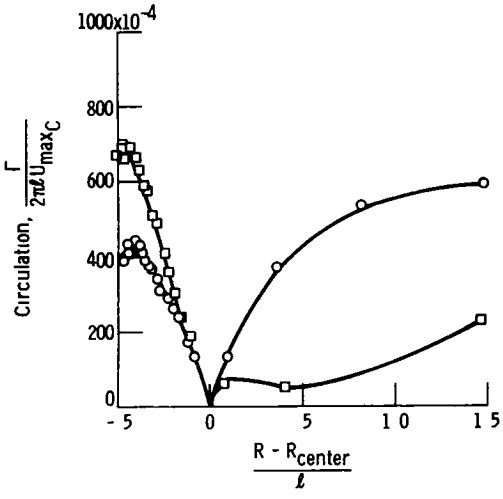

(a) Configuration I

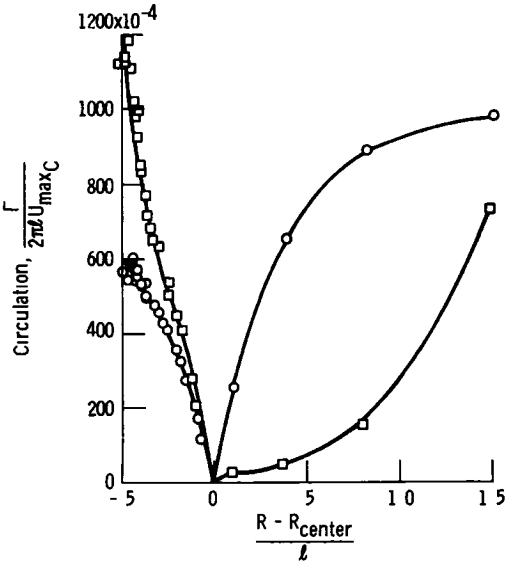

(b) Configuration II

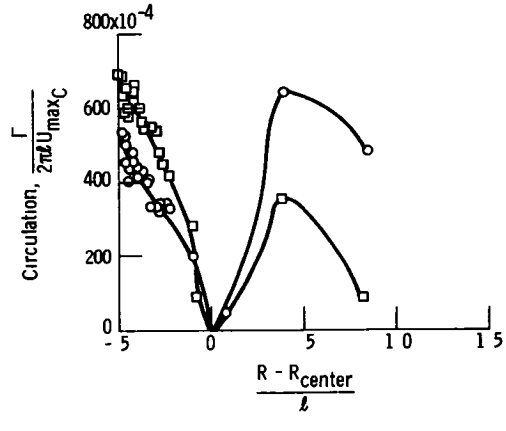

(c) Configuration III

Figure 72. - Vortex strength distribution for station C.

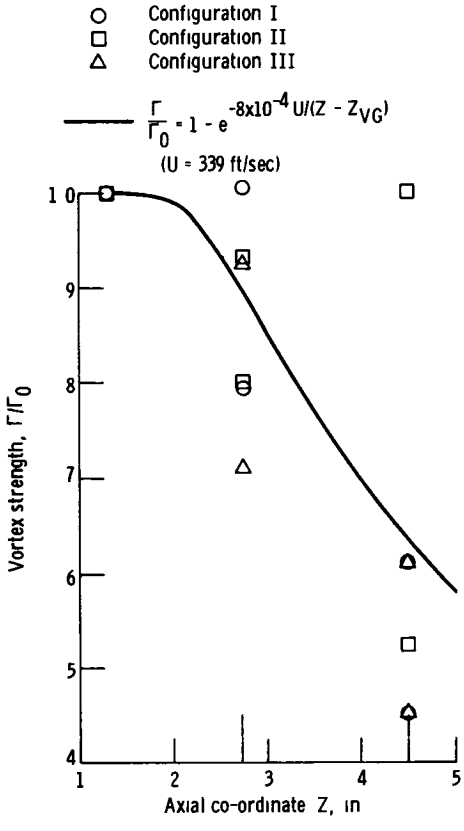

Figure 73 - Axial viscous dissipation of vortex strength

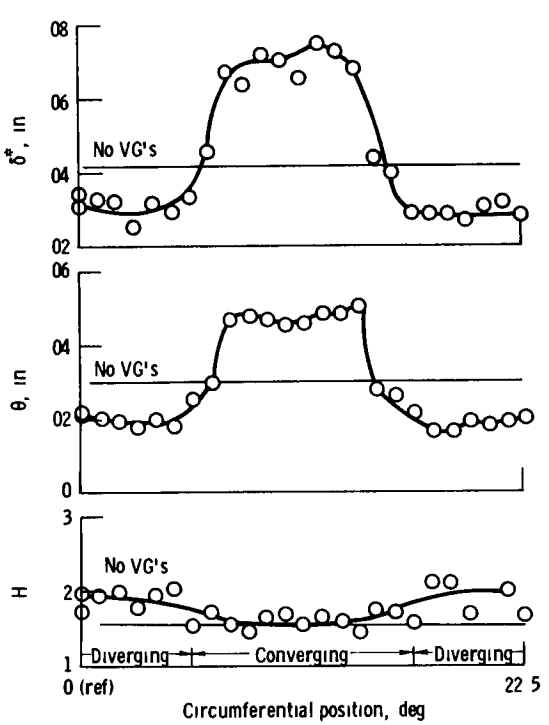

(a) Station B

Figure 74 - Circumferential variation of hub boundary-layer integral properties with configuration I vortex generators installed, $\bar{M}_{inlet} = 0.29$

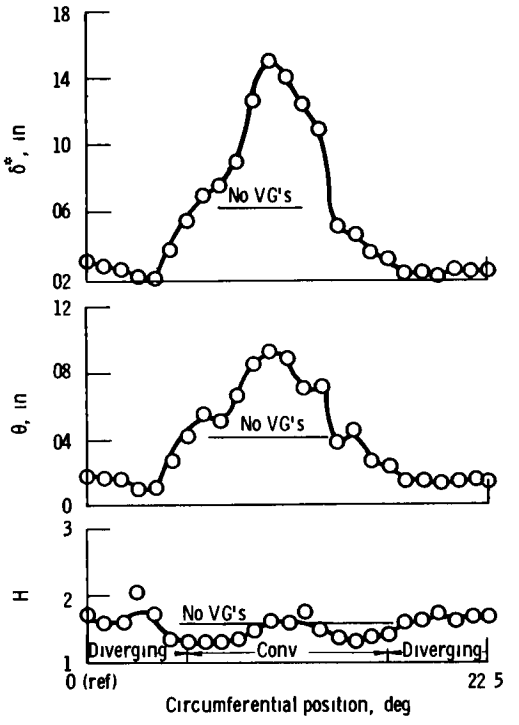

(b) Station C

Figure 74 - Continued

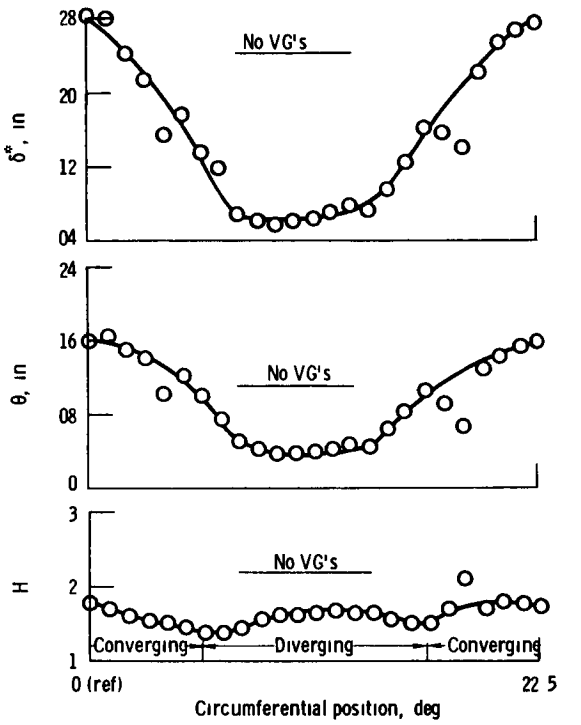

(c) Station D

Figure 74 - Concluded

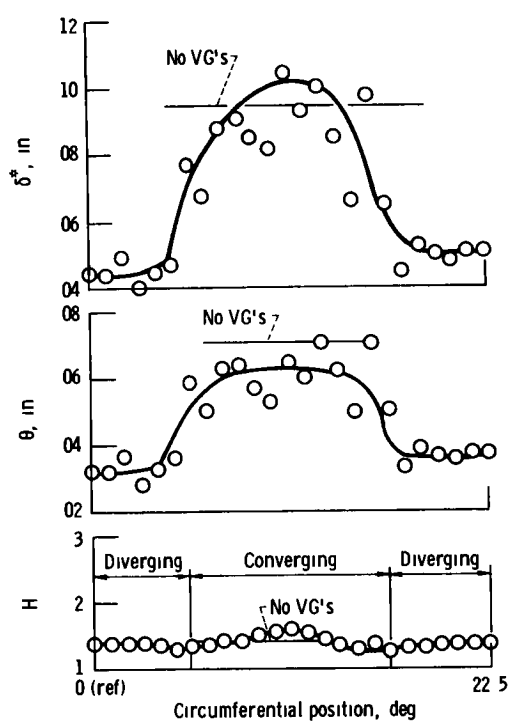

(a) Station B

Figure 75 - Circumferential variation of hub boundary layer integral properties with configuration I vortex generators installed, $\bar{M}_{inlet} = 0.48$

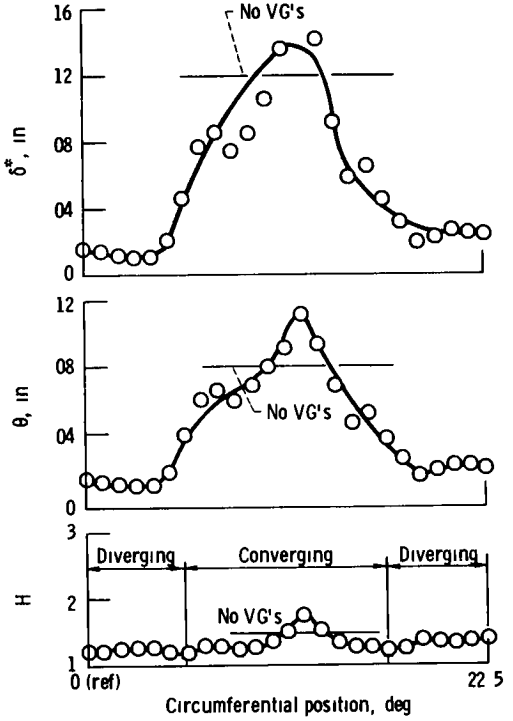

(b) Station C

Figure 75 - Continued

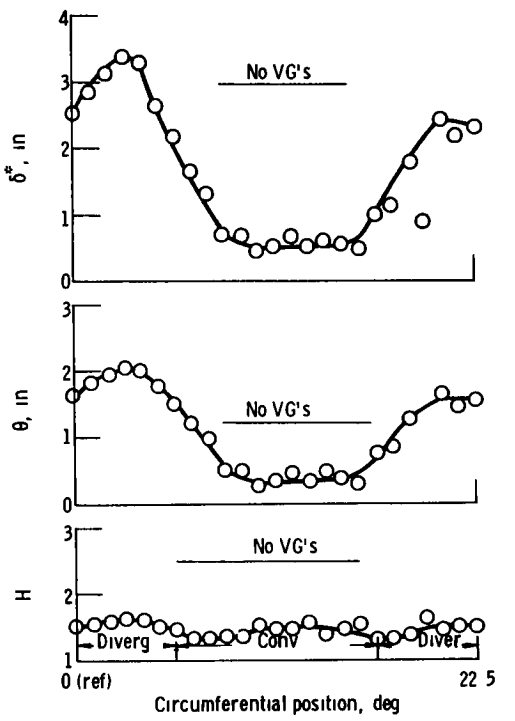

(c) Station D

Figure 75 - Concluded

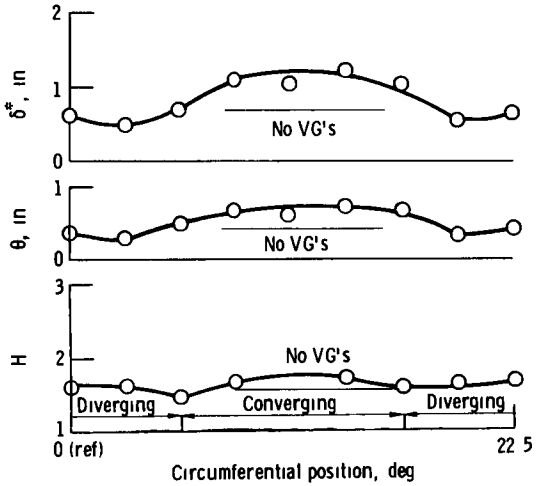

(a) Station B

Figure 76 - Circumferential variation of hub boundary layer properties with configuration I vortex generators installed, $\bar{M}_{inlet}$ = 0 75

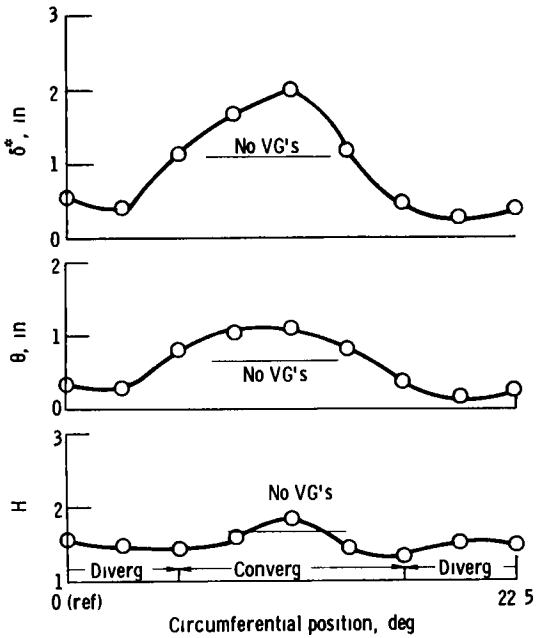

(b) Station C

Figure 76 - Continued

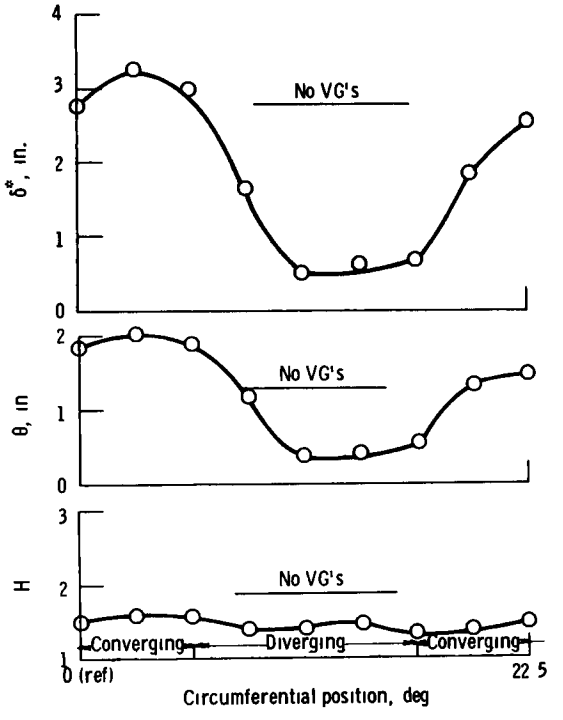

(c) Station D

Figure 76 - Concluded

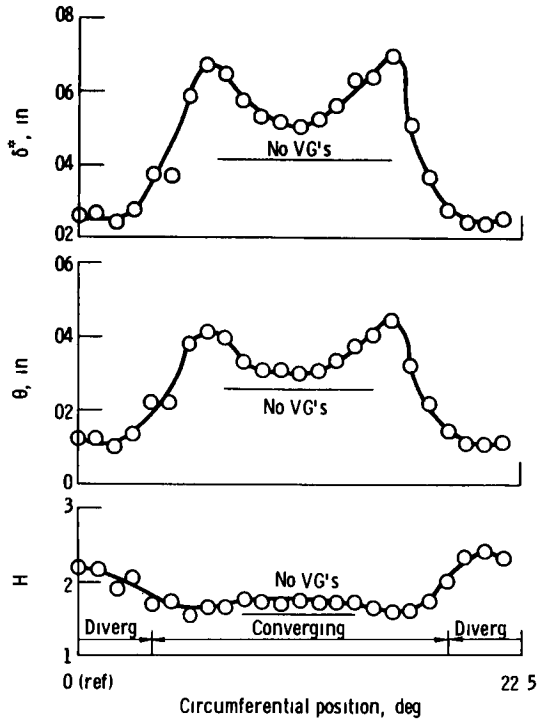

(a) Station B

Figure 77 - Circumferential variation of hub boundary-layer integral properties with configuration II vortex generators installed, $\bar{M}_{inlet} = 0.3$

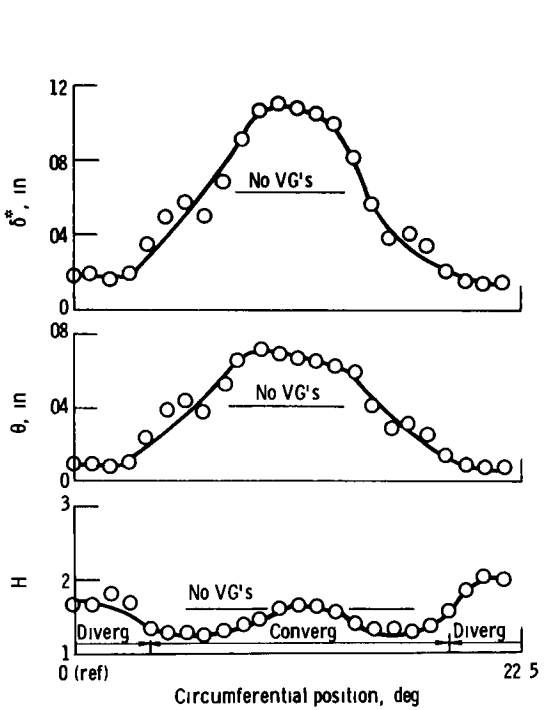

(b) Station C

Figure 77 - Continued

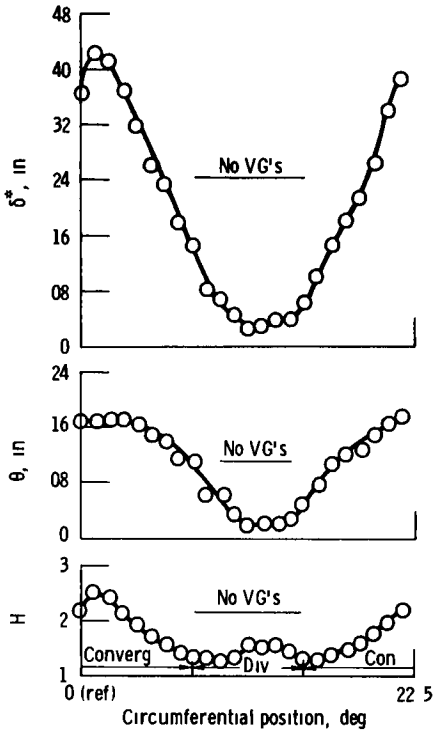

(c) Station D

Figure 77 - Concluded

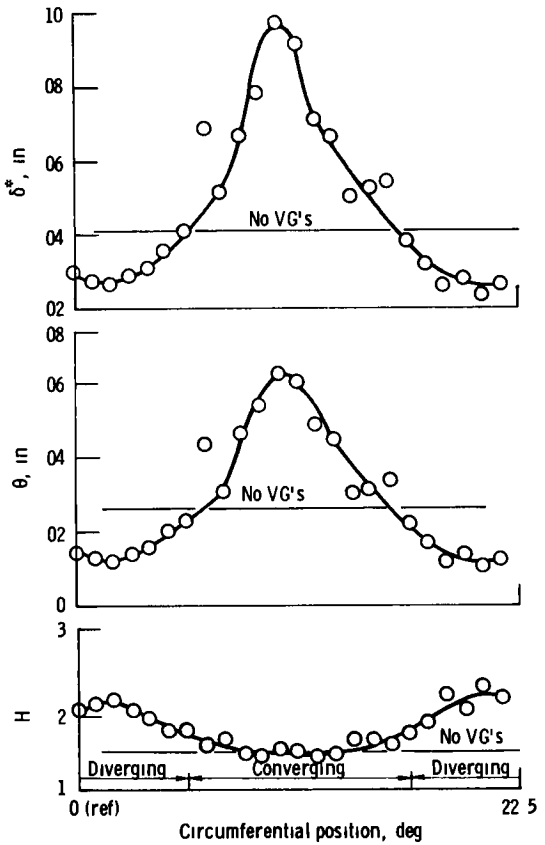

(a) Station B

Figure 78 - Circumferential variation of hub boundary-layer integral properties with configuration III vortex generators installed, $\bar{M}_{inlet}$ = 0 3

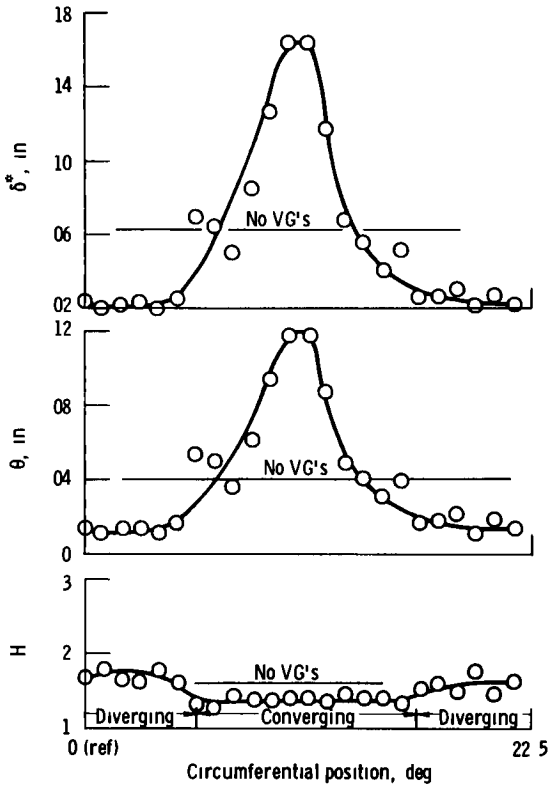

(b) Station C

Figure 78 - Continued

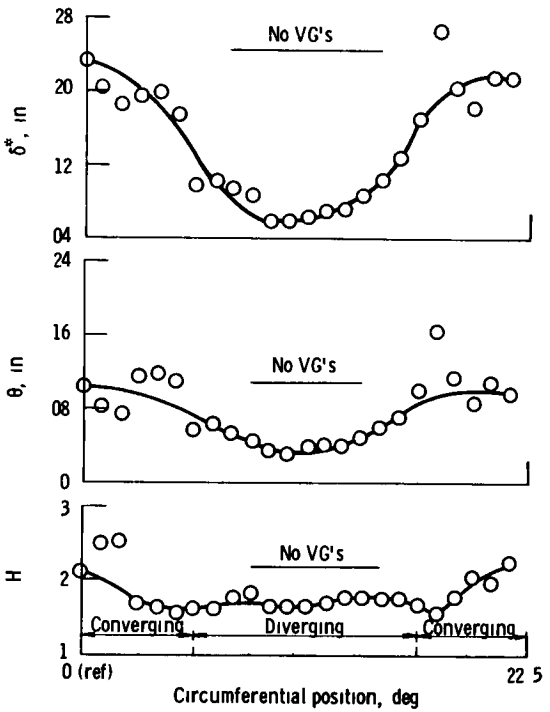

(c) Station D

Figure 78 - Concluded

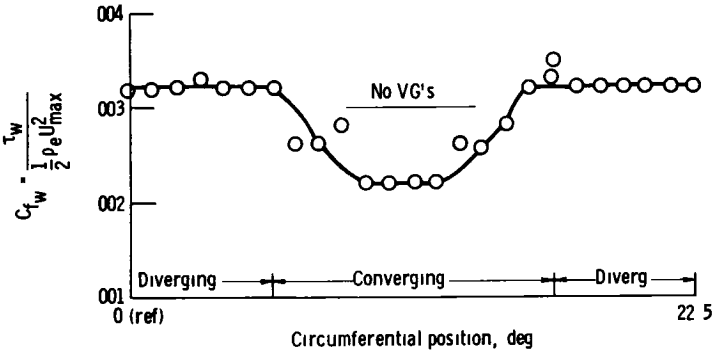

(a) Station B

Figure 79 - Circumferential variation of hub surface skin friction coefficient with configuration I vortex generators installed, $\bar{M}_{inlet} = 0.29$

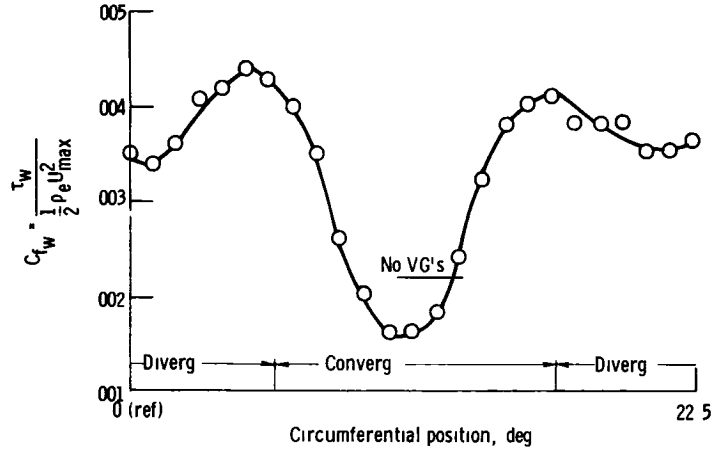

(b) Station C

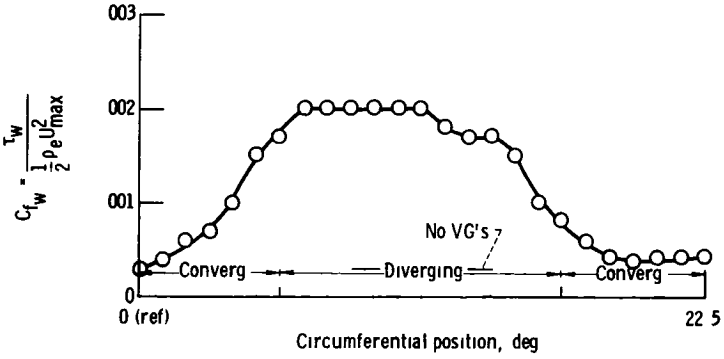

(c) Station D

Figure 79 - Concluded

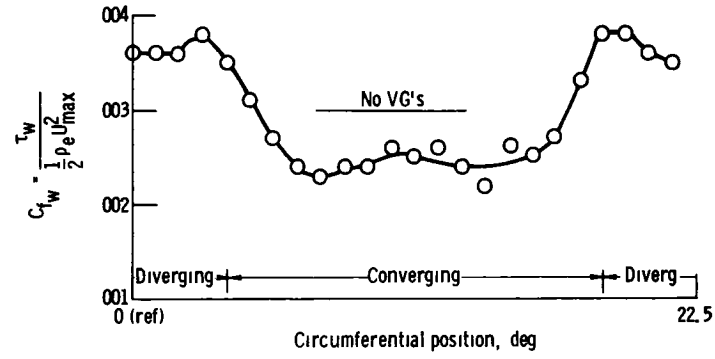

(a) Station B

Figure 80 - Circumferential variation of hub surface skin friction coefficient with configuration II vortex generators installed, $\bar{M}_{inlet} = 0.3$

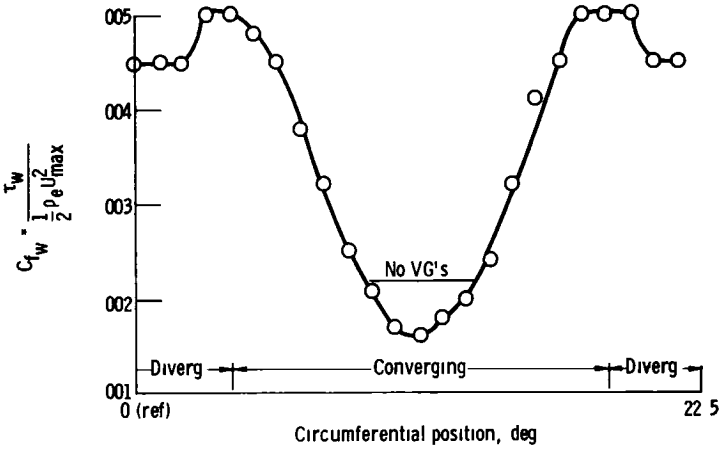

(b) Station C

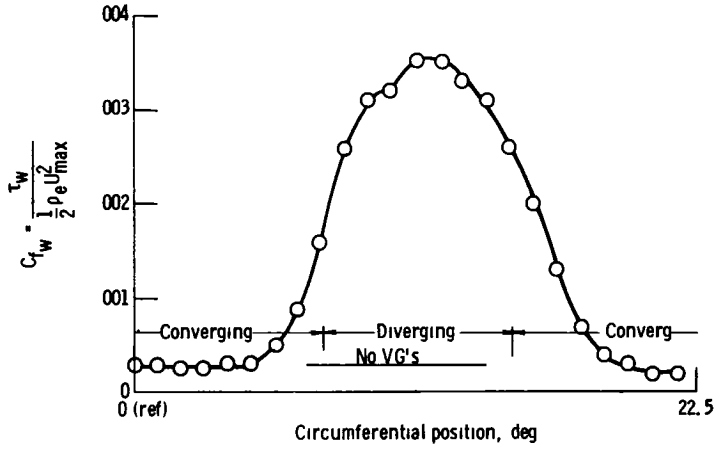

(c) Station D

Figure 80 - Concluded

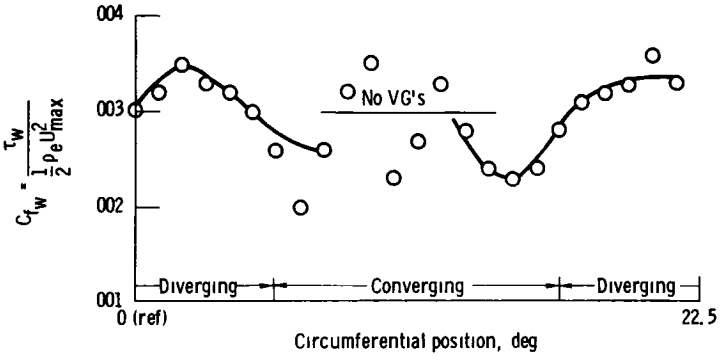

(a) Station B

Figure 81 - Circumferential variation of hub surface skin friction coefficient with configuration III vortex generators installed, $\bar{M}_{inlet} = 0.3$

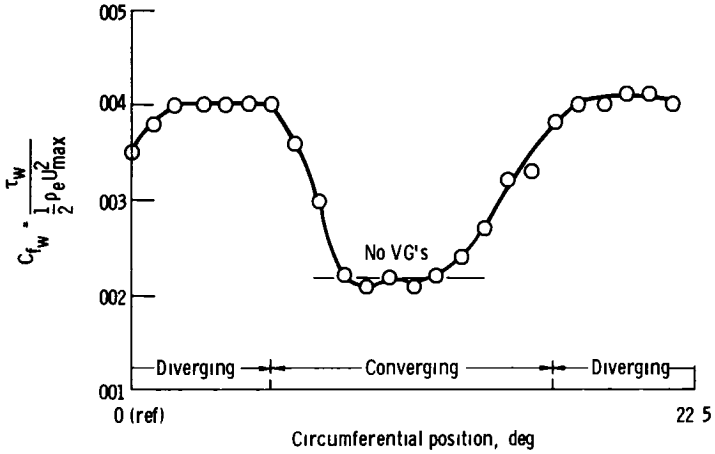

(b) Station C

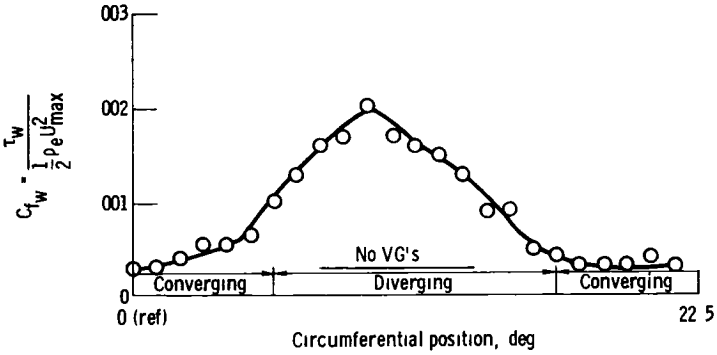

(c) Station D

Figure 81 - Concluded

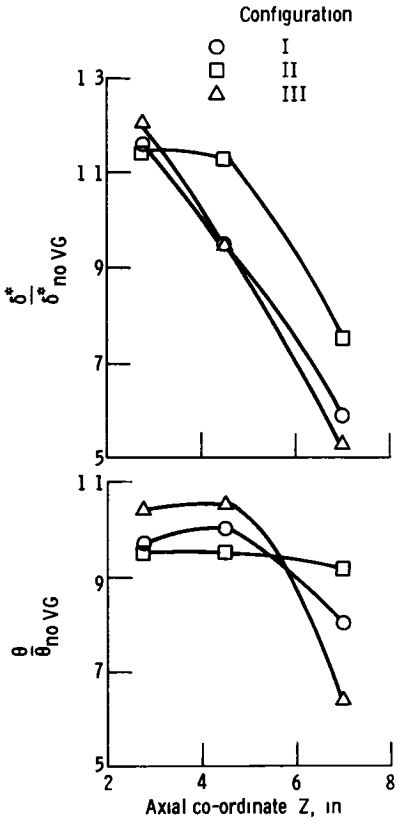

Figure 82 - Average integral thickness variations

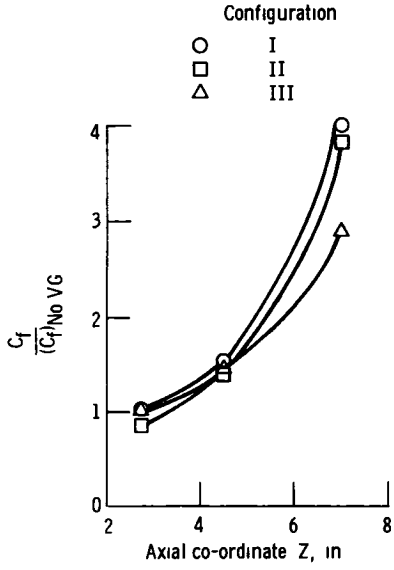

Figure 83 - Average skin friction coefficient variation

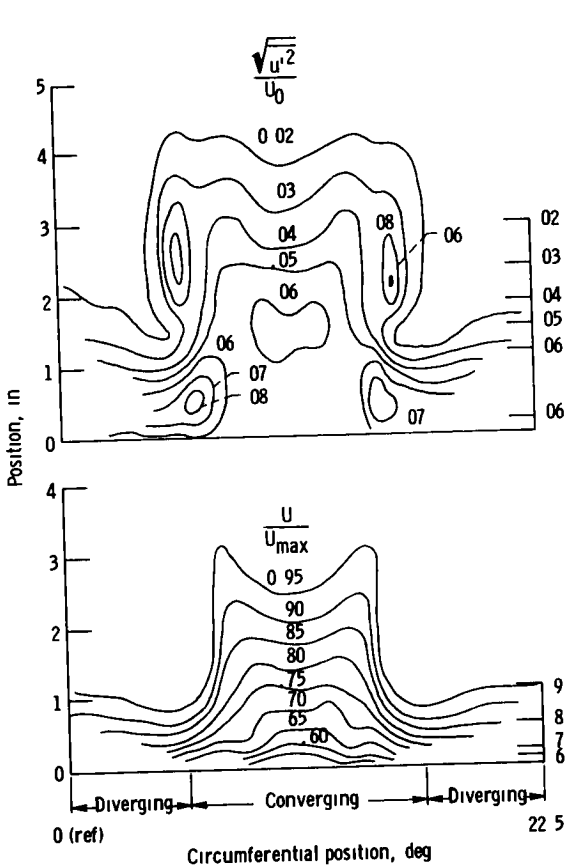

(a) Station B

Figure 84 - Hub boundary layer velocity and axial turbulence intensity contours for configuration I vortex generators installed, $\bar{M}_{inlet} = 0.3$

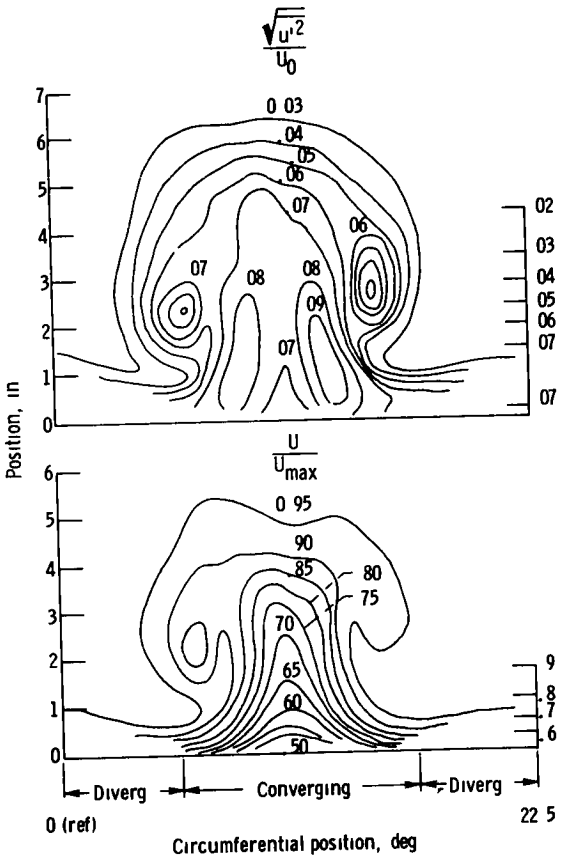

(b) Station C

Figure 84 - Continued

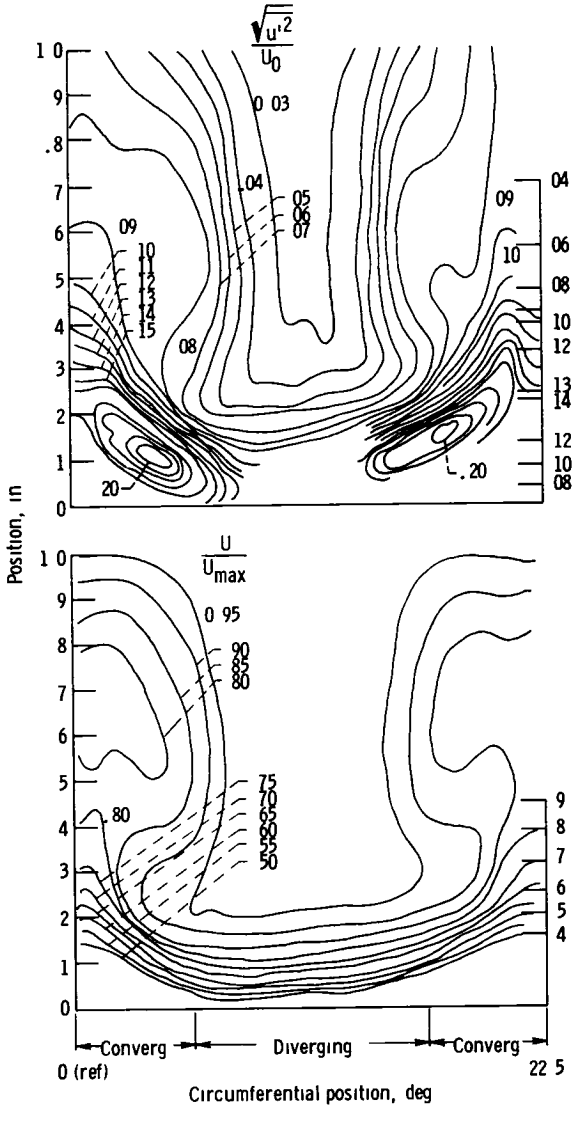

(c) Station D

Figure 84 - Concluded

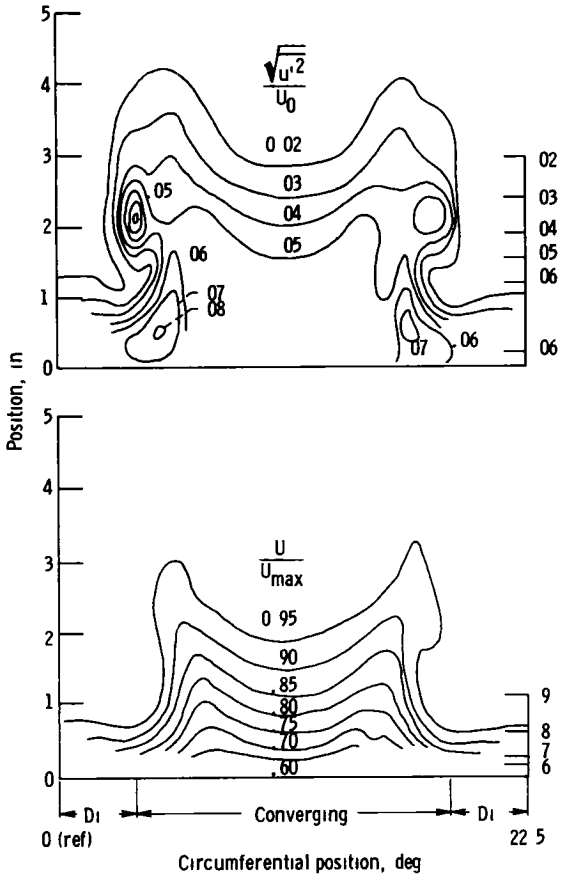

(a) Station B

Figure 85 - Hub boundary layer velocity and axial intensity contours for configuration II vortex generators installed, $\overline{M}_{inlet} = 0.3$

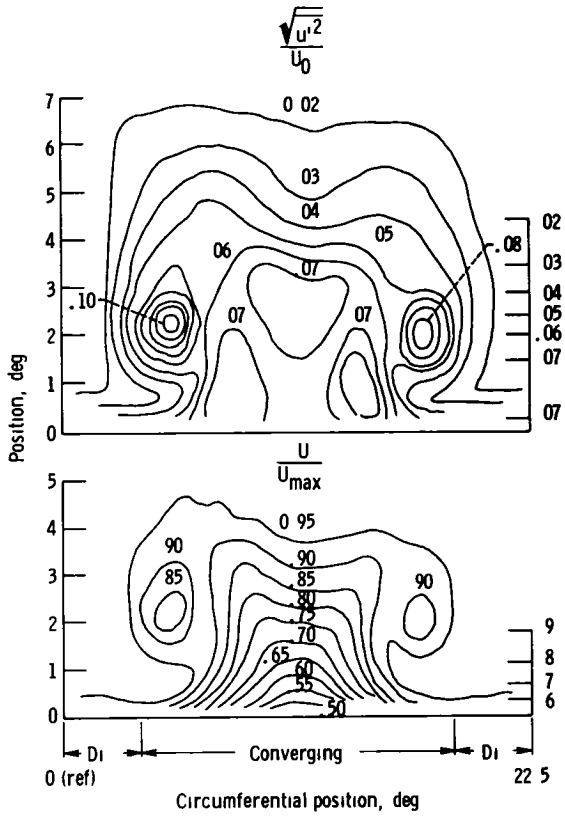

(b) Station C

Figure 85 - Continued

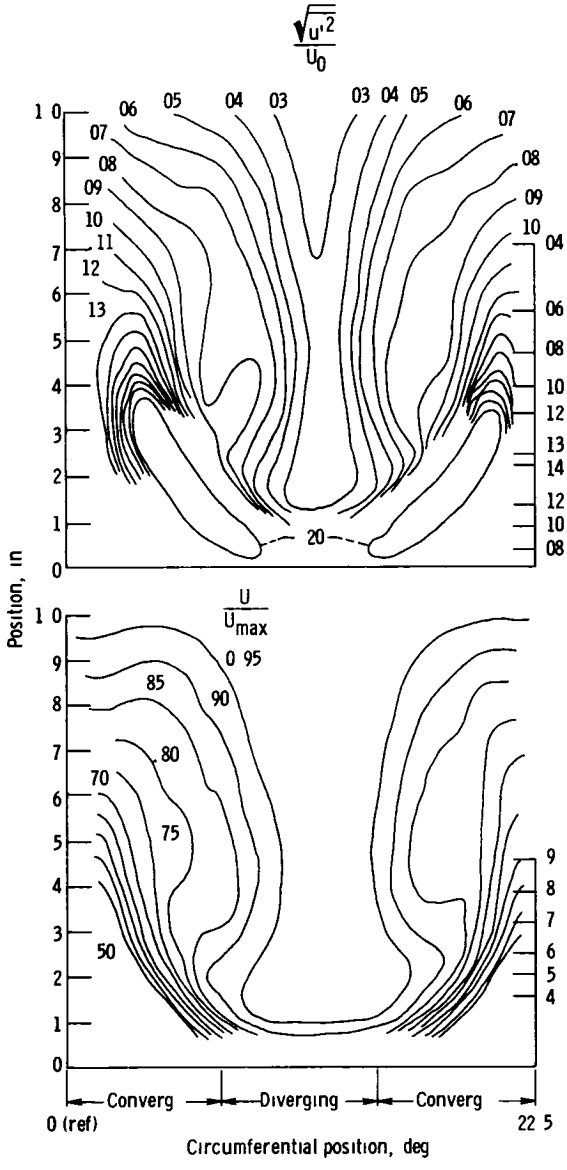

(c) Station D

Figure 85 - Concluded

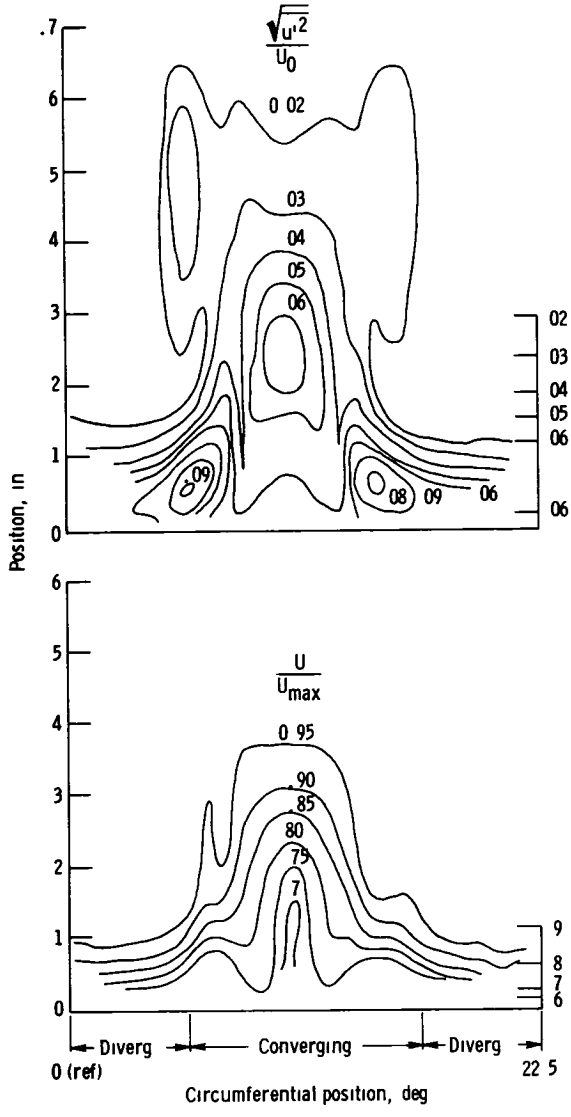

(a) Station B

Figure 86 - Hub boundary layer velocity and axial turbulence intensity contours for configuration III vortex generators installed, $\overline{M}_{inlet} = 0\ 3$

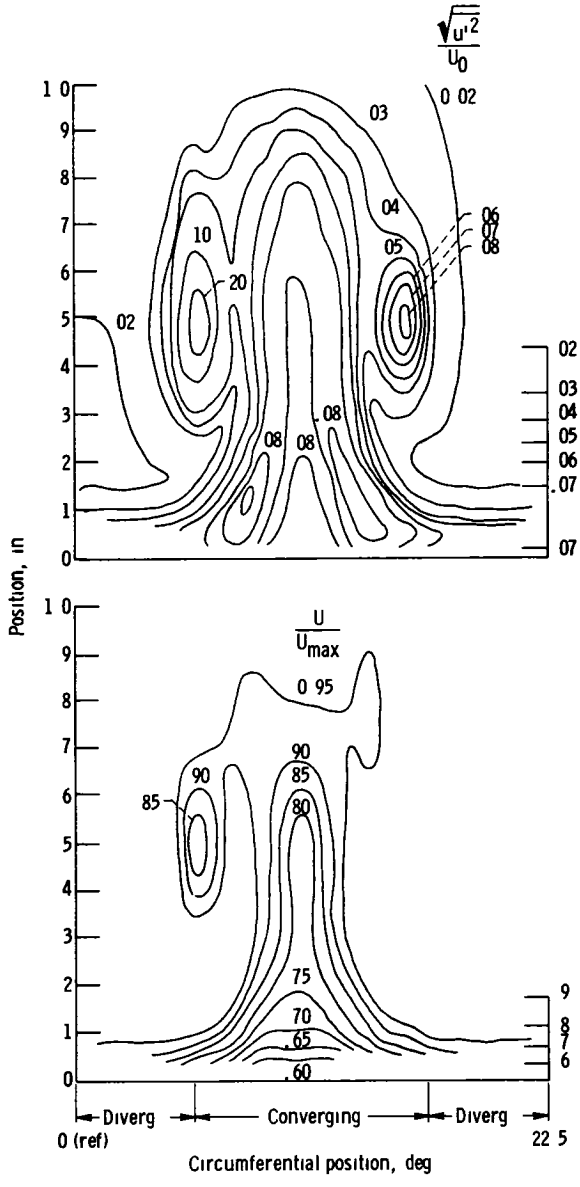

(b) Station C

Figure 86 - Continued

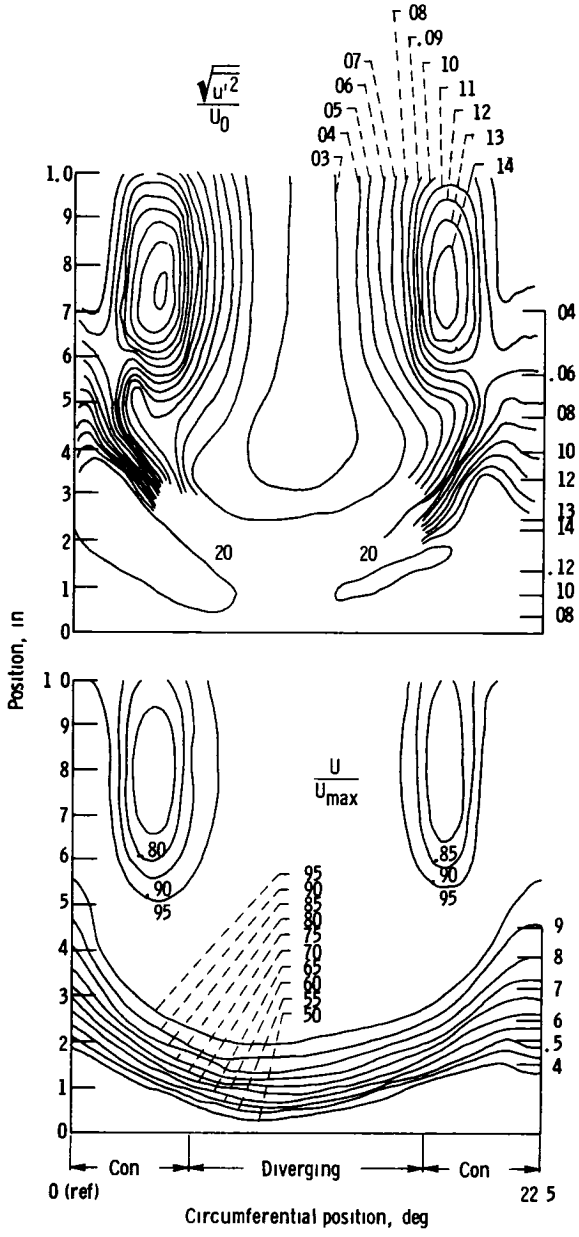

(c) Station D

Figure 86 - Concluded

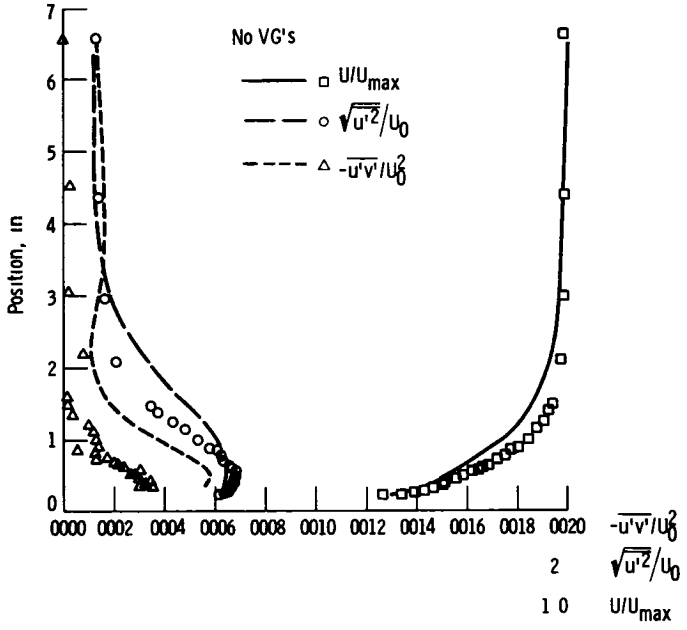

(a) Circumferential position = 0°

Figure 87 - Station B boundary layer profiles for configuration I vortex generators installed, $\bar{M}_{inlet}$ = 0 3

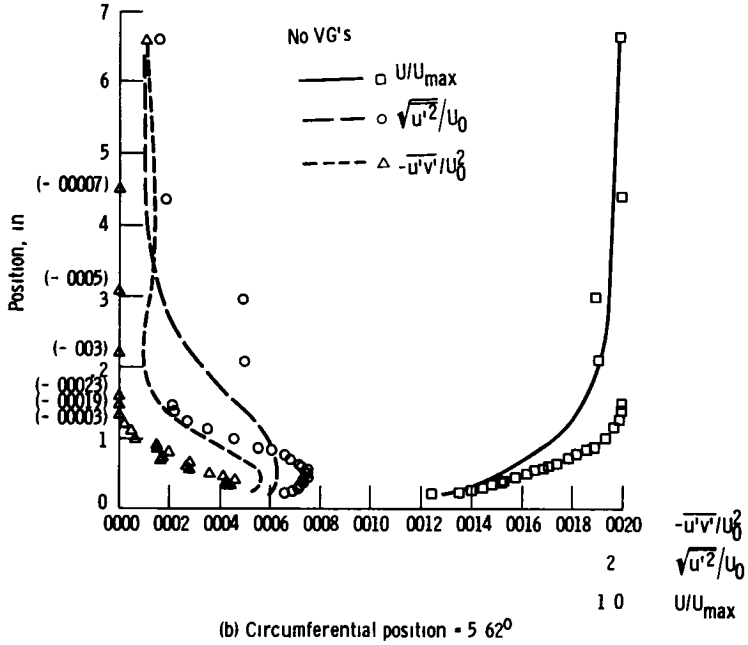

(b) Circumferential position = 5 62°

Figure 87 - Continued

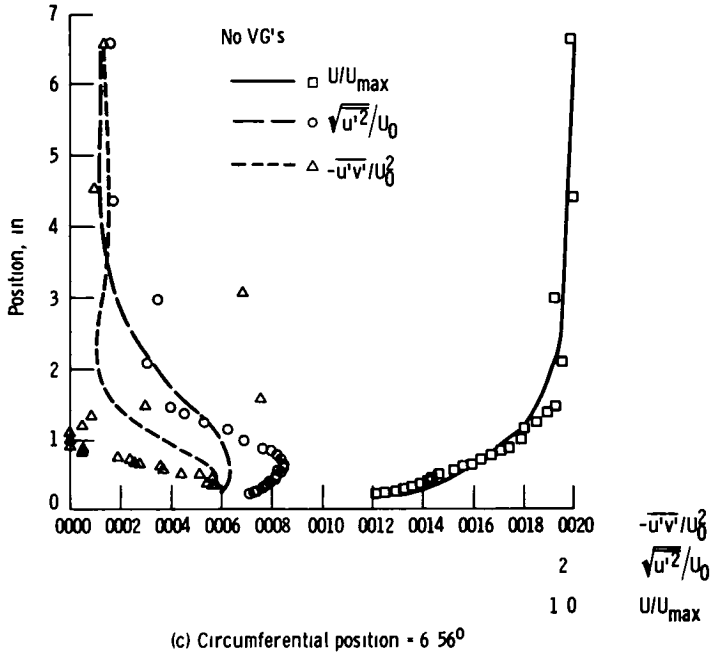

(c) Circumferential position = 6 56°

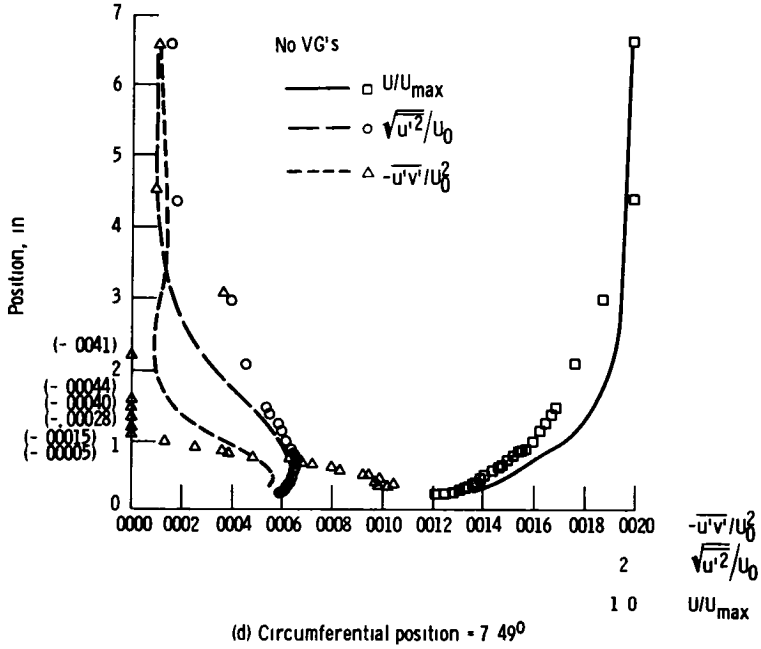

(d) Circumferential position = 7 49°

Figure 87 - Continued

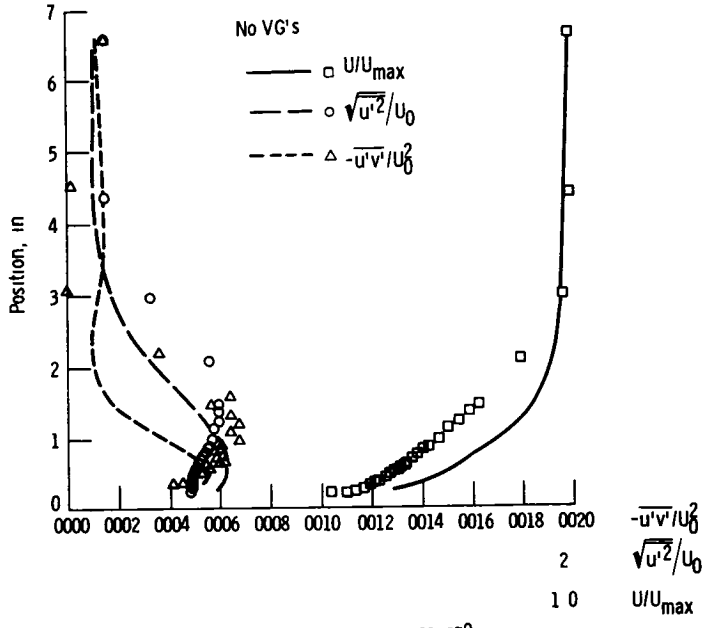

(e) Circumferential position = 11 25°

Figure 87 - Concluded

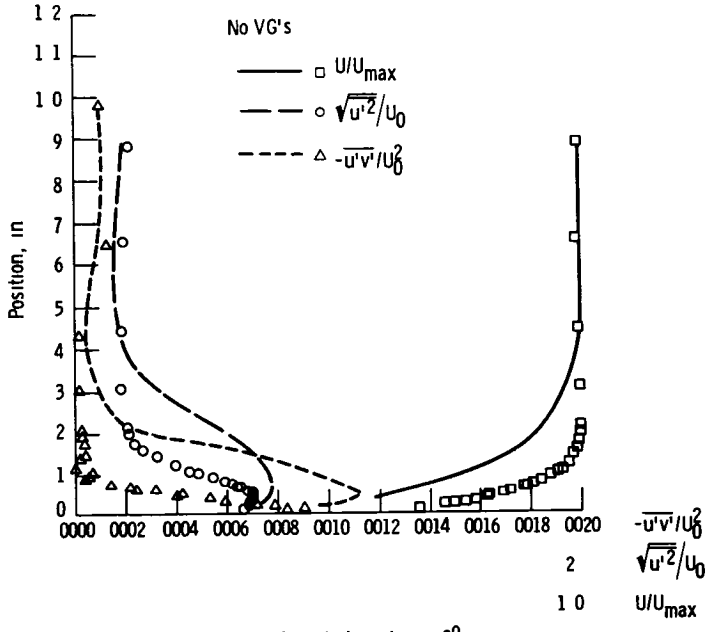

(a) Circumferential position = 0°

Figure 88 - Station C boundary layer profiles for configuration I vortex generators installed, $\bar{M}_{inlet}$ = 0 3

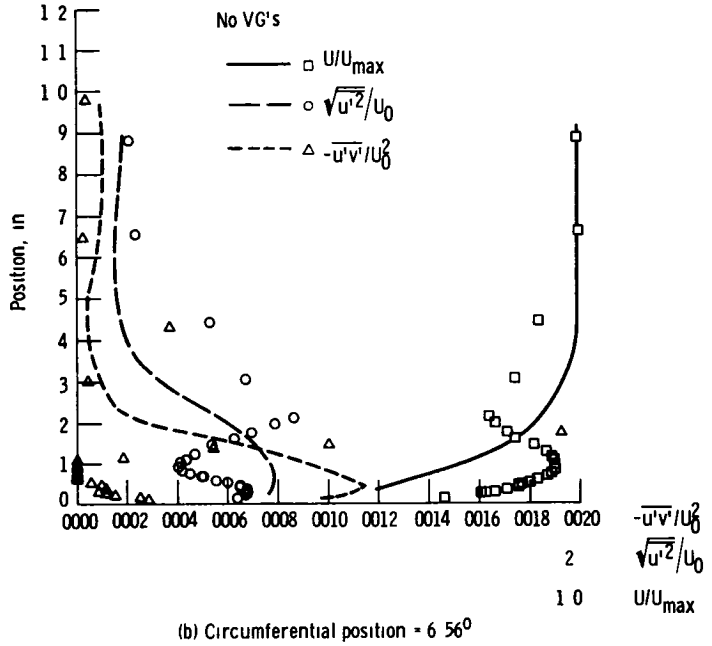

(b) Circumferential position = 6 56°

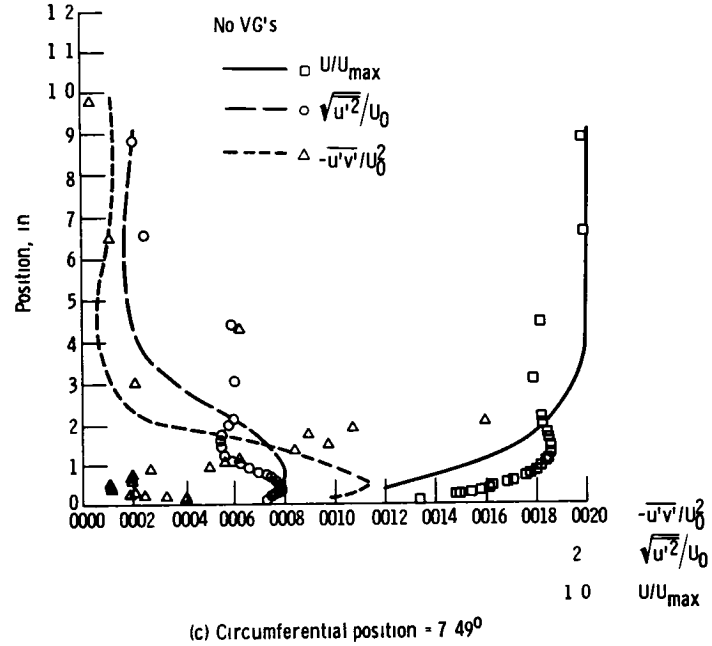

(c) Circumferential position = 7 49°

Figure 88 - Continued

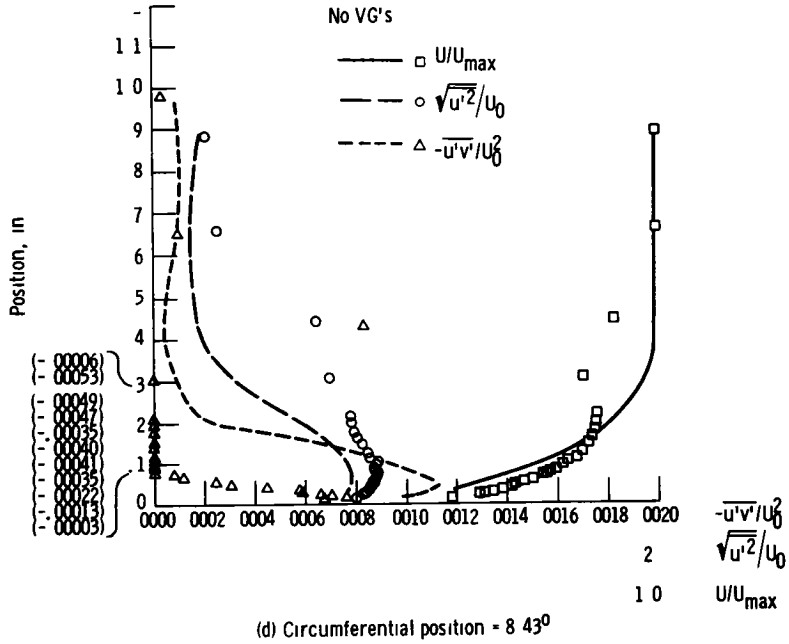

(d) Circumferential position = 8 43°

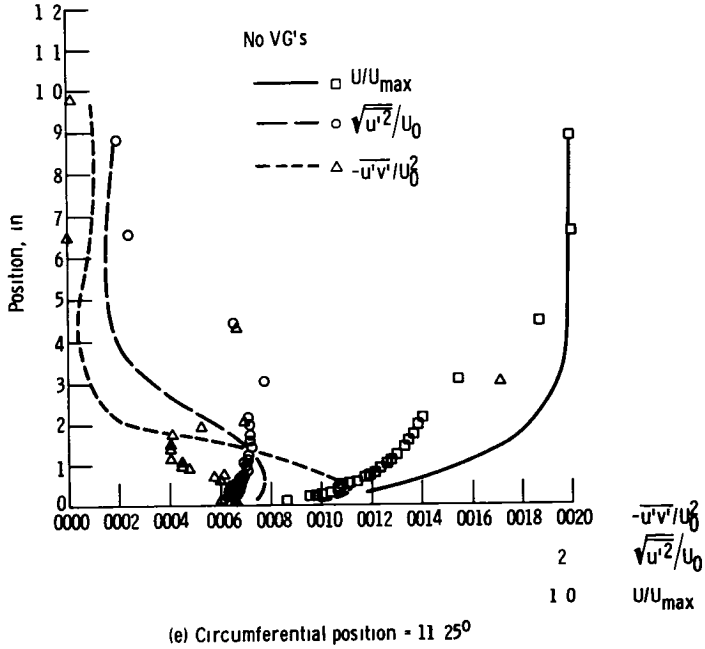

(e) Circumferential position = 11 25°

Figure 88 - Concluded

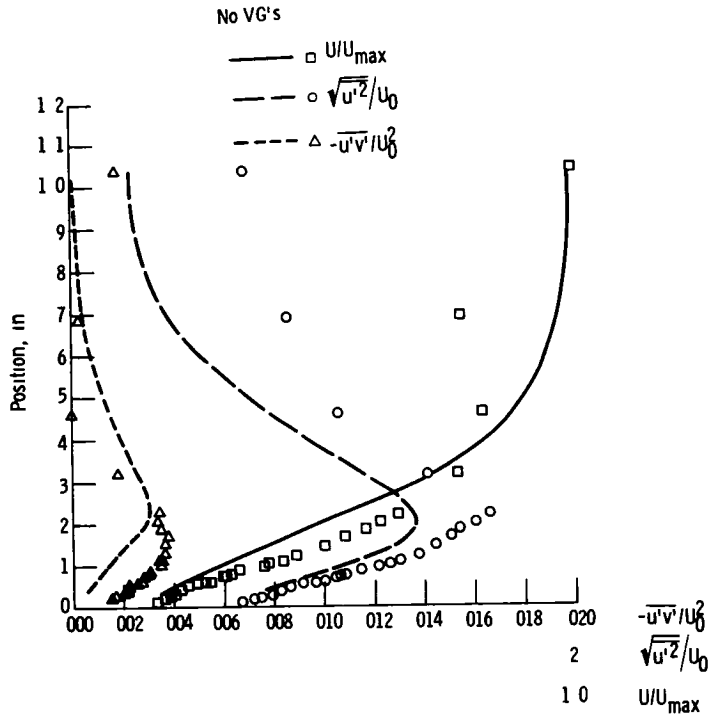

(a) Circumferential position = 0°

Figure 89 - Station D boundary layer profiles for configuration I vortex generators installed, $\bar{M}_{inlet}$ = 0 3

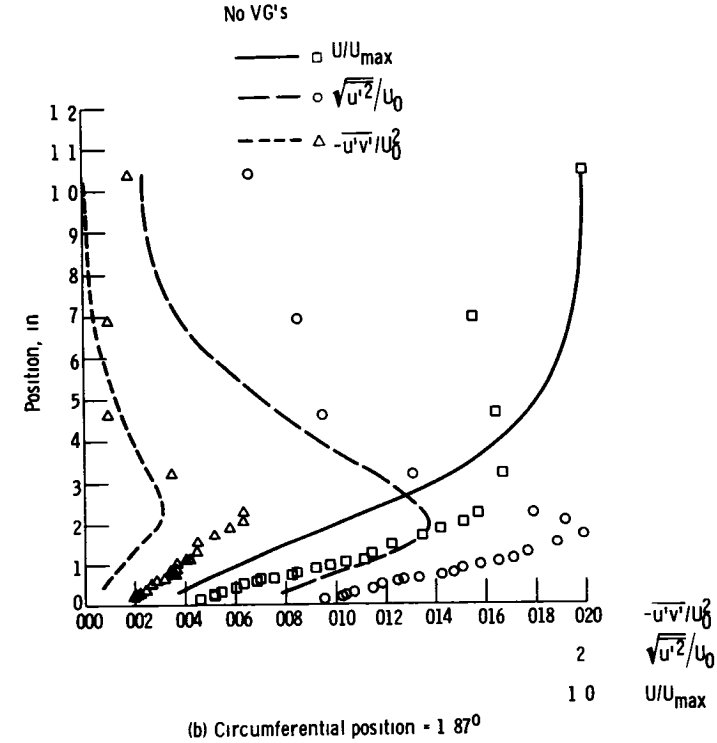

(b) Circumferential position = 1 87°

Figure 89 - Continued

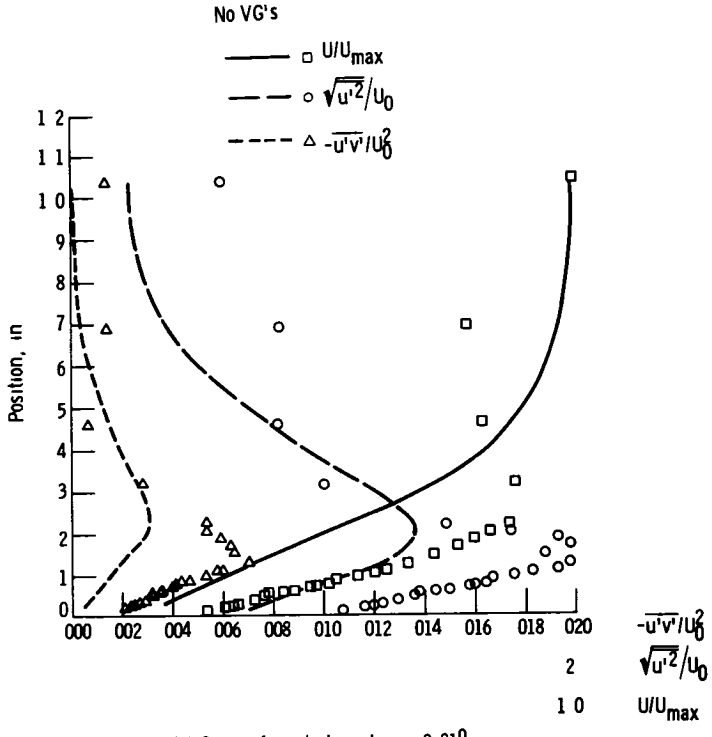

(c) Circumferential position = 2 81°

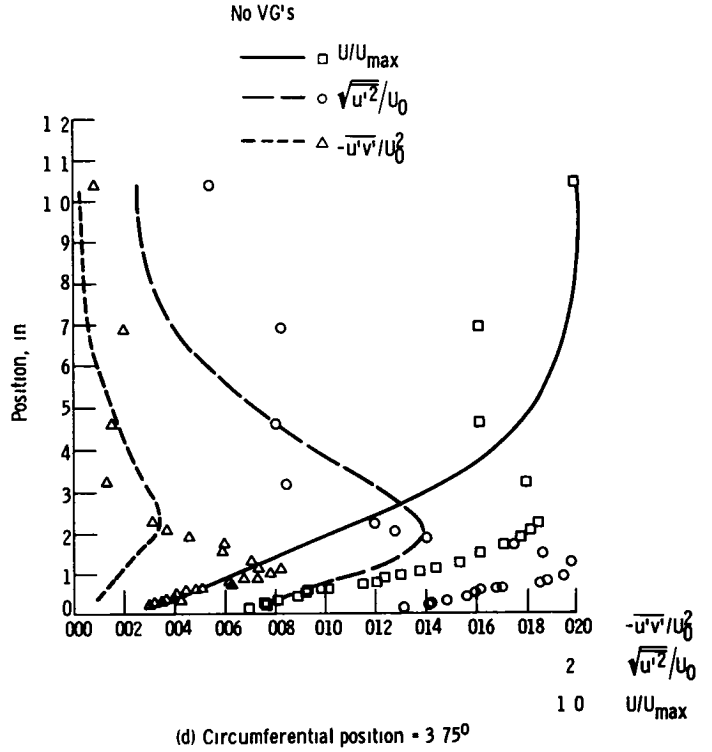

(d) Circumferential position = 3 75°

Figure 89 - Continued

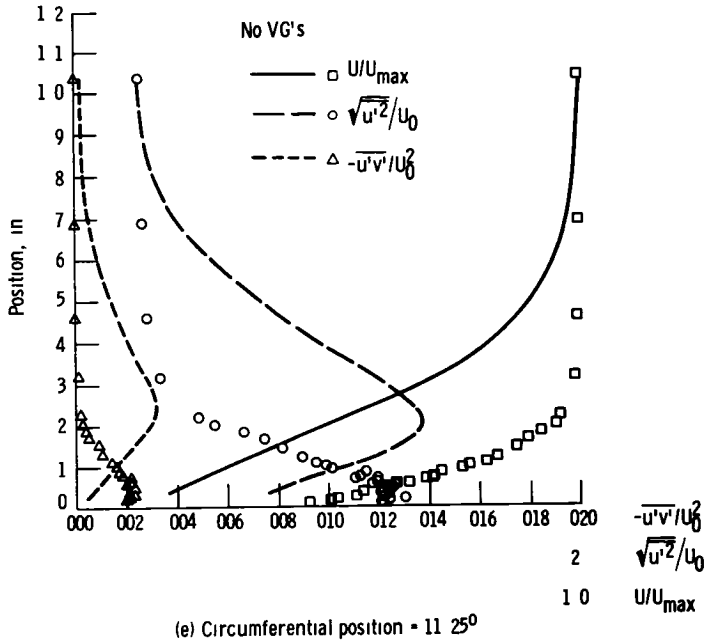

(e) Circumferential position = 11 25°

Figure 89 - Concluded

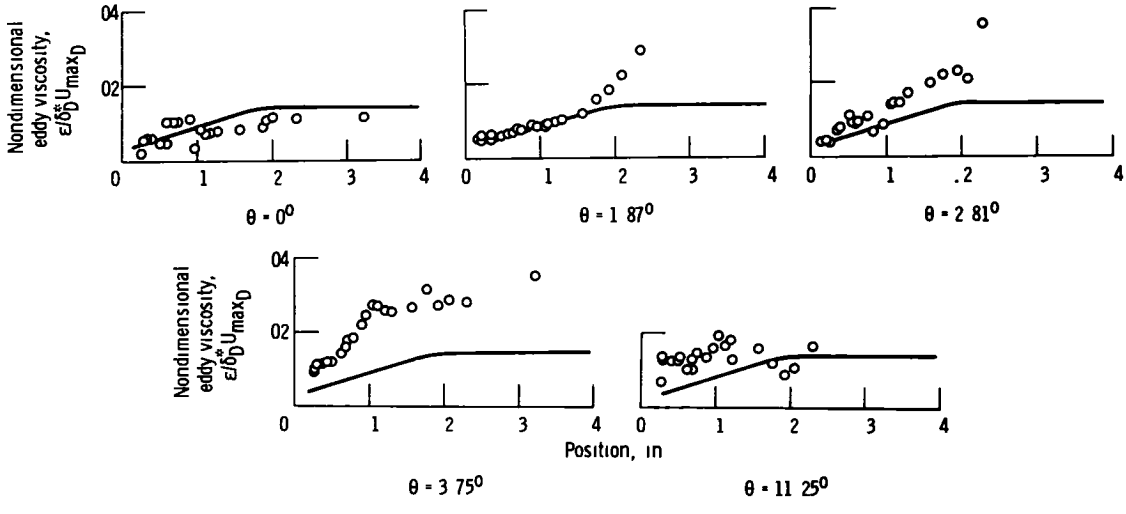

(a) Configuration I

Figure 90 - Nondimensional eddy viscosity distributions for station D

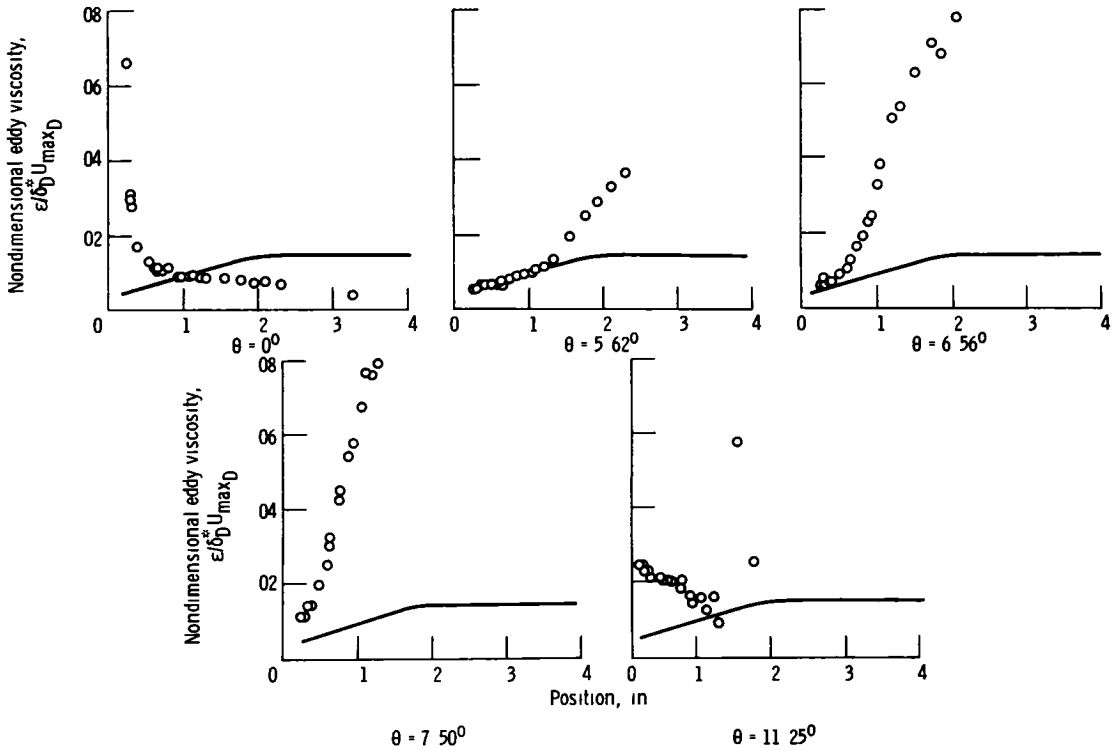

(b) Configuration II

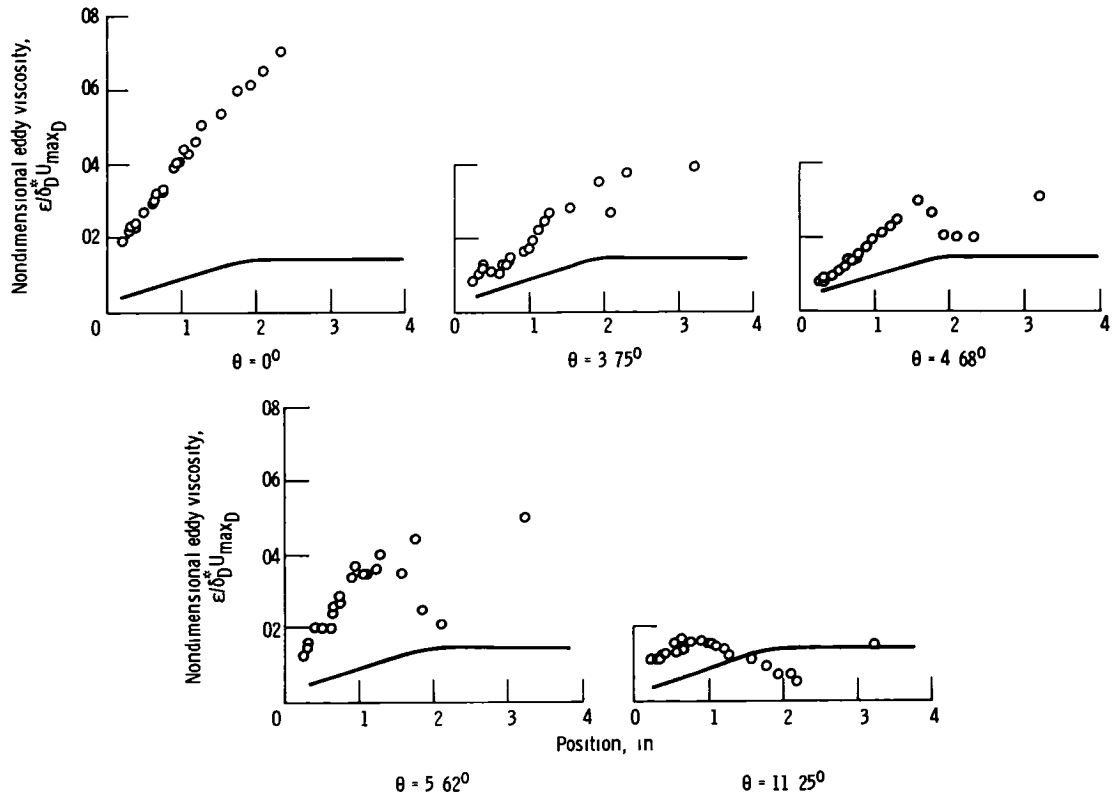

(c) Configuration III

Figure 90 - Concluded

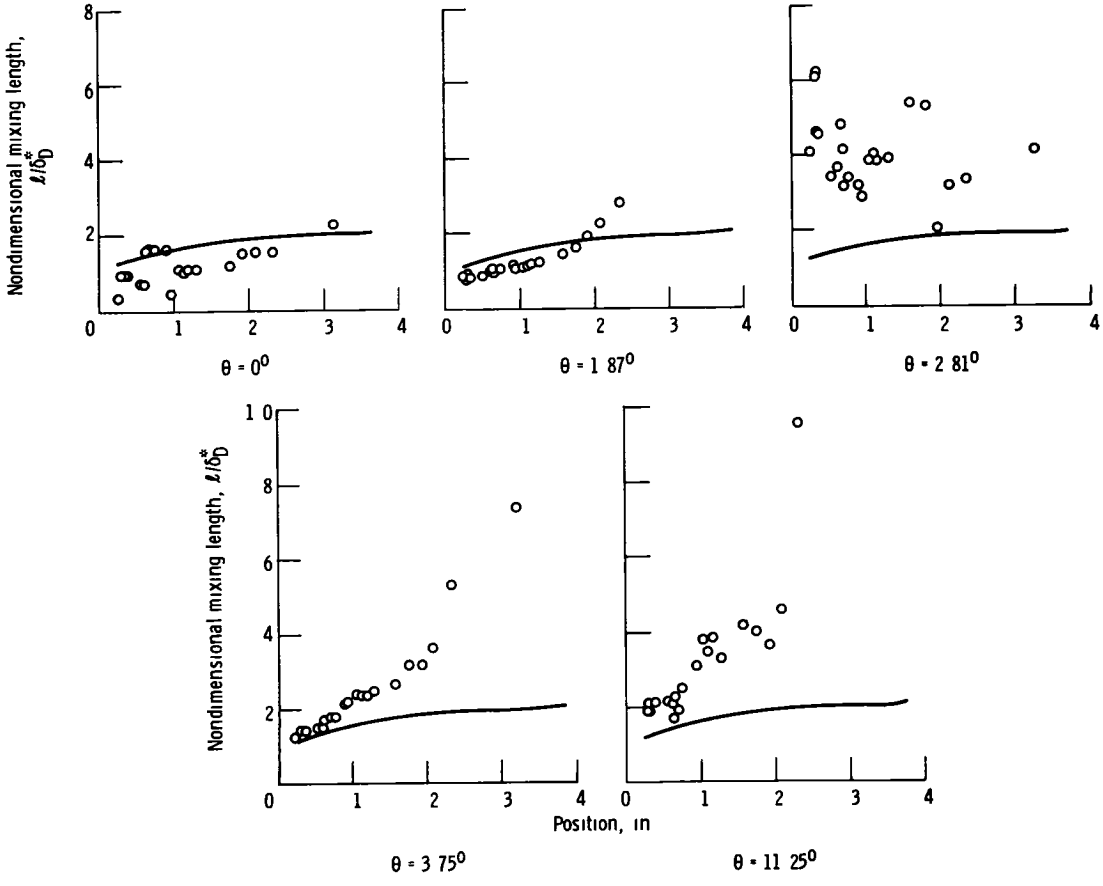

(a) Configuration I

Figure 91 - Nondimensional mixing length distributions for station D

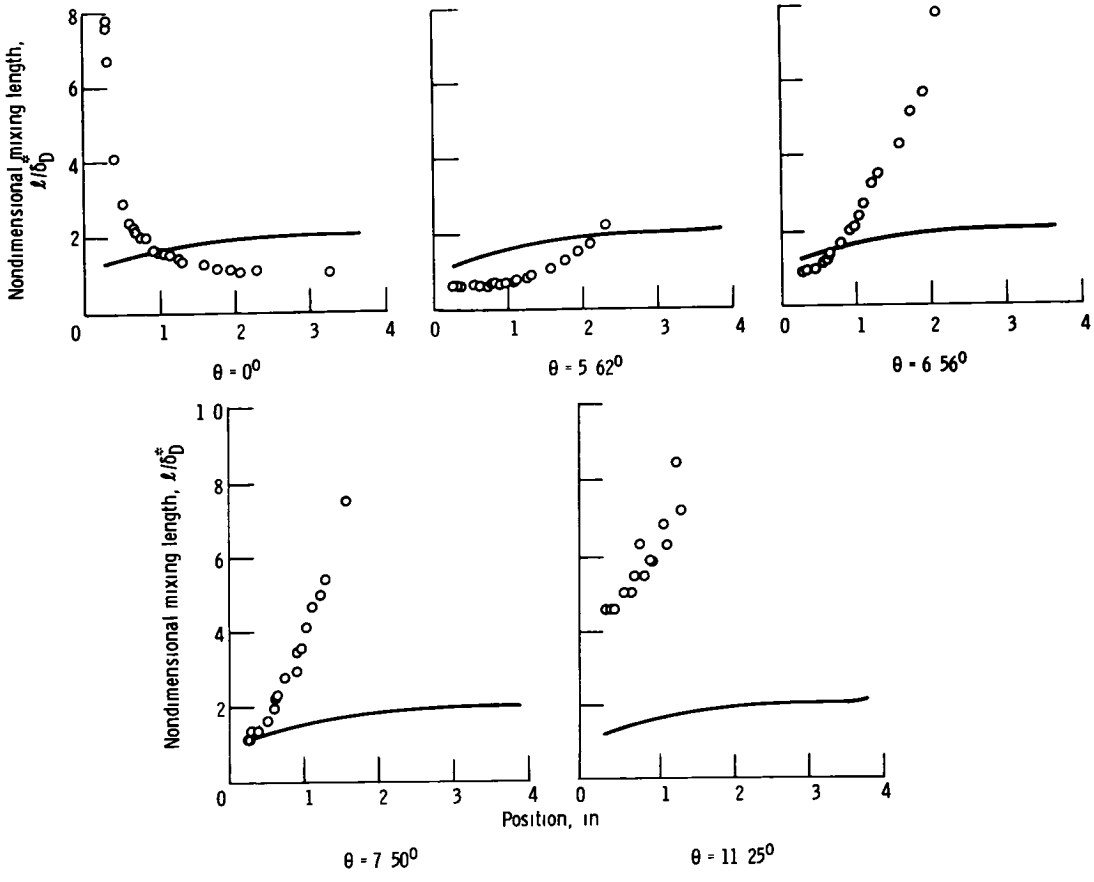

(b) Configuration II

Figure 91 - Continued

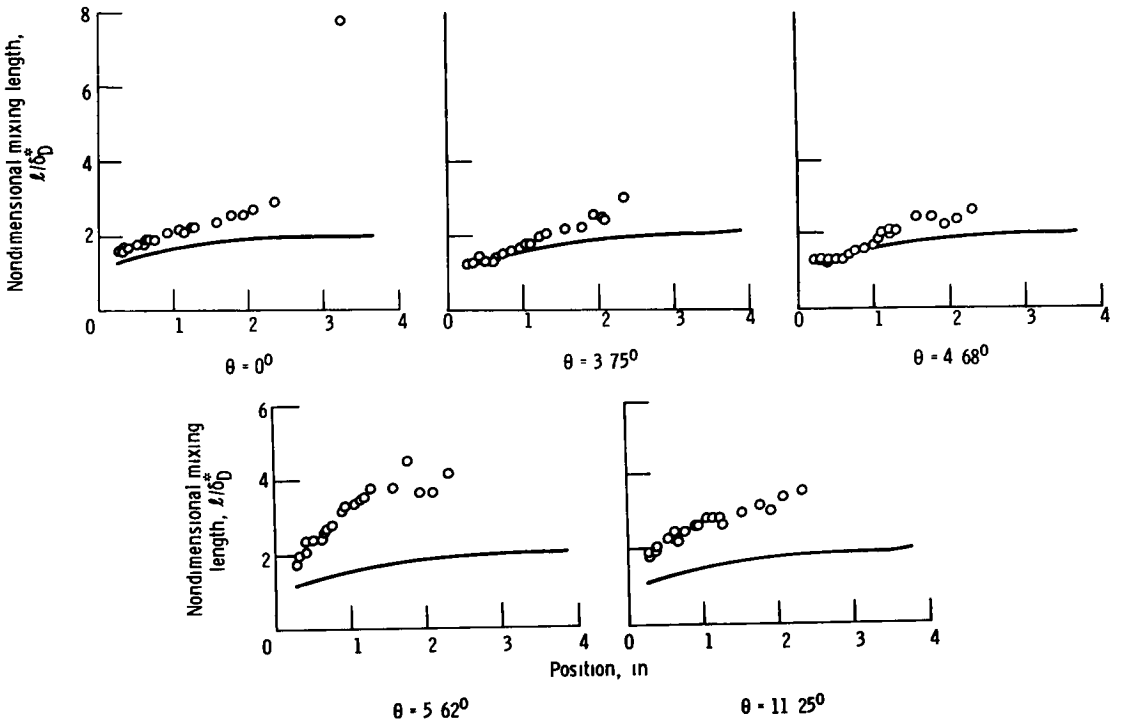

(c) Configuration III

Figure 91 - Concluded

CHAPTER V

SUMMARY AND CONCLUSIONS

The primary objective of the research program discussed herein was to investigate the physical details of the forced mixing process of a boundary layer in an axisymmetric annular diffuser using conventional wing like vortex generators as the forced mixing device. The diffuser chosen for this study was a constant Mach number gradient design which is typical of diffusers currently used in supersonic aircraft propulsion systems.

Detailed flow field measurements were made at four axial locations downstream of the vortex generators. At each axial location, a total of 25 equally spaced profiles were measured behind three consecutive vortex generators which formed two pairs of vortex generators.

Measurements were made in two phases. Initially total pressure rakes as well as radially traversing boundary layer total pressure probes were installed at each station, and measurements were made throughout the inlet Mach number range of 0.1 to 0.9. In addition, yaw angle distribution measurements were made at the first two stations downstream of the vortex generators.

The second phase involved replacing the total pressure rakes and probes with hot film anemometry probes to define the boundary layer turbulence structures at the same locations which the pressure measurements were made. Both single and cross film probes were used to measure mean velocity, axial turbulence intensity, and Reynolds shear stress profiles.

The diffuser turbulence data was taken only for a nominal inlet Mach number of 0.3. The inlet Mach number was purposely kept low to avoid compressibility problems which plague hot wire and hot film sensors.

Three different vortex generator configurations were tested. The baseline configuration I had evenly spaced vortex generators with a height of 0.25 inch and an aspect ratio of 0.5 (height/chord). The second configuration II had vortex generators with the same geometric properties as did configuration I but the spacing of adjacent vortex generators which comprise two pairs were not equal. The third configuration III was an increased size version of configuration I with a height of 0.375 inch.

All three vortex generator configurations tested provided increases in diffuser performance over the respective levels measured with no vortex generators installed. Increases in diffuser exit total pressure recovery were as much as 0.5 percent at the higher inlet Mach numbers. Diffuser exit static pressure coefficient increases of 0.1 were noted for all inlet Mach numbers. Diffuser exit total pressure distortion levels were reduced by as much as 2 to 3 percent at the higher inlet Mach numbers.

The differences in performance achieved by the three configurations were less marked.

For all three vortex generator configurations tested, the hub surface boundary layer was still separated at the diffuser exit station although the inclusion of the vortex generators did reduce the height of the separated zone by about 50 percent. The hub boundary layer separation at the diffuser exit station with vortex generators installed was expected as the hub surface had a discontinuity in slope at the diffuser exit station. This was peculiar to the experimental hardware design and not illustrative of an actual flight design.

The measured shed vortex core sizes were found to be about 0.2 times the vortex generator chord, a result which agreed with measured core sizes of vortices shed from wings installed in wind tunnels.

Vortex paths agreed qualitatively in lateral spacing variation with simplified potential flow path prediction analyses; however, the variation in height of the vortex axes above the hub surface did not agree with the predictions.

Vortex strength was correlated with axial location through the relation that $\Gamma/\Gamma_0 = 1 - e^{-0.0008/z-z_{VG}}$ which indicates that the effectiveness of the vortices a forced mixers was severely limited at the diffuser exit station ($\Gamma/\Gamma_0 = 0.34$ at the diffuser exit station).

Boundary layer profiles measured downstream of the vortex generators indicated that the hub boundary layer retained the asymmetry imparted by the forced mixing to the diffuser exit station. For all three configurations tested, the profiles indicated the mixing action intensified as the boundary layer flow proceeded downstream.

Distinct differences in boundary layer integral properties and skin friction levels were noted as a function of vortex generator spacing (configuration II) and size (configuration III).

The axial turbulence intensity and Reynolds shear stress profiles measured displayed similarities in trend but differences in

level for the three vortex generator configurations tested. In the favorable forced mixing region, the profiles had two distinct components - one associated with the boundary layer and the other associated with the vortex. In the unfavorable forced mixing region no such distinction could be made. Rather a significant region of high turbulence fluid was evident. Turbulence intensity levels in the vicinity of the vortex cores were essentially equivalent to the maximum levels measured in the hub boundary layer.

Nondimensional eddy viscosity and mixing length profiles were determined for the most downstream axial location prior to the diffuser exit station. The profiles varied as a function of location with respect to the vortex location. As such it was not possible to determine a single value of eddy viscosity or mixing length for use in conventional two-dimensional turbulence models to account for the effects of forced mixing. In general all three vortex generator configurations increased the levels of eddy viscosity and mixing length over those measured with no vortex generators present by a factor of at least two to three.

BIBLIOGRAPHY

1. Chang, P. K.. Separation of Flow, Pergamon Press, 1970.

2. Bruynes, H.: Fluid Mixing Device. U.S. Patent 2,558,816, 1951.

3. Taylor, H. D.: "Application of Vortex Generator Mixing Principle To Diffusers," Concluding Report, United Aircraft Corp. Research Department, Report R-15064-5, December 31, 1948.

4. Taylor, H. D.: "Design Criteria For And Applications of the Vortex Generator Mixing Principle," United Aircraft Corporation Research Department, Report M-15038-1, February 18, 1948.

5. Taylor, H. D.: "United Aircraft Research Department Summary Report on Vortex Generators," United Aircraft Corp. Research Department, Report R-05280-9, March 7, 1950.

6. Taylor, H. D.: "Elimination of Diffuser Separation by Vortex Generators," United Aircraft Corporation Research Department, Report R-4012-3, 1947.

7. Taylor, H. D.: "Retractable Vortex Generators," United Aircraft Corporation Research Department, Report M-15335-3, June 22, 1950.

8. Schubauer, G. B.; and Spangenberg, W. G.: "Forced Mixing in Boundary Layers," Journal of Fluid Mechanics, Vol. 8, Pt. 1, May 1960.

9. Sajben, M.; Chen, C. P.; and Kroutil, J. C.: "Application of a New Boundary Layer Control Device to Conical Diffusers," McDonnell-Douglas Research Laboratories Report MDCQ0607, October 1976.

10. Woolard, H. W.: Boundary-Layer Forced Mixing Investigation - Literature Survey and Progress Report," Lockhead California Company, Report 18478, November 1966.

11. Pearcy, H. H.: "Shock Induced Separation and Its Prevention by Design and Boundary-Layer Control," Boundary Layer and Flow Control, Volume 2. Edited by G. V. Lachmann, Pergammon, 1961, pp. 1166-1344.

12. Valentine, E. F.; and Carroll, R. B.: "Effects of Some Primary Variables on Rectangular Vortex Generators on the Static Pressure Rise Through a Short Diffuser," NACA RM L52B13, 1952.

13. Valentine, E. F.; and Carroll, R. B.: Effects of Several Arrangements of Rectangular Vortex Generators on the Static Pressure Rise Through a Short 2:1 Diffuser," NACA RM L50L04, 1951.

14. Wood, C. O.: "Preliminary Investigation of the Effects of Rectangular Vortex Generators on the Performance of a Short 1.9:1 Straight-Wall Annular Diffuser," NACA RM L51G09, 1951.

15. Wood, C. O.; and Higginbotham, J. T.: "Influence of Vortex Generators on the Performance of a Short 1.9:1 Straight Wall Annular Diffuser with Whirling Inlet Flow," NACA RM L52L01a, 1953.

16. Wood, C. O.; and Higginbotham, J. T.: "Flow Diffusion in a Constant Diameter Duct Downstream of an Abruptly Terminated Centerbody," NACA RM L53D23, 1953.

17. Nishi, M.; and Senoo, Y.: "Investigation of Strength and Paths of Vortices Shed from Vortex Generators in a Pipe and Application to Conical Diffusers," Bulletin of the JSME, Vol. 17, No. 105, March 1974.

18. MacMiller, C. J.: "Investigation of Subsonic Duct Distortion," AIAA Paper 69-449, 1969.

19. Mitchell, G. A.; and Davis, R. W.: "Performance of Centerbody Vortex Generators in an Axisymmetric Mixed Compression Inlet at Mach Numbers from 2.0 to 3.0," NASA TN D-4679, July 1968.

20. Neumann, H. E.; Wasserbauer, J. F.; and Shaw, R. J.: "Performance of Vortex Generators in a Mach 2.5 Low-Bleed Full Scale 45-Percent-Internal-Contraction Axisymmetric Inlet," NASA TM X-3195, April 1975.

21. Ting, C. T.; Kaldschmidt, G.; and Syltebo, B. E.: "Design and Testing of New Center Inlet and S-Duct for B-727 Airplane with Refanned JT8D Engines," AIAA Paper 75-59, 1975.

22. Brown, A. C.; Nawrocki, H. F.; and Paley, P. N.: "Subsonic Diffusers Designed Integrally with Vortex Generators," Journal of Aircraft, Vol. 5, No. 3, May-June, 1968.

23. Jones, I. P.: "The Calculation of the Paths of Vortices from a System of Vortex Generators and Comparison with Experiment," British ARC, C.P. 361, 1955.

24. Spangler, J. G.; and Wells, C. S.: "Effects of Spiral Longitudinal Vortices on Turbulent Boundary Layer Skin Friction," NASA CR-145, December 1964.

25. Ponte, S.; and Baron, A.: "The Effect of Vortex Generators on the Development of a Boundary Layer," AGARD V/STOL Aerodynamics, 1974.

26. Gould, D. C.: "The Use of Vortex Generators to Delay Boundary Layer Separation. Theoretical Discussion Supported by Tests on a CF-100 Aircraft," National Aeronautical Establishment (Canada), Report LR-183, 1956.

27. Dosanjh, D. S.; Gasparek, E. P.; and Eskinazi, S.: "Decay of a Viscous Trailing Vortex," The Aeronautical Quarterly, May 1962.

28. Square, H. B.: "The Growth of a Vortex in Turbulent Flow," The Aeronautical Quarterly, August 1965.

29. Henry, J. R.; Wood, C. C.; and Wilbur, S. W.: "Summary of Subsonic-Diffuser Data," NACA RM L56F05, 1956.

30. Povinelli, L. A.: "An Experimental and Analytical Investigation of Axisymmetric Diffusers," NASA TM X-71786, 1975.

31. Anderson, O. L.: "Finite-Difference Calculation of Turbulent Swirling Compressible Flow in Axisymmetric Ducts with Struts and Slot Cooled Walls," USAAMRDL-TR-74-50, September 1974.

32. Boldman, D. R.; and Neumann, H. E.: "Experimental and Analytical Study of a Conically Diffused Flow with a Nearly Separated Boundary Layer," NASA TN D-748, 1973.

33. Robertson, J. M.; and Calehuff, G. L.: "Turbulence in Civil Engineering: Turbulence in a Diffuser Boundary Layer," Proc. ASCE 83, HY5, paper 1393, 1957.

34. Schubauer, G. B.; and Klebanoff, P. S.: "Investigation of Separation of the Turbulent Boundary Layer," NACA Report 1030, 1951.

35. Clauser, F. H.: "The Turbulent Boundary Layer," Advances in Applied Mechanics; vol. IV, Academic Press, New York, 1956, pp. 1-51.

36. Stevens, S. J.; and Williams, G. J.: "Measurements of the Overall Performance and Boundary Layer Growth in an Annular Diffuser," Symposium on Internal Flows, 1971.

37. Sovran, G.; and Klemp, G. D.: "Experimentally Determined Optimum Geometers for Rectilinear Diffusers with Rectangular, Conical or Annular Cross Section," Fluid Mechanics of Internal Flow, G. Sovran, ed. Elsevier Pub. Co., 1967, p. 293.

38. Mitchell, G. A.: "Preliminary Investigation of Inlet Ingestion of a Wing Tip Vortex," NASA TM X-68225, 1973.

39. Dudzinski, T. J.; and Krause, L. N.: "Flow Direction Measurement with Fixed-Position Probes," NASA TM X-1904, 1969.

40. Majola, O. O.: "A Hot-Wire Method for Three-Dimensional Shear Flows," Disa Information, No. 16, July 1974, pp. 11-14.

41. Clauser, F. H.: "Turbulent Boundary Layers in Adverse Pressure Gradients," Journal of the Aeronautical Sciences, February 1954, pp. 91-108.

APPENDIX A

Flow Angularity Probes

The design of the flow angularity probes used followed the philosophy of reference 39. The probes were calibrated in an atmospheric free jet facility at the NASA-Lewis Research Center to provide a calibration of flow yaw angle versus the appropriate pressure parameter. As reference 39 indicated, the calibration of such a probe should be Mach number independent for a Mach number range of $0.3 \leq M_\infty \leq 0.9$ so the calibrations were done for a free stream Mach number of 0.4. A sample calibration is included and shown as Figure 92.

Calibration data were taken for every 5° of yaw between $+30^\circ$ and -30°. Cubic least squares curves were then fit to each of the two segments (-30° to 0° and 0° to $+30^\circ$).

Since the differences in pressure between the two sides tubes were small, a 2.5 psid transducer was used to measure the difference $P_1 - P_2$ (see Fig. 92) while two 50 psi absolute transducers were used to measure P_t and P_1.

The digital computer data reduction program was then used to form the pressure parameter and determine the resulting flow yaw angle.

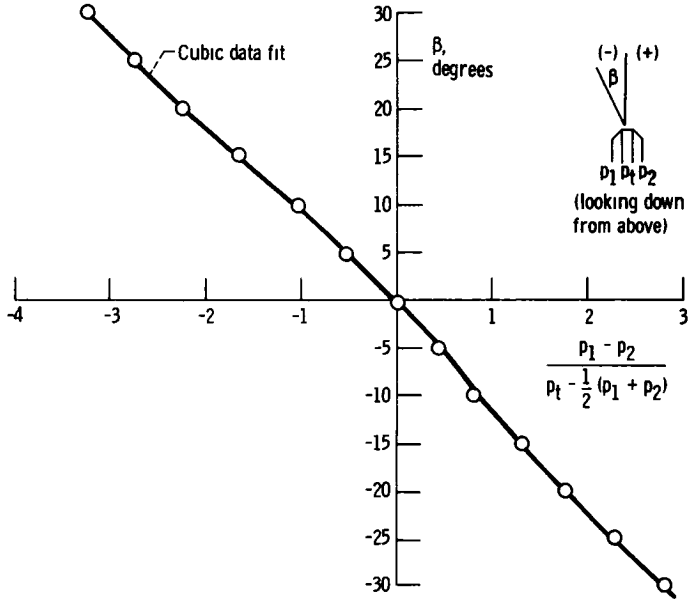

Figure 92. - Typical flow angularity probe calibration

APPENDIX B

Calibration of Hot Film Probes

Since the local diffuser boundary layer flow would be expected to be asymmetric due to the velocity components induced by the vortices, it was necessary to account for the three-dimensional velocity components in the response relations for the hot film probes. The standard hot film response equations quoted in the literature apply only to the specialized case where the axial velocity component is the only nonzero velocity component (i.e., $V = W = 0$). The method used for this study was developed by Majola[40] and will be outlined here.

A single hot film sensor placed in a flowing fluid and operated in a constant temperature mode will respond according to the following relation

$$E^2 = C_1 + \tilde{C}_2 \rho (Q_{eff})^n \tag{B1}$$

where

E is the voltage across the sensor

$C_1, \tilde{C}_2, n$ are calibration constants

ρ is the local fluid density

Q_{eff} is the effective cooling velocity past the sensor

If the fluid can be considered to be incompressible, the factor ρ^n can be absorbed into the constant C_2 to yield

$$E^2 = C_1 + C_2 (Q_{eff})^n \tag{B2}$$

A number of expressions have been proposed to relate the effective cooling velocity to the actual velocity components of the fluid. For this study the following relation was employed.

$$Q^2_{eff} = Q^2_{normal} + a^2 Q^2_{parallel} \tag{B3}$$

where

Q_{normal} is the velocity component normal to the sensor

$Q_{parallel}$ is the velocity component parallel to the sensor

a is an experimentally determined direction sensitivity coefficient

First consider a sensor located in a plane parallel to the YZ plane shown in Figure 93. It follows that

$$Q^2_{normal} = (U + u')^2 + (V + v')^2 \tag{B4}$$

$$Q^2_{parallel} = (W + w')^2$$

and thus

$$Q^2_{eff} = (U + u')^2 + (V + v')^2 + a^2(W + w')^2 \tag{B5}$$

Now if this expression is inserted into equation (B2), a standard decomposition of E into steady state and fluctuating components ($E = \bar{E} + e$) is performed, and second order terms are neglected, the following relationship involving the fluctuating components will result

$$e = \frac{n}{2}\left(\frac{\overline{E^2} - C_1}{\bar{E}^2}\right)\frac{u'}{U} \tag{B6}$$

In deriving the above expression, the assumption was made that the ratios of all velocity components to the mean velocity in the x-direction were small (V/U, W/U, u'/U, v'/U, $w'/U < 1$). That is, there is a preferred direction to the mean motion. This should be a reasonable assumption for the problem considered herein.

Now if each side of equation (B6) is squared, a time averaged performed and finally a square root of each side taken, the following expression will result for the local turbulence intensity.

$$\frac{\sqrt{\overline{u'^2}}}{U} = \frac{2}{n}\frac{\bar{E}\sqrt{\overline{e^2}}}{\bar{E}^2 - C_1} \tag{B7}$$

An expression for the mean axial velocity can also be gotten from the decomposition and the result is

$$U = \left(\frac{\overline{E}^2 - C_1}{C_2} \right)^{1/n} \tag{B8}$$

It is convenient to form an expression for the local mean velocity referenced to the maximum measured velocity. Such an expression easily follows from equation (B8)

$$\frac{U}{U_{max}} = \left(\frac{\overline{E}^2 - C_1}{\overline{E}^2_{max} - C_1} \right)^{1/n} \tag{B9}$$

The following calibration procedure was used to determine the constants C_1, C_2, and n for the single film probes. Initially each probe was run in the constant density free jet facility previously mentioned. All probes were operated with an overheat ratio of 1.5. The probe being calibrated was positioned in the inviscid core region of the jet and the steady state voltage output $\overline{E}$ was determined corresponding to a number of jet Mach numbers between 0.0 and 0.3. The data were then fitted using a least squared technique to the form of equation (B8) to determine the constants C_2 and n. The constant C_1 was taken to be the square of the voltage across the sensor when the fluid velocity was zero.

Once the hot film probes were installed in the diffuser experiment the calibration was repeated. The probes were positioned in the inviscid portion of the local flow field as determined by the measured total pressure profiles. A four-point calibration was then undertaken of each probe by varying the inlet conditions. Since it was not practical to hold the density constant in the diffuser experiment, equation (B1) was used to determine the calibration coefficients. In all instances, excellent agreement existed between the two calibrations performed for each probe.

Now consider a hot film sensor oriented in a plane parallel to the XY plane and inclined at an angle ψ with respect to the positive X direction as shown in figure 94.

The velocity components for this sensor are

$$\begin{aligned} Q^2_{normal} &= \left[(U + u')\sin\psi - (V + v')\cos\psi \right]^2 + (W + w')^2 \\ Q^2_{parallel} &= \left[(U + u')\cos\psi + (V + v')\sin\psi \right]^2 \end{aligned} \tag{B10}$$

If these expressions are again inserted into equation (B2), a decomposition performed, and the result time averaged, the following expression will result which relates the mean velocity components and turbulence quantities

$$k_0 U\left[1 + \left(\frac{k_1}{2} - \frac{k_2^2}{8}\right)\left(\frac{v'^2 + v^2}{U^2}\right) + k_3\left(\frac{w'^2 + w^2}{U^2}\right) + \frac{k_2}{2}\frac{v}{U}\right] =$$

$$= \left(\frac{\overline{E}^2 - C_1}{C_2}\right)^{1/n} (1 + f) \qquad \text{(B11)}$$

where

$$f = \frac{1}{n}\frac{\overline{e^2}}{\left(\overline{E}^2 - C_1\right)} + \frac{2}{n}\left(\frac{1 - n}{n}\right)\frac{\overline{E}^2\overline{e}^2}{\left(\overline{E}^2 - C_1\right)^2} \qquad \text{(B12)}$$

$$k_0 = (\sin^2\psi + a^2\cos^2\psi)^{1/2}$$

$$k_1 = \frac{\cos^2\psi + a^2 \sin 2\psi}{\sin^2\psi + a^2\cos^2\psi}$$

$$k_2 = \frac{(a^2 - 1)\sin^2\psi}{\sin^2\psi + a^2\cos^2\psi}$$

$$k_3 = \frac{1}{\sin^2\psi + a^2\cos^2\psi}$$

Now a cross film probe has two sensors which will be designated as I($\psi_I = 45^o$ nominally) and II($\psi_{II} = 135^o$ nominally). With these definitions of ψ_I and ψ_{II}, it follows that

$$\left.\begin{aligned} k_{0I} &= k_{0II} \\ k_{1I} &= k_{1II} \\ k_{2I} &= -k_{2II} \\ k_{3I} &= k_{3II} \end{aligned}\right\} \qquad \text{(B13)}$$

A relation like that of equation (B11) can be written for each of the two sensors of a cross film probe. If this is done and the two expressions are subtracted the following results

$$V = \frac{1}{k_{2I}k_{0I}}\left[\left(\frac{\bar{E}_I^2 - C_{1I}}{C_{2I}}\right)^{1/n_I}(1 + f_I) - \left(\frac{\bar{E}_{II}^2 - C_{2II}}{C_{2II}}\right)^{1/n_{II}}(1 + f_{II})\right] \tag{B14}$$

Thus as equation (B14) indicates it is possible to calculate the steady state transverse velocity component from the steady state and fluctuating voltage outputs of the two sensors of the hot film probe.

It is convenient to ratio V to the free stream velocity U_∞. If this is done the following will result

$$\frac{V}{U_\infty} = \frac{1}{k_{2I}}\left[\left(\frac{\bar{E}_I^2 - C_{1I}}{\bar{E}_{I\infty}^2 - C_{1I}}\right)^{1/n_I}\left(\frac{1 + f_I}{1 + f_{I\infty}}\right) - \left(\frac{\bar{E}_{II}^2 - C_{1II}}{\bar{E}_{II\infty}^2 - C_{1II}}\right)^{1/n_{II}}\left(\frac{1 + f_{II}}{1 + f_{II\infty}}\right)\right] \tag{B15}$$

It should be noted that the above expression was derived assuming that $V = 0$ when $U = U_\infty$.

In order to derive an expression for the turbulent shear stress, a decomposition is again performed and only the fluctuating portion of the relation considered. If this is done the following will result

$$\frac{\overline{u'v'}}{U^2} = \frac{1}{2k_{2I}}\left\{\left[\frac{2}{n_I}\left(1 + \frac{k_{2I}}{2}\cdot\frac{V}{U}\right)\frac{\bar{E}_I}{\left(\bar{E}_I^2 - C_{1I}\right)}\right]^2 \overline{e_I^2} - \left[\frac{2}{n_{II}}\left(1 + \frac{k_{2II}}{2}\cdot\frac{V}{U}\right)\frac{\bar{E}_{II}}{\left(\bar{E}_{II}^2 - C_{1II}\right)}\right]^2 e_{II}^2\right\} \tag{B16}$$

Equation (B16) indicates that the turbulent shear stress can be calculated if the steady state transverse velocity V is known. It is interesting to note that the circumferential velocity component W does not appear in the above expression. Thus, the use of equations (B15) and (B16) will allow the turbulent shear stress to be calculated for the locally three-dimensional flow using just the measurements from the cross film probe.

The calibrations for the cross film probes were performed in the free jet facility since it was not possible to re-orient the probes once they were installed in the diffuser experiment. Initially it was assumed that the n for each sensor of each probe was 0.5. This assumption seemed reasonable based upon the single film results. Then each probe was oriented in the inviscid core of the free jet, so one sensor was parallel to the flow direction and the other perpendicular to the flow direction. Data were then taken for jet Mach numbers from 0 to 0.3. The procedure was then repeated with the probe rotated 90° so as to reverse the orientation of the two sensors relative to the jet velocity.

A least squares curve fit of the data for the sensor oriented perpendicular to the flow velocity vector was then performed to determine the constants C_1 and C_2 for each of the two sensors. For a sensor oriented perpendicular to the flow direction, the governing equation is simply that given by equation (B8).

To determine the directional sensitivity coefficient a for each sensor of each probe, the data taken for the sensor oriented parallel to the flow directive was used. For this orientation, the governing equation would be

$$\overline{E}^2 = C_1 + C_2 \sqrt{aU_{jet}} \tag{B17}$$

Values of a were calculated for each measured jet velocity for each of the two sensors and the results averaged to get one value of a for each probe.

As already pointed out in order to calculate the turbulent shear stress it was necessary to first determine the transverse velocity component using equation (B15). It was noted that in the process of deriving equation (B15) the assumption was made that $V = 0$ when $U = U_{\infty}$. This assumption implies that the cross film probe would be properly oriented when placed in the free stream. The cross film probes used in this study were fabricated such that the probes were properly oriented with respect to the appropriate diffuser hub slope. Thus the probes would not be properly aligned when retracted into the free stream due to the flow curvature present within the diffuser flow field. The misalignment was estimated to be 2.0° for probe B, 4.7° for probe C, and 8.4° for probe D. This misalignment effect was judged to be small enough so that it could be ignored.

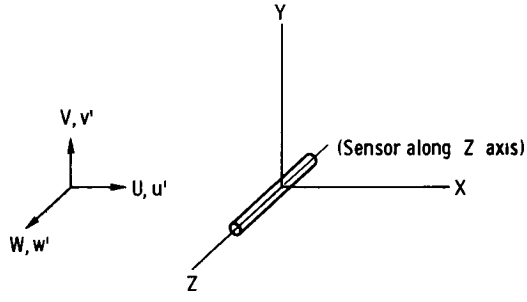

Figure 93 - Single film sensor orientation.

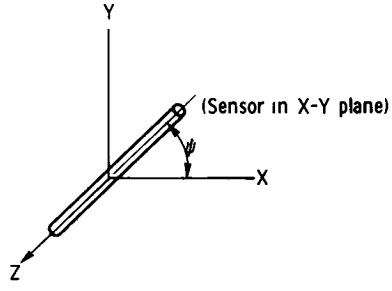

Figure 94 - Cross film sensor orientation

APPENDIX C

Analog Circuitry for Hot Film Data Reduction

The amount of data to be gathered using the five hot film anemometry probes made some sort of on-line processing of the analog signals mandatory. To accomplish this task an EAI 580 analog computer was programmed to process the incoming signals and present output signals of the quantities of interest. These output analog signals were sampled by the NASA Lewis Automatic Voltage Digitizing System (AVD) and then sent to the Central Automatic Digital Data Encoding System (CADDE) prior to being sent to the IBM 360 for processing into engineering units.

For the single film probes, the quantities of interest were the DC voltage $\overline{E}$ and the mean square average of the fluctuating voltages $\overline{e^2}$. The circuitry depicted in Figure 95 was designed to extract these quantities from the analog signal output from each of the five hot film anemometers.

The DC voltage branch of the circuit employed an operational amplifier with a capacitor in the feedback loop which resulted in an output signal with a two-second time average.

The average mean square fluctuating branch had an initial high pass RC filter with a time constant of 0.5 second and a half power point of 0.319 Hz to remove the DC voltage.

The instantaneous squared fluctuating voltage $\overline{e^2}$ was obtained as the output of a multiplier in the squaring configuration. An operational amplifier identically configured to the one discussed above averaged the instantaneous squared signal over 2 seconds to yield the desired output $\overline{e^2}$. The 2-second time constant for the mean square of the fluctuating signal was essentially consistent with the required time constant to yield an essentially constant mean square level as reported in reference 32. Visual readouts of the mean square analog output when data was being taken indicated that the 2-second time constant was adequate for "smoothing" of the data.

For the cross film probes, the same quantities $\overline{E}$ and $\overline{e^2}$ was of interest for each of the two sensors per probe. But, in addition, the mean value of the cross product of the two fluctuating signals was desired, i.e., $\overline{e_1 e_2}$. The same basic circuit design as

discussed above could be employed, but additional circuits were required to accommodate the increased number of quantities which had to be extracted from the output of each cross film probe. The circuit diagram for one cross film probe is shown in Figure 96. Note that four such circuits were required, one for each of the cross film probes.

The multipliers limited the frequency response of the above circuits. A frequency response check on a multiplier was undertaken and the results are shown in Figure 97. It can be seen that the response was essentially flat out to 34,000 Hz which was the limiting frequency of the test. On-line spectral plots of the analog output signals from the single film probes indicated that essentially all the turbulence energy was contained in the 0 to 10,000 Hz range so the multipliers did not reject any useful information when the instantaneous mean square signal was formed.

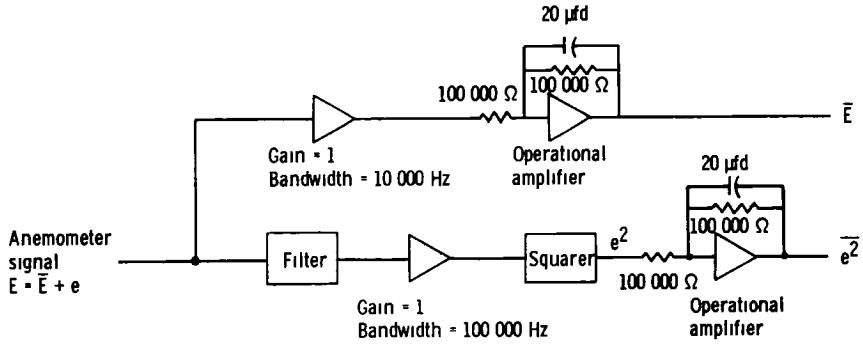

Figure 95 - Analog circuitry for single hot film sensor probe.

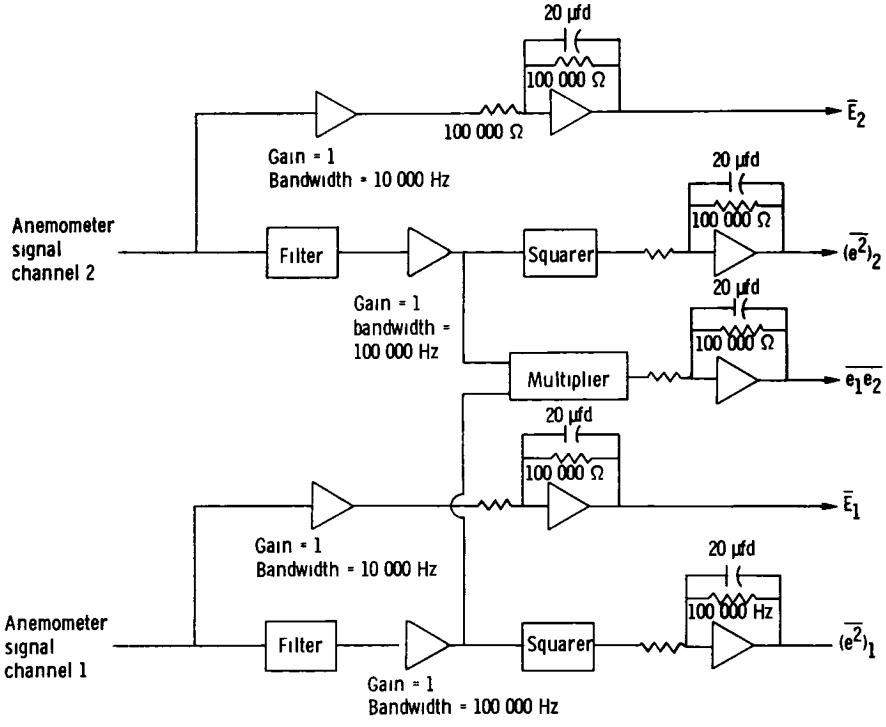

Figure 96 - Analog circuitry for cross hut film sensor probe.

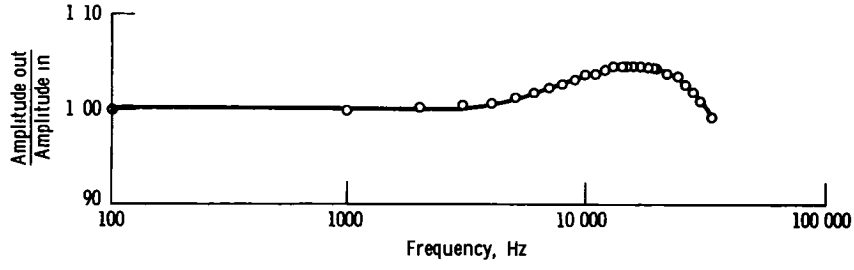

Figure 97 - Frequency response of multiplier

APPENDIX D

Clauser Plot Technique For Determining Skin Friction Coefficient

The Clauser plot technique[41] relies on the assumption that the turbulent boundary layer in question obeys its universal law of the wall, that is

$$\frac{U}{U_*} = 2.439 \ln \frac{yU_*}{\nu} + 5 \tag{D1}$$

where U_* is the friction velocity given by

$$U_* = \sqrt{\frac{\tau_w}{\nu}} \tag{D2}$$

Now the skin friction coefficient can be expressed as

$$C_f = \frac{U_*^2}{\frac{U_e^2}{2}} \tag{D3}$$

Now equation (D1) can be rewritten as follows where the ln has been recast as the base 10 logarithm

$$\frac{U}{U_e} = \frac{5.616 \log\left(\frac{yU_e}{\nu} \cdot \frac{U_*}{U_e}\right) + 5}{\frac{U_e}{U_*}} \tag{D4}$$

In the above equation (D5), the quantity U_e/U_* can be considered as the unknown quantity and a series of curves can be plotted which show U/U_e as a function of $\log(yU_e/\nu)$ with U_e/U_* as a parameter. This family of curves is shown in Figure 98.

If the boundary layer profile in question is plotted on a figure similar to 98, the appropriate value of U_e/U_* can be determined. This will allow U_* and, hence, C_f to be calculated.

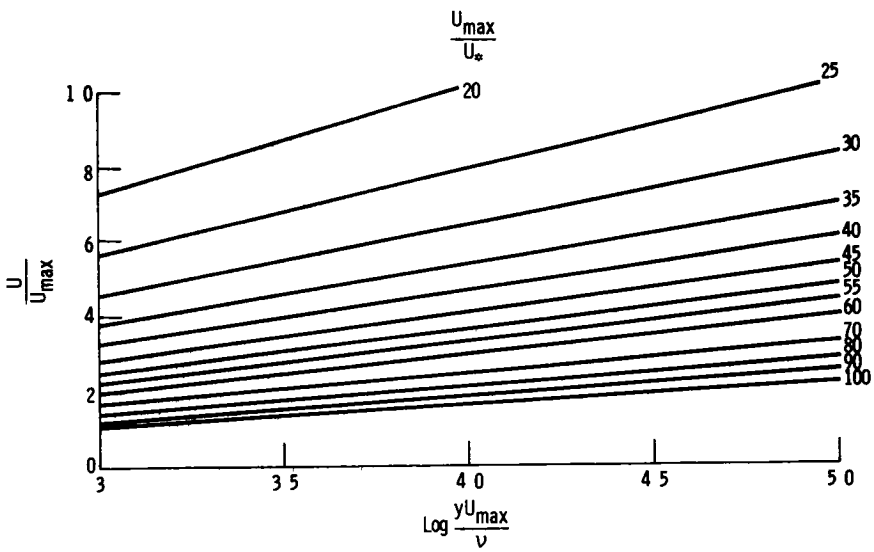

Figure 98. - Clauser skin friction plot.

1 Report No	2 Government Accession No	3 Recipient's Catalog No
NASA TM-79171		

4 Title and Subtitle	5 Report Date
AN EXPERIMENTAL INVESTIGATION OF FORCED MIXING OF A TURBULENT BOUNDARY LAYER IN AN ANNULAR DIFFUSER	April 1979
	6 Performing Organization Code
7 Author(s)	8 Performing Organization Report No
Robert Joseph Shaw	E-9947
	10 Work Unit No
9 Performing Organization Name and Address	
National Aeronautics and Space Administration Lewis Research Center Cleveland, Ohio 44135	11 Contract or Grant No
	13 Type of Report and Period Covered
12 Sponsoring Agency Name and Address	Technical Memorandum
National Aeronautics and Space Administration Washington, D C 20546	14 Sponsoring Agency Code

15 Supplementary Notes

Thesis submitted in partial fulfillment of the requirements for the Degree of Doctor of Philosophy

16 Abstract

An experimental program was conducted to determine the physical details of the forced mixing process of a turbulent boundary layer in an axisymmetric annular diffuser using conventional wing like vortex generators Detailed flow field measurements were made at four axial locations downstream of the vortex generators At each axial location, a total of 25 equally spaced profiles were measured behind three consecutive vortex generators which formed two pairs of vortex generators Total pressure profiles were measured to determine boundary layer profiles and vortex positions Hot film anemometry probes were used to measure the boundary layer turbulence structure at the same locations where pressure measurements were made. Both single and cross film probes were used The diffuser turbulence data was taken only for a nominal inlet Mach number of 0 3 Three vortex generator configurations were tested The differences between configurations involved changes in size and relative vortex generator positions All three vortex generator configurations tested provided increases in diffuser performance The differences in performance between the configurations was small Vortex paths agreed qualitatively in lateral spacing variation with simplified potential flow path prediction techniques The variation in height of the vortex axes above the surface did not agree with such predictions Distinct differences in the boundary layer integral properties and skin friction levels were noted between configurations The axial turbulence intensity and Reynolds stress profiles measured displayed similarities in trends but differences in levels for the three configurations

17 Key Words (Suggested by Author(s))	18 Distribution Statement
Supersonic propulsion system Diffuser flow Turbulent boundary layer Forced mixing, Vortex generators	Unclassified - unlimited STAR Category 02

19 Security Classif (of this report)	20 Security Classif (of this page)	21 No of Pages	22 Price*
Unclassified	Unclassified		

For sale by the National Technical Information Service Springfield Virginia 22161